

DISEQUILIBRIUM CARBON, OXYGEN, AND NITROGEN CHEMISTRY IN THE ATMOSPHERES OF HD 189733b AND HD 209458b

JULIANNE I. MOSES¹, C. VISSCHER², J. J. FORTNEY³, A. P. SHOWMAN⁴, N. K. LEWIS⁴, C. A. GRIFFITH⁴, S. J. KLIPPENSTEIN⁵,
 M. SHABRAM⁶, A. J. FRIEDSON⁷, M. S. MARLEY⁸, AND R. S. FREEDMAN⁸

¹ Space Science Institute, 4750 Walnut Street, Suite 205, Boulder, CO 80301, USA; jmoses@spacescience.org

² Lunar and Planetary Institute, Houston, TX 77058, USA

³ Department of Astronomy and Astrophysics, University of California, Santa Cruz, CA 95064, USA

⁴ Department of Planetary Sciences and Lunar and Planetary Laboratory, The University of Arizona, Tucson, AZ 85721, USA

⁵ Chemical Sciences and Engineering Division, Argonne National Laboratory, Argonne, IL 60439, USA

⁶ Department of Astronomy, University of Florida, Gainesville, FL 32611, USA

⁷ Earth and Space Sciences Division, Jet Propulsion Laboratory, California Institute of Technology, Pasadena, CA 91109, USA

⁸ NASA Ames Research Center, Moffett Field, CA 94035, USA

Received 2011 January 31; accepted 2011 May 3; published 2011 July 22

ABSTRACT

We have developed a one-dimensional photochemical and thermochemical kinetics and diffusion model to study the effects of disequilibrium chemistry on the atmospheric composition of “hot-Jupiter” exoplanets. Here we investigate the coupled chemistry of neutral carbon, hydrogen, oxygen, and nitrogen species on HD 189733b and HD 209458b and we compare the model results with existing transit and eclipse observations. We find that the vertical profiles of molecular constituents are significantly affected by transport-induced quenching and photochemistry, particularly on the cooler HD 189733b; however, the warmer stratospheric temperatures on HD 209458b help maintain thermochemical equilibrium and reduce the effects of disequilibrium chemistry. For both planets, the methane and ammonia mole fractions are found to be enhanced over their equilibrium values at pressures of a few bar to less than an mbar due to transport-induced quenching, but CH₄ and NH₃ are photochemically removed at higher altitudes. Disequilibrium chemistry also enhances atomic species, unsaturated hydrocarbons (particularly C₂H₂), some nitriles (particularly HCN), and radicals like OH, CH₃, and NH₂. In contrast, CO, H₂O, N₂, and CO₂ more closely follow their equilibrium profiles, except at pressures $\lesssim 1 \mu\text{bar}$, where CO, H₂O, and N₂ are photochemically destroyed and CO₂ is produced before its eventual high-altitude destruction. The enhanced abundances of CH₄, NH₃, and HCN are expected to affect the spectral signatures and thermal profiles of HD 189733b and other relatively cool, transiting exoplanets. We examine the sensitivity of our results to the assumed temperature structure and eddy diffusion coefficients and discuss further observational consequences of these models.

Key words: planetary systems – planets and satellites: atmospheres – planets and satellites: composition – planets and satellites: individual (HD 189733b, HD 209458b) – stars: individual (HD 189733, HD 209458)

Online-only material: color figures, supplemental data (FITS) file (tar.gz)

1. INTRODUCTION

The detection and characterization of extrasolar planets is one of the most exciting and fastest growing fields in astronomy (e.g., Charbonneau et al. 2007; Marley et al. 2007; Udry et al. 2007; Deming & Seager 2009; Baraffe et al. 2010). Of the handful of tools available for characterization of exoplanet atmospheres, transit and eclipse observations have proven to be invaluable for inferring properties of both the planet and its host star (e.g., Charbonneau et al. 2000, 2002, 2005; Henry et al. 2000; Seager & Sasselov 2000; Brown 2001; Brown et al. 2001; Burrows et al. 2001; Hubbard et al. 2001; Deming et al. 2005b; Knutson et al. 2007, 2009; Madhusudhan & Seager 2009). The wavelength dependence of the signal during transit and eclipse observations can allow identification of atmospheric constituents on “hot-Jupiter” exoplanets (e.g., Charbonneau et al. 2002; Vidal-Madjar et al. 2003; Tinetti et al. 2007; Grillmair et al. 2008; Swain et al. 2008b, 2009a; Madhusudhan & Seager 2009), allowing a better understanding of the chemical and physical processes operating in these exotic atmospheres.

Hot Jupiters are often divided into two classes, those that appear to have stratospheric thermal inversions, and those that do not (e.g., Fortney et al. 2008a; Hubeny et al. 2003; Harrington et al. 2007; Burrows et al. 2007, 2008; Knutson

et al. 2008; Spiegel et al. 2009; Madhusudhan & Seager 2009). Although the ultimate reasons for these differences are still under investigation (see also Spiegel et al. 2009; Zahnle et al. 2009; Knutson et al. 2010; Youdin & Mitchell 2010; Fressin et al. 2010; Machalek et al. 2008, 2010; Madhusudhan & Seager 2010), exoplanets with thermal inversions appear to have some source of high-altitude absorption, whereas exoplanets without thermal inversions are apparently missing this stratospheric absorber, perhaps because it is tied up in condensed phases (e.g., Hubeny et al. 2003; Fortney et al. 2008a; Burrows et al. 2008) or is destroyed by photolysis and/or other mechanisms related to chromospherically active host stars (Knutson et al. 2010). The observations discussed in the above citations suggest that HD 209458b has a strong stratospheric thermal inversion, whereas HD 189733b does not. These two transiting planets, which have been the most extensively studied and characterized to date because of their bright parent stars and large transit depths, become convenient endmembers for our study of the chemistry of the two main classes of hot Jupiters.

Constraints on the composition and thermal structure of HD 189733b and HD 209458b have been provided through (1) the identification of Na, H, and other atomic neutral and ionic species in the planets’ upper atmospheres (Charbonneau et al. 2002; Vidal-Madjar et al. 2003, 2004, 2008; Ben-Jaffel

2007, 2008; Ballester et al. 2007; Snellen et al. 2008; Redfield et al. 2008; Sing et al. 2008a; Ehrenreich et al. 2008; Langland-Shula et al. 2009; Linsky et al. 2010; Ben-Jaffel & Hosseini 2010; Lecavelier des Etangs et al. 2010), (2) the identification of molecular species such as H_2O , CH_4 , CO_2 , and CO in the ~ 1 bar to 0.1 mbar atmospheric region (Tinetti et al. 2007; Fortney & Marley 2007; Burrows et al. 2007, 2008; Grillmair et al. 2008; Barman 2008; Swain et al. 2008a, 2008b, 2009a, 2009b, 2010; Beaulieu et al. 2008, 2010; Désert et al. 2009; Madhusudhan & Seager 2009), (3) observational and theoretical inferences regarding the vertical and horizontal temperature structure, including the suggested presence of a stratospheric temperature inversion on HD 209458b but not on HD 189733b, and the identification of longitudinal temperature variations and phase lags (e.g., Knutson et al. 2007, 2009; Cooper & Showman 2006; Fortney et al. 2006, 2008a, 2010; Richardson et al. 2007; Burrows et al. 2007, 2008; Cowan et al. 2007; Showman et al. 2008, 2009; Madhusudhan & Seager 2009, 2010), and (4) the inferred presence of hazes, clouds, and Rayleigh scatterers that can affect atmospheric spectral behavior (e.g., Charbonneau et al. 2002; Fortney et al. 2003; Fortney 2005; Iro et al. 2005; Pont et al. 2008; Lecavelier des Etangs et al. 2008a, 2008b; Sing et al. 2008a, 2008b, 2009; Shabram et al. 2011). Note, however, that the data reduction and observational analyses are often difficult due to low signal-to-noise, potential variable stellar activity of the host star (including star spots), and/or poorly understood systematic instrument effects (e.g., Gibson et al. 2011); spectral models are also poorly constrained, making analysis of the observations difficult. Various groups do not always agree, even when examining the same or similar data sets (cf. Désert et al. 2009 versus Beaulieu et al. 2008 versus Ehrenreich et al. 2007; Swain et al. 2008b versus Sing et al. 2009 versus Gibson et al. 2011; Stevenson et al. 2010 versus Beaulieu et al. 2011). An additional problem with analyses is the lack of reliable molecular line parameters for hot bands of gases other than H_2O , CO , and CO_2 . Even if the data reduction and analysis were not inherently difficult, interpretation of thermal infrared data can be hampered by the fact that molecular bands can manifest as either absorption or emission features, depending on the atmospheric thermal structure, creating a degeneracy between temperature profiles and compositions (e.g., Burrows et al. 2008; Madhusudhan & Seager 2009, 2010; Tinetti et al. 2010; Fortney et al. 2010; O'Donovan et al. 2010). Despite these complications, transit and eclipse observations represent our best current means for characterizing the atmospheres of hot Jupiters. Theoretical models are needed to interpret these observations.

Existing chemical models for transiting exoplanets tend to fall into two groups: thermochemical-equilibrium models and photochemical models. Thermochemical equilibrium is assumed for most models (e.g., Burrows & Sharp 1999; Seager et al. 2000; Lodders & Fegley 2002; Sharp & Burrows 2007; Burrows et al. 2007, 2008; Fortney et al. 2008a; Visscher et al. 2010a), although potential departures from equilibrium are sometimes explored through evaluations of simple timescale arguments (e.g., Lodders & Fegley 2002; Fortney et al. 2006, 2008b; Visscher et al. 2006, 2010a; Madhusudhan & Seager 2011) or through more complex models with parameterized chemical kinetics (Cooper & Showman 2006). Thermochemical equilibrium is a reasonable starting point for exoplanet composition predictions, but the strong ultraviolet flux incident on close-in transiting planets like HD 189733b and HD 209458b can drive the observable upper regions of the atmosphere out of equilibrium. Moreover,

some of the existing transport and kinetics timescale arguments have known flaws (for further discussion, see Yung et al. 1988; Smith 1998; Bézard et al. 2002; Visscher et al. 2010b; Moses et al. 2010; Visscher & Moses 2011) and are often misused, leading to questionable predictions of quenched disequilibrium abundances.

The second group of chemical models exploits knowledge of Jovian photochemistry to predict the consequences of the large ultraviolet flux incident on exoplanet atmospheres (Liang et al. 2003, 2004; Yelle 2004; García Muñoz 2007; Koskinen et al. 2007, 2009; Zahnle et al. 2009, 2011; Line et al. 2010). Of these latter models, Yelle (2004), García Muñoz (2007), and Koskinen et al. (2007, 2009) focus on the uppermost regions of the atmosphere, i.e., the thermosphere, ionosphere, and exosphere and do not consider what goes on deeper than 1 μbar . In contrast, Liang et al. (2003, 2004) and Line et al. (2010) explore the photochemistry of the deeper stratosphere and troposphere using thermochemical equilibrium and/or transport-quenched disequilibrium as a lower boundary condition for their models; however, their focus on low-temperature reactions (for the former two studies) and their lack of fully reversed reactions (all three studies) prevents them from extending the kinetic models into the thermochemical regime at temperatures $\gtrsim 1000$ K, and their assumptions can result in artificial constant-with-altitude profiles for the major species in the troposphere. Zahnle et al. (2009, 2011) have published the only models to date that have attempted to bridge the thermochemistry and photochemistry regimes with a single model; however, their reliance on isothermal atmospheric models can result in some unrealistic vertical profiles and species abundances that will not be present with more realistic atmospheric structures, and it is not clear whether their reaction scheme will reproduce equilibrium at high temperatures.

We therefore have developed a unique one-dimensional (1D) thermochemical and photochemical kinetics and transport model to circumvent some of the problems described above. The model has the ability to transition seamlessly from the thermochemical-equilibrium regime in the deep troposphere of giant planets to the “transport-quenched” disequilibrium and photochemical regimes in the upper troposphere and stratosphere to illuminate how chemical processes in each regime combine to influence the observational properties of giant-planet atmospheres. In an initial set of studies, we applied the model to the deep troposphere of Jupiter to ensure that the model satisfies observational constraints on a well-studied planet within our own solar system (Visscher et al. 2010b; Moses et al. 2010). We now apply the model to the atmospheres of HD 189733b and HD 209458b, as representatives of the two classes of hot Jupiters—those with and without stratospheric thermal inversions. Our main goal is to more realistically predict the vertical profiles of the major observable carbon-, oxygen-, and nitrogen-bearing species on these close-in transiting planets to aid the analysis and interpretation of primary transit and secondary-eclipse observations. By including both thermochemical and photochemical kinetics in a traditional 1D chemistry/diffusion model, we can avoid some of the shortcomings and pitfalls of previous chemical models—we do not need to correctly identify in advance the mechanism and rate-limiting steps for transport quenching of species like CO , CH_4 , HCN , and NH_3 , we can avoid other uncertainties in the timescale arguments such as the correct length scale to use for the transport timescale (e.g., Smith 1998), we do not need to restrict the model to any particular pressure region, and we can

consider realistic atmospheric structures rather than isothermal atmospheres.

As we will show in the following sections, disequilibrium processes like transport-induced quenching and photochemistry can perturb the composition of HD 189733b and HD 209458b away from equilibrium. The effects of these disequilibrium processes are more significant for cooler exoplanets like HD 189733b than for warmer exoplanets like HD 209458b, but there are potential observational consequences for both planets. In particular, transport-induced quenching and photochemistry can enhance the abundance of atmospheric constituents like CH_4 , HCN , NH_3 , and C_2H_2 , and the presence of these disequilibrium molecules will affect spectral and photometric behavior. We compare the model results with existing transit and secondary-eclipse observations and discuss in detail the major disequilibrium mechanisms affecting the abundance of carbon, nitrogen, and oxygen species on HD 189733b and HD 209458b.

2. MODEL

We use KINETICS, the Caltech/JPL 1D photochemistry/diffusion code (Allen et al. 1981; see also Yung et al. 1984; Gladstone et al. 1996; Moses et al. 2000a, 2000b, 2005; Liang et al. 2003, 2004; Line et al. 2010) to calculate the vertical distributions of tropospheric and stratospheric constituents on extrasolar giant planets. This fully implicit, finite-difference code solves the coupled mass-continuity equations as a function of pressure for each species:

$$\frac{\partial n_i}{\partial t} + \frac{\partial \Phi_i}{\partial z} = P_i - L_i, \quad (1)$$

where n_i is the number density (cm^{-3}), Φ_i is the flux ($\text{cm}^{-2} \text{s}^{-1}$), P_i is the chemical production rate ($\text{cm}^{-3} \text{s}^{-1}$), and L_i is the chemical loss rate ($\text{cm}^{-3} \text{s}^{-1}$) of species i , all of which are explicit functions of time t and altitude z . The flux transport terms include both molecular and eddy diffusion, the latter parameterized by an eddy diffusion coefficient K_{zz} . The calculations are allowed to evolve until steady state is achieved, and a convergence criterion of one part in a thousand is used. We consider 198 atmospheric levels with a vertical resolution ranging from 30 grid points per atmospheric scale height in the deep atmosphere to 3 grid points per scale height in the upper atmosphere. A finer grid is needed in the deep atmosphere to accurately track the quench points for some of the disequilibrium species. The model extends from the deep tropospheres of HD 209458b (bottom boundary at 2754 K, 1 kbar) and HD 189733b (2600 K, 1.67 kbar) to well past the homopause region into the thermosphere (top boundary at pressures less than 10^{-10} bar, exospheric temperature assumed to be 12,000 K). The upper boundary is chosen at a high-enough altitude such that we encompass the photochemical production and destruction regions for the main molecular species H_2 , H_2O , CO , CH_4 , CO_2 , N_2 , NH_3 , and HCN for plausible assumptions about K_{zz} , and such that assumptions about upper boundary conditions do not affect the results. Although the models extend into the thermosphere, our intent is not to specifically model thermospheric chemistry. Instead, the thermospheric temperature profile and escape boundary condition are included in an ad hoc manner based on the results of Yelle (2004), García Muñoz (2007), and Koskinen et al. (2010) (see below for further details).

We use free-convection and mixing-length theories (e.g., Stone 1976; Flasar & Gierasch 1977) to define the eddy diffusion coefficients K_{zz} in the deep, adiabatic portion of the troposphere

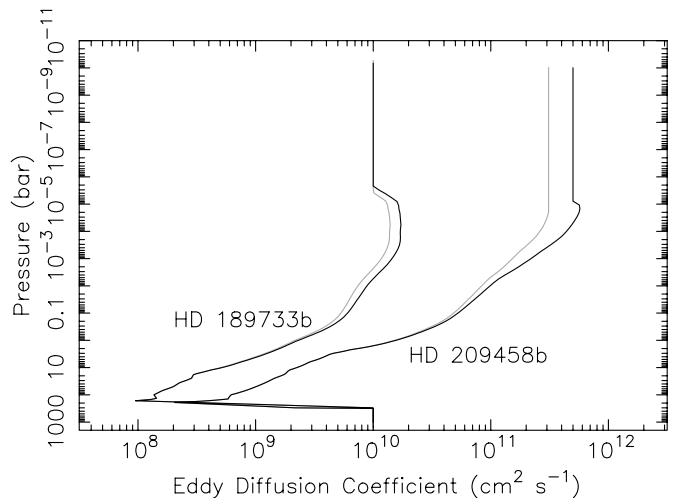


Figure 1. Eddy diffusion coefficient profiles adopted for our nominal models, as estimated from rms vertical velocity profiles obtained from the GCMs of Showman et al. (2009; see the text). For both planets, the black line represents the profile for the dayside-average model, and the gray line represents the profile for the terminator-average model. The high-pressure value of $K_{zz} = 10^{10} \text{ cm}^2 \text{ s}^{-1}$ is an estimate of the eddy diffusion coefficient in the adiabatic region from free-convection and mixing-length theory (Stone 1976), and K_{zz} are assumed to be constant at altitudes above the top level of the GCMs.

and estimate K_{zz} profiles through the bulk of the rest of the atmosphere from the root-mean-square (rms) vertical velocities derived from global horizontal averages at a given pressure level from the three-dimensional (3D) general circulation model (GCM) simulations of Showman et al. (2009), i.e., by assuming $K_{zz} = w(z)L(z)$, where $w(z)$ is the horizontally averaged global rms vertical velocity from the GCM simulations and $L(z)$ is assumed to be the atmospheric pressure scale height $H(z)$ (but could be some fraction of $H(z)$; see Smith 1998). Note that this procedure provides only a crude estimate of K_{zz} , and it would have been preferable to have calculated K_{zz} from the eddy vertical velocity times the eddy displacement, but this information was not available from the GCMs. In particular, the procedure may overestimate K_{zz} in the ~ 10 –200 bar radiative region, where the vertical motion tends to consist of small-scale wave oscillations. In the future, it would be useful to include passive tracers into the GCMs to directly and rigorously calculate the rate of vertical mixing. Figure 1 shows the eddy diffusion coefficient profiles adopted for our nominal models. However, given the above caveats, we consider K_{zz} profiles to be essentially free parameters in the models and examine the sensitivity of our results to reasonable variations in the adopted K_{zz} profiles. The molecular diffusion coefficients are described in Moses et al. (2000a).

Temperature profiles are not calculated self-consistently within the KINETICS code but are instead required as inputs to the model. The temperatures adopted in our model are shown in Figure 2. Most of these profiles derive from the 3D GCM simulations of Showman et al. (2009) for the region from 170 bar to a few μbar or the 1D models of Fortney et al. (2006, 2010) for the region from 1000 to 1.0×10^{-6} bar. Because the nitrogen species in particular quench at very high temperatures, we needed to extend the GCM profiles to deeper levels (i.e., to reach temperatures of at least 2500 K). The 1D models of Fortney et al. (2006, 2010) already include the deep adiabatic region, but the GCM profiles do not. For HD 189733b, the 1D “4 π ” profiles of Fortney et al. (2006, 2010) that assume the incident stellar energy is redistributed over the entire planet

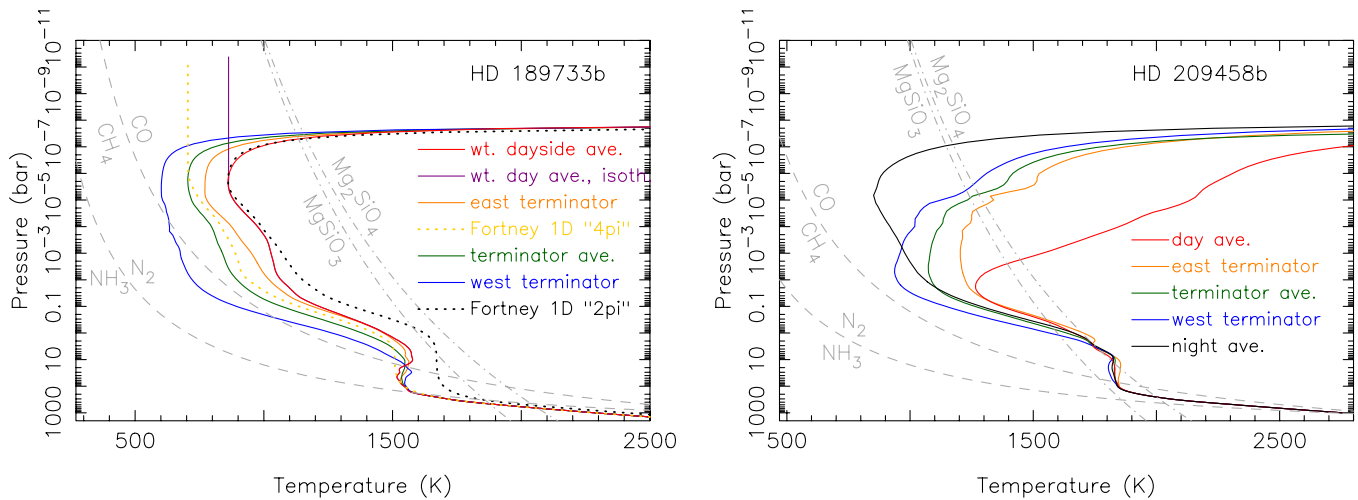


Figure 2. Temperature profiles for our models of HD 189733b (left) and HD 209458b (right), based on the general circulation models of Showman et al. (2009; solid lines) and on the 1D radiative-convective models of Fortney et al. (2006, 2010; dotted lines), for an assumed solar-composition atmosphere. For HD 189733b, the models include a projected-area-weighted profile averaged over the dayside hemisphere (to best represent the planet’s apparent disk during the secondary eclipse), profiles averaged over the eastern and western terminators (to best represent the ingress and egress regions during the transits), a terminator-average profile, and 1D profiles calculated assuming the incident stellar energy is distributed over the entire planet (curve labeled “4pi”) or over the dayside hemisphere only (curve labeled “2pi”). For HD 209458b, the models include a straight (i.e., not projected-area) average over the dayside hemisphere, along with eastern and western terminator averages, a terminator average, and an average over the nightside hemisphere. Most profiles have been given an ad hoc high-temperature thermosphere at high altitudes based on the models of Yelle (2004) and García Muñoz (2007). Also shown are pressure–temperature curves (dashed gray lines) at which the major nitrogen species, N_2 and NH_3 , and the major carbon species, CO and CH_4 , have equal abundances in thermochemical equilibrium. To the left-hand side of these $\text{CH}_4 = \text{CO}$ and $\text{NH}_3 = \text{N}_2$ curves, the reduced species (CH_4 and NH_3) dominate, while the more oxidized species (CO and N_2) dominate to the right. Note that both planets are within the CO - and N_2 -dominated regimes over much of the atmosphere for all temperature profiles except for the coolest HD 189733b western-terminator-average profile. The gray dot-dashed lines represent the approximate condensation curves for the major silicates enstatite (MgSiO_3) and forsterite (Mg_2SiO_4), based on Visscher et al. (2010a).

(A color version of this figure is available in the online journal.)

compare very well with the GCM theoretical thermal profiles in the 1–100 bar region, so we extended the GCM profiles to deeper pressures by simply connecting smoothly to the 1D profiles. For HD 209458b, the 1D “4 π ” profiles are somewhat warmer than the GCM profiles in the 1–100 bar region, and we shifted the 1D profiles by -60 K before connecting the GCM profiles to this deeper adiabatic region. At low pressures (high altitudes), we extended the profiles by assuming either an isothermal atmosphere or a high-temperature thermosphere, using the thermospheric profiles of Yelle (2004) and García Muñoz (2007) as a guide for the latter. Once the pressure–temperature profiles were established, the rest of the background atmospheric grid (e.g., densities, altitudes) was derived through solving the hydrostatic equilibrium equation.

HD 189733b orbits its host star at a distance of ~ 0.031 AU (e.g., Southworth 2010). The cool but chromospherically active HD 189733 has an effective temperature in the range ~ 5050 – 5090 K (Bouchy et al. 2005; Knutson et al. 2010) and has typically been classified in the literature as a K1 V-to-K2 V main-sequence star (e.g., Barnes et al. 2010; Shkolnik et al. 2008), although the *Hipparcos* catalog lists it as a G5 V (Perryman et al. 1997; see also Montes et al. 2001). In any case, HD 189733 is less luminous than the Sun, and HD 189733b is not one of the hottest of the transiting exoplanets that have been discovered to date, despite its small orbital semimajor axis. HD 189733 is part of a binary star system, but the M dwarf companion to HD 189733 is ~ 200 AU away and should not significantly affect the flux incident on HD 189733b. Because well-calibrated ultraviolet spectra for HD 189733 are available for only a specific range of wavelengths (e.g., Lecavelier des Etangs et al. 2010), we set up a normalized 1 AU spectrum using the *Hubble Space Telescope* (HST) Space Telescope Imaging Spectrograph (STIS) spectra of epsilon

Eridani (a K2 V star) from the CoolCAT database (Ayers 2005) for the 1150–2830 Å region, after correcting for stellar distance. At the upper end of this wavelength range, the flux from epsilon Eridani is much less than for typical G stars like our Sun at the same stellar distance, whereas the flux at the shorter EUV wavelength end of this range compares well to main-sequence G stars. We therefore use the 1 AU solar flux divided by 10 for wavelengths longer than 2830 Å and use the 1 AU solar flux for low-to-average solar conditions as an analog for our 1 AU-normalized HD 189733 flux for wavelengths below 1150 Å. The photochemical calculations are then performed assuming that HD 189733b is located 0.031 AU from this K2 V-analog star. The host star for HD 209458b is a G0 V stellar type (*Hipparcos*; Perryman et al. 1997), and we simply use the solar flux as an analog for HD 209458, and assume HD 209458b orbits at a distance of 0.047 AU (e.g., Southworth 2010). The stellar zenith angle θ is fixed at 48° for the dayside-average models—where $\langle \cos \theta \rangle = 2/3$ ($\theta \approx 48^\circ$) is the projected-area-weighted average of the cosine of the stellar zenith angle over the planetary disk at secondary-eclipse conditions—and θ is fixed at $\sim 84^\circ$ – 86° for the terminator models. Multiple Rayleigh scattering by H_2 and He is considered in the model using a Feautrier radiative-transfer method (Michelangelo et al. 1992).

We consider the neutral chemistry of 90 carbon-, hydrogen-, oxygen-, and nitrogen-bearing species: the model contains H , H_2 , He, C, CH, excited singlet $^1\text{CH}_2$, ground-state triplet $^3\text{CH}_2$, CH_3 , CH_4 , C_2 , C_2H , C_2H_2 , C_2H_3 , C_2H_4 , C_2H_5 , C_2H_6 , C_3H_2 , C_3H_3 , $\text{CH}_3\text{C}_2\text{H}$, CH_2CCH_2 , C_3H_5 , C_3H_6 , C_3H_7 , C_3H_8 , C_4H , C_4H_2 , C_4H_3 , C_4H_4 , C_4H_5 , C_4H_6 , C_4H_8 , C_4H_9 , C_4H_{10} , C_5H_3 , C_5H_4 , C_6H_2 , C_6H_3 , C_6H_4 , C_6H_5 , non-cyclic C_6H_6 , C_6H_6 (benzene), O, $\text{O}(^1\text{D})$, O_2 , OH, H_2O , CO, CO_2 , HCO, H_2CO , CH_2OH , CH_3O , CH_3OH , HCCO, H_2CCO , $\text{C}_2\text{H}_3\text{O}$, CH_3CHO , $\text{C}_2\text{H}_4\text{OH}$, HO_2 , H_2O_2 , N, N_2 , NH, NH_2 , NH_3 , NNH, N_2H_2 , singlet

biradical H_2NN , N_2H_3 , N_2H_4 , CN , HCN , H_2CN , CH_2NH , CH_3NH , CH_2NH_2 , CH_3NH_2 , CH_2CN , CH_3CN , C_3N , HC_3N , $\text{C}_2\text{H}_2\text{CN}$, $\text{C}_2\text{H}_3\text{CN}$, NO , NO_2 , N_2O , HNO , HNO_2 , NCO , HNCO , and CH_3NO . Metals, rock-forming elements, and sulfur and phosphorus species are not considered, nor is ion chemistry. See Zahnle et al. (2009) for a discussion of the effects of sulfur photochemistry on exoplanet composition. The reaction list derives originally from the Jupiter and Saturn models of Gladstone et al. (1996), Moses (1996), and Moses et al. (1995a, 1995b, 2000a, 2000b, 2005), although extensive updates that account for high-temperature kinetics have been included based largely on combustion-chemistry literature (e.g., Baulch et al. 1992, 1994, 2005; Atkinson et al. 1997, 2006; Smith et al. 2000; Tsang 1987, 1991; Dean & Bozzelli 2000). See Visscher et al. (2010b) for further discussion of the hydrocarbon and oxygen kinetics and Moses et al. (2010) for further discussion of the nitrogen kinetics. The model contains ~ 1600 reactions, with the rate coefficients of ~ 800 of the reactions being taken from literature values, and the remaining ~ 800 reactions being the reverse of these “forward” reactions, with the rate coefficients of the reverse reactions being calculated internally at each pressure–temperature point along the grid using the thermodynamic principle of microscopic reversibility (e.g., $k_{\text{for}}/k_{\text{rev}} = K_{\text{eq}}$, where k_{for} is the rate coefficient for the forward reaction, k_{rev} is the rate coefficient for the reverse reaction, and K_{eq} is the equilibrium constant of the reaction; see Visscher & Moses 2011 for further details). The rate-coefficient expressions for the forward reactions (and their literature sources) are provided in Table S1 of the Supplementary Material. The rate coefficients for the reverse reactions for the pressure–temperature conditions of certain of our exoplanet models can be found in the full model outputs also presented in the Supplementary Material. Note that Miller et al. (2009) demonstrate that detailed balance assuming microscopic reversibility is expected to be quite accurate, even for complicated chemical reactions that involve multiple, interconnected potential wells.

We assume a $1\times$ protosolar composition atmosphere (Lodders 2003, 2009; Lodders et al. 2009) in thermochemical equilibrium for our initial conditions for all the constituents, using the NASA CEA code (Gordon & McBride 1994) for the equilibrium calculations. Thermodynamic parameters are taken from Gurvich et al. (1989–1994), the JANAF tables (Chase 1998), Burcat & Ruscic (2005), or other literature sources. Note that although we do not consider rock-forming elements and their resulting effects on the chemistry of oxygen, we do assume that $\sim 20\%$ of the oxygen has been sequestered along with silicates and metals (see Lodders 2004) in the deep atmospheres of HD 189733b and HD 209458b, thus depleting the available oxygen above the silicate clouds. As such, our “solar” abundance of oxygen is slightly less than that used by many other groups, and the species profiles themselves should not be considered accurate within and below the silicate cloud condensation regions due to our neglect of the effects of rock-forming elements (see Figure 2).

For boundary conditions, we assume zero flux at the top and bottom boundaries so that no mass enters or leaves the system. The lower boundary in our models is at a high-enough temperature that thermochemical equilibrium will prevail, and a zero-flux boundary condition is reasonable. We also checked cases with a fixed-mixing-ratio lower boundary condition for all constituents, set at their equilibrium values, rather than a zero-flux lower boundary condition and found no difference in the results. The upper boundary in our model is at a pressure of a

few times 10^{-5} μbar , which typically corresponds to a planetary radius less than three times the 1 bar radius R_p in exoplanet hydrodynamic models (and in some cases much less than $3R_p$, depending on the model; see Yelle 2004; Tian et al. 2005; García Muñoz 2007). At these high altitudes, the hydrodynamic models and model-data comparisons show the atmosphere of HD 209458b to be escaping, with an overall mass loss rate that is low enough that exoplanets like HD 209458b would lose less than $\sim 1\%$ of their mass over their lifetime (e.g., Lecavelier des Etangs et al. 2004; Tian et al. 2005; Murray-Clay et al. 2009). As such, we also test cases with an upper escape boundary condition for species like atomic H, with a typical upward flux of $\sim (6\text{--}60) \times 10^{11} \text{ cm}^{-2} \text{ s}^{-1}$ (e.g., $10^7\text{--}10^8 \text{ g s}^{-1}$ for HD 209458b at a radius of $3R_p$; see Yelle 2004; García Muñoz 2007; Tian et al. 2005; Koskinen et al. 2010), or we investigate a range of possible upper boundary escape fluxes from 10^{10} to $10^{16} \text{ cm}^{-2} \text{ s}^{-1}$, but we find that this upper boundary condition has no effect on the stratospheric or lower-thermospheric results. However, we have not included a hydrodynamic wind connecting to this escaping region, which is the main reason the escape flux has little effect on our model stratosphere. Hydrodynamic models (Yelle 2004; Tian et al. 2005; García Muñoz 2007) show that the atmosphere should be close to hydrostatic equilibrium below $2\text{--}3 R_p$, with the base of the planetary wind usually being located near the 1 nbar level (see also the discussion in Koskinen et al. 2010). Thus, escape from a hydrodynamic or thermal wind is not expected to substantially influence the composition of the stratosphere, and hydrostatic equilibrium is a reasonable assumption in our models. However, if an atmospheric bulk wind actually dominates down to the base of the thermosphere (or deeper) for any particular exoplanet, then hydrodynamic flow and atmospheric escape could conceivably affect the stratospheric composition on such exoplanets.

3. RESULTS

Our model results suggest that the three main chemical processes—thermochemical equilibrium, transport-induced quenching, and photochemistry—all operate effectively in the atmospheres of HD 189733b and HD 209458b. Thermochemical equilibrium dominates at pressures greater than a few bars, transport-induced quenching can dominate for some species in the $\sim 1\text{--}10^{-3}$ bar region, and photochemistry can dominate at pressures less than $\sim 10^{-3}$ bar, except when the stratosphere is very hot. All three processes combine to influence the vertical profiles of the important observable constituents on HD 189733b and HD 209458b. As such, all three processes should be considered in investigations of the chemistry and composition of extrasolar giant planets. Below we describe how the different disequilibrium processes affect the results and discuss the dominant mechanisms that control the abundances of neutral carbon, oxygen, and nitrogen species in our thermochemical and photochemical kinetics and transport models. The column abundances for some of the interesting species in our models are shown in Table 1, and full model outputs are supplied in the Supplementary Material.

3.1. Equilibrium versus Transport-induced Quenching versus Photochemistry

Figure 3 illustrates how the individual disequilibrium processes affect the mole fractions of some species in our dayside-average HD 189733b and HD 209458b models. The dashed curves show the thermochemical-equilibrium solutions. Note

Table 1
Column Abundances Above 1 bar

Species	Nominal K_{zz} Terminator HD 189733b	Nominal K_{zz} Dayside HD 189733b	$K_{zz} = 10^7$ Dayside HD 189733b	$K_{zz} = 10^{11}$ Dayside HD 189733b	Nominal K_{zz} Dayside HD 209458b	Nominal K_{zz} Terminator HD 209458b
H	2.1×10^{20}	9.3×10^{20}	1.2×10^{21}	7.9×10^{20}	2.2×10^{22}	8.9×10^{21}
H ₂	1.0×10^{26}	1.0×10^{26}	1.0×10^{26}	1.0×10^{26}	2.3×10^{26}	2.3×10^{26}
He	1.9×10^{25}	1.9×10^{25}	1.9×10^{25}	2.0×10^{25}	4.5×10^{25}	4.5×10^{25}
C	5.6×10^{14}	4.1×10^{15}	1.2×10^{15}	6.1×10^{14}	7.0×10^{15}	2.1×10^{15}
CH ₃	2.0×10^{17}	2.3×10^{17}	7.2×10^{16}	3.7×10^{18}	1.9×10^{17}	1.7×10^{17}
CH ₄	5.5×10^{21}	1.5×10^{21}	4.4×10^{20}	2.4×10^{22}	1.2×10^{20}	2.1×10^{20}
C ₂ H ₂	6.6×10^{16}	3.0×10^{16}	2.8×10^{15}	4.6×10^{18}	3.4×10^{15}	2.7×10^{15}
C ₂ H ₄	1.8×10^{16}	6.3×10^{15}	5.6×10^{14}	1.6×10^{18}	1.6×10^{14}	2.4×10^{14}
C ₂ H ₆	2.4×10^{11}	5.4×10^{13}	4.9×10^{12}	1.3×10^{16}	3.2×10^{11}	7.7×10^{11}
C ₃ H ₂	9.4×10^{14}	9.2×10^{14}	7.1×10^{14}	2.5×10^{15}	7.9×10^6	3.7×10^8
C ₄ H ₂	4.3×10^{12}	1.5×10^{10}	1.5×10^9	6.1×10^{13}	3.3×10^4	1.9×10^5
C ₆ H ₆	6.8×10^{12}	4.5×10^{11}	8.1×10^{11}	2.5×10^{11}	1.2×10^{-4}	1.0×10^{-2}
O	2.5×10^{14}	7.7×10^{14}	8.5×10^{13}	5.8×10^{14}	6.1×10^{16}	3.5×10^{15}
OH	1.6×10^{15}	8.3×10^{15}	7.9×10^{15}	1.3×10^{16}	5.5×10^{17}	1.5×10^{17}
H ₂ O	4.6×10^{22}	4.2×10^{22}	4.1×10^{22}	6.7×10^{22}	9.4×10^{22}	9.6×10^{22}
CO	5.1×10^{22}	5.4×10^{22}	5.5×10^{22}	2.9×10^{22}	1.3×10^{23}	1.3×10^{23}
CO ₂	1.6×10^{19}	1.2×10^{19}	1.2×10^{19}	9.9×10^{18}	1.9×10^{19}	2.3×10^{19}
HCO	1.7×10^{14}	4.7×10^{14}	4.8×10^{14}	2.5×10^{14}	5.0×10^{15}	3.4×10^{15}
H ₂ CO	1.0×10^{16}	1.0×10^{16}	1.1×10^{16}	5.6×10^{15}	2.3×10^{16}	2.3×10^{16}
CH ₃ OH	1.8×10^{13}	7.3×10^{10}	8.7×10^{12}	6.1×10^{13}	7.3×10^{12}	9.4×10^{12}
N	6.4×10^{14}	2.3×10^{15}	5.6×10^{13}	9.8×10^{14}	7.1×10^{15}	2.1×10^{15}
N ₂	7.3×10^{21}	7.5×10^{21}	8.2×10^{21}	4.9×10^{21}	1.9×10^{22}	1.9×10^{22}
NH ₂	8.4×10^{15}	2.8×10^{16}	2.5×10^{15}	9.1×10^{16}	3.9×10^{16}	2.2×10^{16}
NH ₃	1.7×10^{21}	1.2×10^{21}	1.0×10^{20}	4.1×10^{21}	1.6×10^{20}	1.8×10^{20}
HCN	1.8×10^{20}	1.4×10^{20}	5.0×10^{18}	2.6×10^{21}	1.4×10^{19}	1.3×10^{19}
H ₂ CN	1.3×10^{13}	1.8×10^{13}	8.1×10^{11}	3.6×10^{14}	5.5×10^{12}	4.1×10^{12}
CH ₂ NH	1.9×10^{15}	9.3×10^{14}	3.9×10^{13}	1.8×10^{16}	5.6×10^{13}	6.4×10^{13}
CH ₃ CN	6.2×10^{14}	1.6×10^{14}	1.9×10^{12}	4.8×10^{16}	7.7×10^{11}	1.2×10^{12}
NO	1.7×10^{14}	4.3×10^{14}	8.5×10^{12}	5.2×10^{14}	7.6×10^{15}	4.6×10^{14}
HNCO	4.5×10^{15}	5.0×10^{15}	4.4×10^{14}	9.0×10^{15}	1.1×10^{15}	1.0×10^{15}

Notes. Model column abundances have units of cm^{-2} ; K_{zz} have units of $\text{cm}^2 \text{ s}^{-1}$. “Terminator” refers to a terminator-average and “dayside” refers to a dayside-average temperature profile for the planet in question from the GCMs of Showman et al. (2009). Our “nominal” K_{zz} profiles are shown in Figure 1.

that CH₄ dominates over CO, H₂O dominates over CO, and NH₃ dominates over N₂ at equilibrium in the deepest regions of both atmospheres, but the dominance reverses at higher altitudes such that CO and N₂ are the dominant carbon- and nitrogen-bearing species in equilibrium at pressures less than ~ 10 bar (i.e., over most of the observable portion of the atmosphere; see also Figure 2). At the highest altitudes (i.e., in the thermosphere), atomic species C, N, and O become the dominant neutral carbon, nitrogen, and oxygen carriers. Although H₂O remains an important carrier of oxygen at all pressures on these planets, thermochemical-equilibrium models predict that the mixing ratios of CH₄ and NH₃ will drop off dramatically with increasing altitude, such that $\text{CO} \gg \text{CH}_4$ and $\text{N}_2 \gg \text{NH}_3$ in terms of the column abundance at 1 bar and above. Thermochemical equilibrium predicts an even smaller column abundance for species like HCN and C₂H₂, such that these species would be at most minor constituents on HD 189733b and HD 209458b if their atmospheres were in equilibrium.

The situation changes significantly when vertical transport is considered. The dotted curves in Figure 3 show the results of models in which thermochemical kinetics and vertical transport are operating but in which the planet receives no photolyzing ultraviolet radiation from the host star, i.e., so that we can examine the influence of transport-induced quenching separately from that of photochemistry. At deep pressure levels in these

atmospheres, temperatures are high enough that energy barriers to the kinetic reactions can be overcome; reactions proceed in both the forward and reverse directions, and equilibrium is maintained. Our kinetics models, which have fully reversed reactions, reproduce equilibrium predictions in these high-temperature, high-pressure regions. However, as a gas parcel is lifted to cooler, higher altitudes, energy barriers can begin to become insurmountable over typical atmospheric residence timescales, and exothermic “forward” reactions can become favored over their endothermic reverses. When the transport timescale drops below the chemical kinetic conversion timescale between different molecular species, the species can become quenched such that their mole fractions become “frozen in” at values representative of the quench point (i.e., where the two time constants are equal). Prinn & Barshay (1977) first developed this concept analytically to explain the unexpectedly large CO abundance in Jupiter’s upper troposphere. Based on CO and other observations, transport-induced quenching appears to be ubiquitous in substellar objects, operating on our solar-system giant planets (e.g., Prinn & Barshay 1977; Lewis & Prinn 1980; Prinn & Olaguer 1981; Lewis & Fegley 1984; Fegley & Prinn 1985; Fegley & Lodders 1994; Lodders & Fegley 2002; Bézard et al. 2002; Visscher & Fegley 2005; Visscher et al. 2010b; Moses et al. 2010), on brown dwarfs (e.g., Fegley & Lodders 1996; Noll et al. 1997; Griffith & Yelle 1999; Saumon et al. 2000,

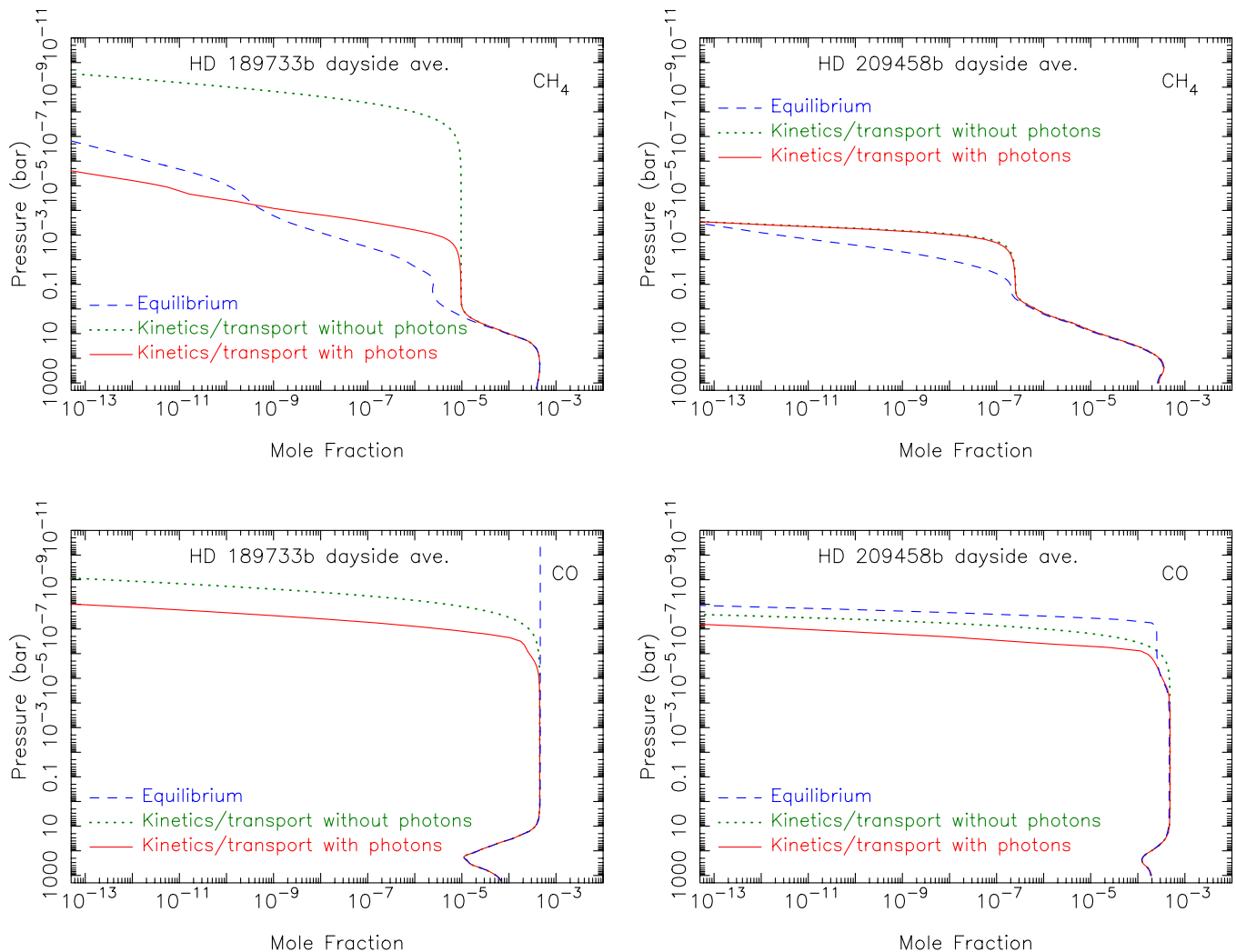


Figure 3. Mole fractions for several species in our models for HD 189733b (left) and HD 209458b (right) for different assumptions about the chemistry and transport. All HD 189733b models assume a projected-area-weighted dayside-average thermal structure with an isothermal extension at high altitudes (i.e., with a cold thermosphere), and all HD 209458b models assume a dayside-average thermal structure with a hot thermosphere (see Figure 2 for the temperature profiles for these models). The dashed lines are for a purely thermochemical-equilibrium model (no kinetics or transport), the dotted lines are for a model that has thermochemical kinetics and transport but no incident ultraviolet photons (i.e., no photochemistry), and the solid lines represent our full model with thermochemical and photochemical kinetics and transport all operating. The eddy diffusion coefficient K_{zz} is fixed at a constant value of $10^9 \text{ cm}^2 \text{ s}^{-1}$ in the transport models.

(A color version of this figure is available in the online journal.)

2003, 2006; Leggett et al. 2007; Hubeny & Burrows 2007; Geballe et al. 2009; Yamamura et al. 2010; King et al. 2010; Visscher & Moses 2011), and most likely on extrasolar planets, as well (e.g., Cooper & Showman 2006; Fortney et al. 2006; Burrows et al. 2008; Line et al. 2010; Madhusudhan & Seager 2011, and references therein). Although both CO and CH₄ will quench when the kinetic interconversion between the two species becomes inefficient, the quenching is more obvious for the species that is not expected to be abundant in equilibrium (i.e., CO on the cooler giant planets and brown dwarfs; CH₄ on the warmer, highly irradiated, close-in transiting giant planets).

The dotted curves in Figure 3 show that transport-induced quenching can greatly increase the predicted abundances of several key species, including CH₄, NH₃, and HCN, over expectations based on thermochemical equilibrium (dashed curves). The quench point for a major species like CH₄ is caused by the breakdown of efficient kinetic interconversion between itself and another major species (CO in this case) and results in an obvious departure from the predicted equilibrium curve. Once an abundant species like CH₄ becomes quenched,

its quenched abundance can affect other minor species like C₂H_x that might not have reached their own quench points yet; these species may continue to react with the CH₄ at higher altitudes in an equilibrium with the quenched CH₄ until they too reach their own quench points. Thus, minor species may depart from equilibrium when a major parent molecule quenches, but their mole fractions may not become constant until they themselves quench at higher, cooler altitudes. As such, the mole fractions from the full kinetics and transport model can have complicated behavior that is not easily predicted from simple time-constant arguments using a single rate-limiting kinetic reaction. Hydrogen cyanide (HCN), for example, maintains an equilibrium with H₂ and with the quenched abundances of CH₄ and NH₃ until its own quench point when the interconversion of NH₃–N₂–CH₄ shuts down, and the resulting mole-fraction profile is complicated. In addition, the quenching may not be abrupt, which can affect the mole-fraction profiles and make abundances more difficult to predict analytically. Ammonia, for example, has two quench points in the HD 189733b model. Ammonia first diverges from the equilibrium curve at the

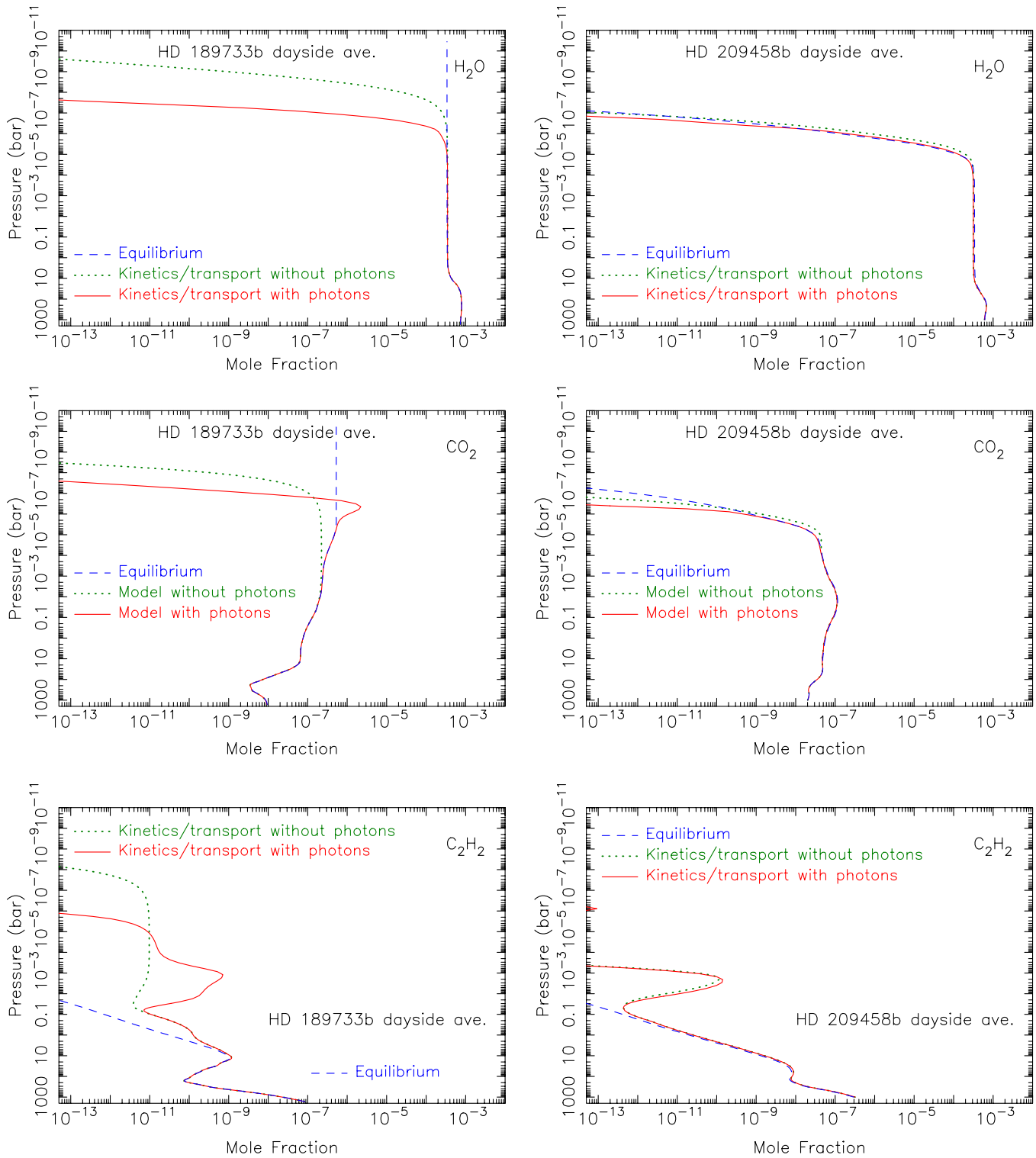


Figure 3. (Continued)

N_2 – NH_3 interconversion quench point, which is at relatively high temperatures and pressures due to the strong $\text{N}\equiv\text{N}$ triple bond. However, there is a pressure and temperature dependence to the different chemical pathways that allow $\text{NH}_3 \leftrightarrow \text{N}_2$ interconversion, and different reactions begin to dominate at different pressure levels. More importantly, the temperatures in the HD 189733b models do not drop off significantly between the “initial” NH_3 quench point near ~ 200 bar and the “final” quench point at the few-bar level, allowing the interconversion

reactions to continue to operate at a reduced but still effective rate in the intervening region. The final NH_3 quench occurs when the thermal gradients become large again and the temperatures become low enough that the NH_3 – N_2 interconversion reactions cease to become important. Ammonia quenching then operates over an extended range on HD 189733b, as marked by the two quench-point arrows in the HD 189733b NH_3 panel in Figure 3. The thermal gradients are larger in the region where NH_3 initially quenches on HD 209458b, allowing chemical

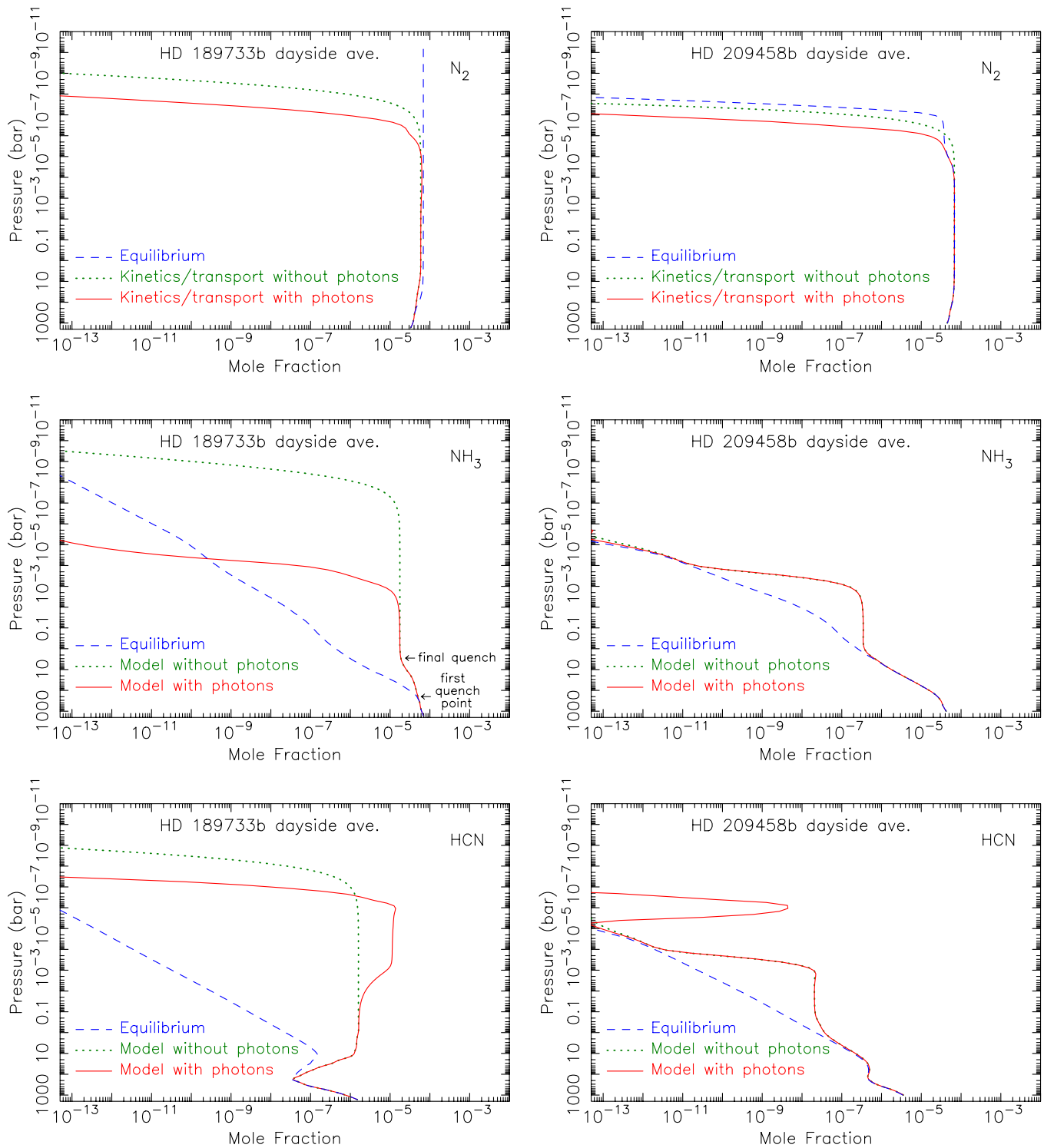


Figure 3. (Continued)

conversion reactions to shut down more abruptly, with a better-defined single quench level for NH_3 in the HD 209458b models.

The details of the particular quenching mechanisms, and their sensitivity to temperature and transport assumptions, will be discussed below. At this point, we simply want to illustrate that transport-induced quenching can be an important process on extrasolar giant planets that can allow disequilibrium species to be carried to relatively high altitudes to potentially affect spectral behavior. Note that transport-induced quenching

is much more important on the cooler HD 189733b than on HD 209458b. Although Figure 3 shows that quenching does occur in our dayside HD 209458b kinetics/transport models, the effectiveness of transport-induced quenching on HD 209458b is limited by the presence of a strong stratospheric thermal inversion—as temperatures become hot enough in the stratosphere, thermochemical kinetics drives the composition back toward equilibrium. When the inversion is weak on or absent from HD 209458b (i.e., at the terminators or nightside), transport-induced quenching becomes more important.

The stratospheric thermal inversion also affects the height to which the molecules can be carried. The models for both planets in Figure 3 have the same eddy diffusion coefficient, yet a comparison of the dotted-line models for both planets shows that the species reach different pressure levels on each planet. The difference is only partly due to the higher temperatures creating a lower homopause level on HD 209458b (where the term “homopause” refers to the pressure level at which the molecular and eddy diffusion coefficient are equal; above the homopause, molecular diffusion acts to limit the abundance of heavier species, whereas below the homopause the atmosphere can be well mixed). This point is demonstrated by a close comparison of CO and N₂ on each planet, as these thermochemically stable species reach their homopause levels, yet they are carried to only slightly different pressures on each planet. The main cause of the limited penetration of molecular species to high altitudes on dayside HD 209458b is the high stratospheric temperatures—species like CH₄ and NH₃ cannot survive the thermochemical kinetics at these temperatures and are converted into atomic C, N, and H, as well as to the more stable molecular species CO and N₂.

Another interesting point to note from Figure 3 is that some molecules like CO, H₂O, N₂, and CO₂ are relatively unaffected by transport-induced quenching on either planet. Although CO, H₂O, and N₂ technically also quench in the thermochemical kinetics and transport models, they are already the dominant species at their quench points, and the quenching does not greatly affect their abundances. As we will show below, this result is somewhat dependent on assumptions about the eddy diffusion coefficient and temperature structure. On HD 189733b, CO₂ quenches eventually (see where the dotted curve diverges from the dashed curve), but only at very high altitudes, and its abundance follows equilibrium at the pressure levels at which the observations are the most sensitive ($\sim 1\text{--}10^{-4}$ bar; see Fortney et al. 2008a). Other species like hydrocarbons, nitriles, and most nitrogen-bearing species are strongly affected by transport-induced quenching.

A comparison of the solid curves with the dotted curves in Figure 3 shows the influence of photochemistry. When ultraviolet photons are present, molecules like H₂O, CO, N₂, and NH₃ are photolyzed, initiating a slew of photochemical reactions that alter the chemistry and composition. As discussed by Liang et al. (2003), one main result of the photochemistry in the atmospheres of close-in extrasolar giant planets is the production of huge quantities of atomic hydrogen from photolysis of H₂O, followed by catalytic destruction of H₂ from the reaction of molecular hydrogen with the photolytic product OH. Other similar catalytic cycles are initiated deeper in the atmosphere from NH₃ photolysis and from reaction of H with CH₄ (see also Zahnle et al. 2011).

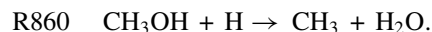
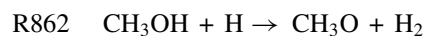
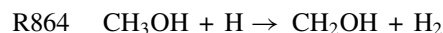
Because many molecules are vulnerable to attack by atomic hydrogen at these temperatures, the production of atomic H sets the stage for the subsequent photochemistry. Some molecules like H₂O, N₂, and CO are efficiently recycled and are relatively stable against photochemistry. As can be seen from Figure 3, photochemistry only affects the profiles of these species at very high altitudes, where visible and infrared transit and eclipse observations have little sensitivity. Other molecules like CH₄ and NH₃ have weaker bonds and/or are more reactive and less efficiently recycled. These molecules can be removed from portions of the visible atmosphere, to be replaced by photochemical products. The big winners in terms of photochemistry are atomic species such as H (by far the

dominant photochemical product), C, O, and N; some radicals like CH₃, NH₂, and OH; unsaturated hydrocarbons like C₂H₂; and some nitriles like HCN. Note that photochemistry (and thermochemistry, if the atmosphere is warm) can keep molecular species from reaching their homopause levels, as species can become kinetically destroyed faster than eddy diffusion can transport them to high altitudes. Below we discuss the kinetic mechanisms in more detail.

3.2. Quench Kinetics

As shown in Figure 3 and discussed above, transport-induced quenching is an important process in the atmospheres of extra-solar giant planets. For relatively warm planets like HD 189733b and HD 209458b, the thermal structure lies within the CO and N₂ stability fields at the temperatures and pressures where quenching occurs, so that the less abundant CH₄ and NH₃ are strongly affected by quenching. This situation differs from that of cooler planets like GJ 436b (which is in the CH₄ and N₂ stability fields, so that quenching of CO and NH₃ can be important) or from cold planets like Jupiter (which is in the CH₄ and NH₃ stability fields, so that quenching of CO and N₂ is important) or from brown dwarfs like Gliese 229b whose thermal structure crosses the CO = CH₄ and N₂ = NH₃ boundaries in such a location that quenching of all four molecules—CO, CH₄, N₂, and NH₃—could be important.

The kinetic pathways leading to the quenching of CO–CH₄ interconversion, N₂–NH₃ interconversion, and NH₃–HCN–CH₄ interconversion have been discussed in Visscher et al. (2010b) and Moses et al. (2010). We have made several updates to the rate coefficients used in those studies, including adopting the CH₃ + OH reaction pathways and rate coefficients of Jasper et al. (2007), and updating the rate coefficients for the nitrogen reactions based on Klippenstein et al. (2009) and Klippenstein (2010). Because of uncertainties in the kinetic rate coefficients for certain key reactions in the CO \leftrightarrow CH₄ interconversion scheme (see Visscher et al. 2010b), we have taken a more detailed look at the CH₃OH + H reaction and its various pathways for this paper. In particular, we have used ab initio transition-state theory to predict the rate coefficients for the three primary channels of the reaction of H with CH₃OH:



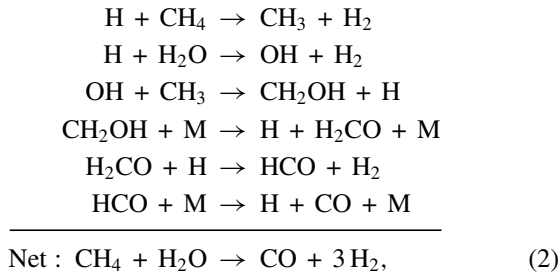
We used the QCISD(T)/cc-pVTZ method (e.g., Pople et al. 1987; Dunning 1989) to predict the rovibrational properties of the stationary points. Higher-level energies were obtained from basis-set extrapolation of explicit QCISD(T) calculations for the cc-pVTZ and cc-pVQZ basis sets. These QCISD(T)/CBS//QCISD(T)/cc-pVTZ calculations were performed with the spin-restricted formalism using the MOLPRO software package.⁹ Zero-point corrected barrier heights of 11.0, 13.4, and 24.2 kcal mol^{−1} were obtained for channels R864, R862, and R860, respectively. Most of the modes were treated as

⁹ MOLPRO is a package of ab initio programs written by H.-J. Werner, P. J. Knowles, F. R. Manby, M. Schütz, P. Celani, G. Knizia, T. Korona, R. Lindh, A. Mitrushenkov, G. Rauhut, T. B. Adler, R. D. Amos, A. Bernhardsson, A. Berning, D. L. Cooper, M. J. O. Deegan, A. J. Dobyn, F. Eckert, E. Goll, C. Hampel, A. Hesselmann, G. Hetzer, T. Hrenar, G. Jansen, C. Köppl, Y. Liu, A. W. Lloyd, R. A. Mata, A. J. May, S. J. McNicholas, W. Meyer, M. E. Mura, A. Nicklaß, P. Palmieri, K. Pflüger, R. Pitzer, M. Reiher, T. Shiozaki, H. Stoll, A. J. Stone, R. Tarroni, T. Thorsteinsson, M. Wang, and A. Wolf.

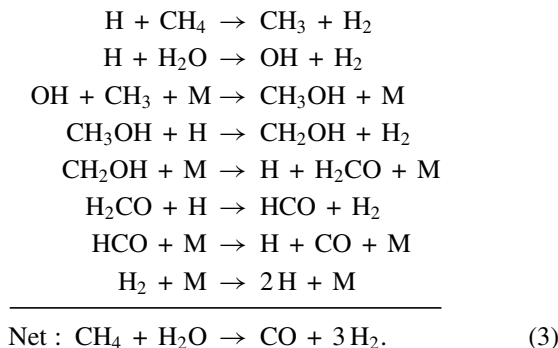
rigid-rotor harmonic oscillators, but hindered-rotor torsional and asymmetric Eckart-tunneling corrections were included as appropriate.

The predicted rate coefficients for reactions R864–R860 are well reproduced over the 500–2500 K region by the modified Arrhenius expressions, $k_{864} = 1.09 \times 10^{-19} T^{2.728} \exp(-2240/T)$, $k_{862} = 6.82 \times 10^{-20} T^{2.658} \exp(-4643/T)$, and $k_{860} = 4.91 \times 10^{-19} T^{2.485} \exp(-10380/T) \text{ cm}^3 \text{ molecule}^{-1} \text{ s}^{-1}$. These predictions are expected to be accurate to within a factor of two. For channels R864 and R862, the predictions are within a factor of 1.35 of the G2-based estimates from Jodkowski et al. (1999) but have lower uncertainties due to the use of higher levels of electronic-structure theory. The more recent predictions of Carvalho et al. (2008) are closely related to the present ones, being only about 0.8 times lower. The only prior study of channel R860 appears to be the G2-based study of Lendvay et al. (1997), which did not provide explicit expressions for this rate coefficient. The absence of both theoretical and experimental data for channel R860 was the motivating factor for the present ab initio transition-state theory analysis, as Visscher et al. (2010b) have suggested that this pathway could be important in the overall interconversion scheme between CH_4 and CO on giant planets.

The above ab initio calculations indicate, however, that the reaction R860 ($\text{CH}_3\text{OH} + \text{H} \rightarrow \text{CH}_3 + \text{H}_2\text{O}$) is too slow to participate in the dominant CH_4 –CO quenching scheme in our HD 189733b and HD 209458b models. Instead, we find that the dominant reaction scheme controlling $\text{CH}_4 \rightarrow \text{CO}$ conversion and methane quenching depends on the eddy diffusion coefficient and pressure–temperature conditions at the quench point; the dominant scheme can even bypass methanol (CH_3OH) altogether in some cases. For smaller eddy diffusion coefficients, the quench level is at lower pressures (higher altitudes), and the dominant CH_4 –CO conversion scheme becomes



where M represents any third body. For larger eddy diffusion coefficients, the quench level is at higher pressures (lower altitudes), and the dominant CH_4 –CO conversion scheme can become



The rate-limiting step for the $\text{CH}_4 \rightarrow \text{CO}$ conversion process is the slowest reaction in the fastest overall conversion scheme.

For the above scheme (2), the rate-limiting reaction is $\text{OH} + \text{CH}_3 \rightarrow \text{CH}_2\text{OH} + \text{H}$ (reaction number R670 in our list), and for the above scheme (3), the rate-limiting reaction is $\text{OH} + \text{CH}_3 + \text{M} \rightarrow \text{CH}_3\text{OH} + \text{M}$ (reaction R674). The relative importance of schemes (2) and (3) depends on which of these $\text{OH} + \text{CH}_3$ pathways are faster for the pressure–temperature conditions at the quench level for the planet under consideration. We adopt rate-coefficient expressions for these two potential rate-limiting reactions from Jasper et al. (2007), who provide a thorough description of the pressure and temperature dependence. Both schemes typically contribute some nontrivial fraction of the rate of interconversion in our models, so considering both pathways in a combined rate-limiting step can furnish a good description of the methane mole-fraction quenching behavior on transiting exoplanets (Visscher & Moses 2011).

Note that although the C–H–O system has been well studied due to applications in combustion chemistry and terrestrial atmospheric chemistry (e.g., Baulch et al. 2005; Atkinson et al. 2006), the kinetics of $\text{CO} \leftrightarrow \text{CH}_4$ interconversion in reducing environments remains somewhat uncertain. The rate coefficients for the above rate-limiting reactions are uncertain by perhaps a factor of three, and other alternative schemes may be competing if other rate coefficients in our full list are in error. The methane mole fraction on HD 189733b and HD 209458b will depend critically on the kinetic rate coefficients adopted in the model, particularly for the reactions that form C–O bonds from species with O–H and C–H bonds. The abundance of quenched species is always highly dependent on the assumed kinetic rate coefficients, as well as on the assumed strength of atmospheric mixing.

Despite these uncertainties, the $\text{OH} + \text{CH}_3 + \text{M} \rightarrow \text{CH}_3\text{OH} + \text{M}$ and the $\text{OH} + \text{CH}_3 \rightarrow \text{CH}_2\text{OH} + \text{H}$ reactions are much more likely to be the rate-limiting step in the conversion of CH_4 to CO on exoplanets than the reaction $\text{OH} + \text{CH}_3 \rightarrow \text{H}_2 + \text{H}_2\text{CO}$ (i.e., the reverse of the CO quench reaction originally proposed by Prinn & Barshay 1977), as the latter reaction is a few orders of magnitude too slow to be a likely player in any dominant conversion scheme (see Dean & Westmoreland 1987; Yung et al. 1988; Griffith & Yelle 1999; Bézard et al. 2002; Jasper et al. 2007; Visscher et al. 2010b). Note also that the dominance of CH_2OH over CH_3O as a product in the reaction of H with CH_3OH and in the reaction of OH with CH_3 , combined with the rapid thermal decomposition of CH_2OH , suggests that the dominant pathway will involve CH_2OH as an intermediate, not CH_3O , which was suggested or adopted in previous CO or CH_4 quenching studies (e.g., Yung et al. 1988; Bézard et al. 2002; Cooper & Showman 2006; Visscher et al. 2010b; Line et al. 2010; Madhusudhan & Seager 2011).

The transport timescale arguments of Prinn & Barshay (1977) can be used to predict the quenched abundance of CH_4 on exoplanets (see also the updates proposed by Visscher & Moses 2011). With this procedure, the quench point is located where the chemical kinetic conversion timescale τ_{chem} is equal to the vertical transport timescale τ_{dyn} . Then, the mole fraction of the quenched species above the quench level is simply the equilibrium mole fraction of the constituent at that quench point. In our models, the chemical kinetic conversion timescale for CH_4 is

$$\begin{aligned}
 \tau_{\text{chem}} &= \frac{[\text{CH}_4]}{d[\text{CH}_4]/dt} \\
 &= \frac{[\text{CH}_4]}{k_{670}[\text{CH}_3][\text{OH}] + k_{674}[\text{CH}_3][\text{OH}][\text{M}]}, \quad (4)
 \end{aligned}$$

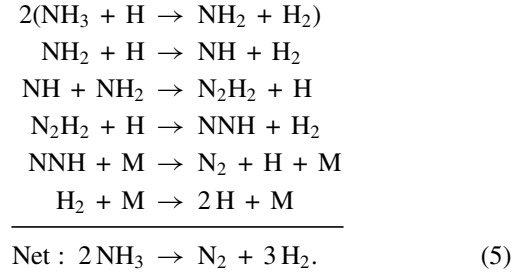
where $[X]$ represents the equilibrium concentration of species X in cm^{-3} , k_{670} is the rate coefficient for reaction R670 in $\text{cm}^3 \text{s}^{-1}$, and k_{674} is the rate coefficient for R670 in $\text{cm}^6 \text{s}^{-1}$. See Jasper et al. (2007), Visscher & Moses (2011), and Supplementary Table S1 for more details on k_{670} and k_{674} .

The transport timescale is $\tau_{\text{dyn}} = L^2/K_{zz}$, where L is an effective length scale over which dynamical mixing operates. As discussed by Smith (1998), L is generally some fraction of the scale height H . For quenching of CO on cold planets like Jupiter, $L \approx 0.1H$, whereas for quenching of CH_4 on close-in transiting hot Jupiters, L is closer to $0.5H$ (see Visscher & Moses 2011). When we use the procedure suggested by Smith (1998) to derive L and when we calculate τ_{chem} as described in Equation (4) for our rate-limiting step, we derive a quenched mole fraction within $\sim 15\%$ of our kinetics/transport model results for HD 189733b and HD 209458b. Therefore, as is also discussed by Bézard et al. (2002), Cooper & Showman (2006), Visscher et al. (2010b), Moses et al. (2010), and Visscher & Moses (2011) the transport timescale approach is valid provided that the Smith (1998) formalism for τ_{dyn} is used and provided that the assumed kinetic rate-limiting step is a reasonable one. We caution that the timescale approach has been misused frequently in exoplanet and brown-dwarf literature, where errors in the calculation of the rate coefficients for the rate-limiting steps have arisen due to incorrect reversals of three-body reactions (Griffith & Yelle 1999; Line et al. 2010), or where numerous other misconceptions about rate-limiting reactions and their rate coefficients and transport timescales are ubiquitous (see Bézard et al. 2002; Visscher et al. 2010b; Moses et al. 2010; Visscher & Moses 2011 for a more detailed discussion of the problem). Some of these problems have serious implications with respect to conclusions about the strength of atmospheric mixing, particularly on brown dwarfs (Troyer et al. 2007; Visscher & Moses 2011), where K_{zz} is likely several orders of magnitude greater than the sluggish $K_{zz} \approx 10^2\text{--}10^4 \text{ cm}^2 \text{s}^{-1}$ that has often been reported (e.g., Griffith & Yelle 1999; Saumon et al. 2003, 2006; Leggett et al. 2007; Geballe et al. 2009), but also in relation to the implied strength of atmospheric mixing on exoplanets (e.g., Madhusudhan & Seager 2011).

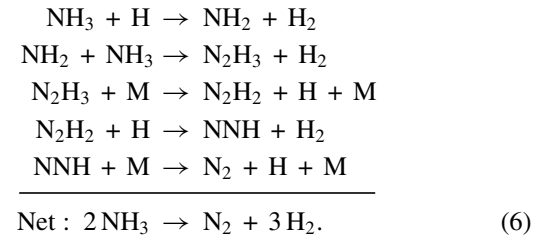
The timescale approach fails for species that have more than one quench point, for species that have an extended quench region due to τ_{chem} remaining close to τ_{dyn} over an extended pressure region, or for species that otherwise exhibit complicated kinetic behavior due to quenching of other key species. As an example, NH_3 in our HD 189733b models quenches in a region of the atmosphere in which the temperature does not fall off sharply with height. The NH_3 mole fraction departs from the equilibrium curve when τ_{dyn} drops below τ_{chem} and conversion between NH_3 and N_2 first becomes inhibited; however, due to the nearly isothermal behavior of the atmosphere above the quench region, τ_{chem} remains relatively close to τ_{dyn} over an extended pressure range, and NH_3 does not fully quench until the temperatures begin to fall off sharply again. Therefore, the time-constant arguments provide a good prescription for where the NH_3 leaves equilibrium but not for the final quenched mole fraction.

Several mechanisms closely compete as the dominant mechanism involved in $\text{NH}_3 \rightarrow \text{N}_2$ conversion, and again, the dominance depends on pressure–temperature conditions near the quench point. In our HD 209458b models, where the atmosphere is relatively warm and NH_3 quenches at relatively low

pressures, the dominant scheme is

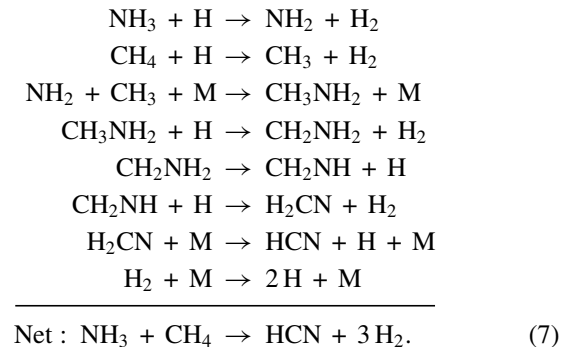


On the cooler HD 189733b, NH_3 first quenches down deep at high pressures and slightly lower temperatures than at the quench point on HD 209458b, through the dominant scheme

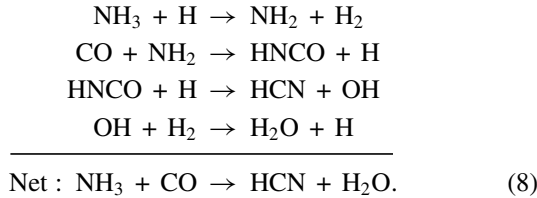


However, this scheme (6) becomes less important with decreasing pressure, and scheme (5) is responsible for the final quench point on HD 189733b. The rate-limiting step in scheme (5) is $\text{NH} + \text{NH}_2 \rightarrow \text{N}_2\text{H}_2 + \text{H}$, and we adopt the Klippenstein et al. (2009) theoretical rate-coefficient expression of $7.07 \times 10^{-10} T^{-0.272} \exp(39/T)$ for this reaction. In scheme (6), the rate-limiting step is $\text{N}_2\text{H}_3 + \text{M} \rightarrow \text{N}_2\text{H}_2 + \text{H} + \text{M}$, where we take the rate coefficient from the theoretical calculations of Dean & Westmoreland (1987) and Hwang & Mebel (2003; see Supplementary Table S1). Note that these two reaction schemes—and all other potential $\text{NH}_3\text{--N}_2$ conversion schemes—are somewhat speculative and rely on rate coefficients derived from theoretical calculations rather than laboratory measurements. As a whole, the kinetics of nitrogen compounds is less well understood than that of the C–H–O system (see Moses et al. 2010 for further discussion).

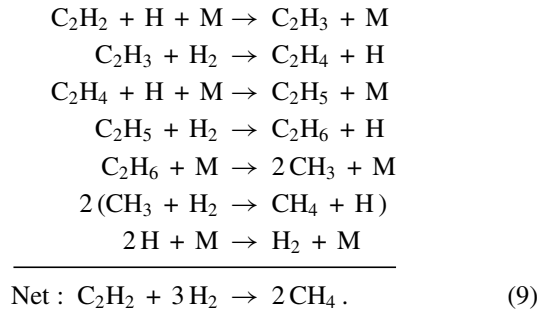
After conversion of NH_3 to N_2 is first quenched (at $\sim 1600 \text{ K}$ in the HD 189733b models, and at $\gtrsim 1700 \text{ K}$ in the HD 209458b models), the disequilibrium abundance of NH_3 affects the abundances of other nitrogen-bearing constituents, often at altitudes well below their ultimate quench points. HCN is a prime example. The HCN mole fraction departs from equilibrium at the first $\text{NH}_3\text{--N}_2$ quench point, but HCN remains in a pseudoequilibrium with NH_3 , CH_4 , and H_2 until its final quench point at higher altitudes. The dominant scheme involved in the $\text{NH}_3 \rightarrow \text{HCN}$ conversion in our cooler HD 189733b models is



This scheme is the reverse of the dominant $\text{HCN} \rightarrow \text{NH}_3$ conversion scheme derived for Jupiter's deep troposphere (Moses et al. 2010), although the rate-limiting step in the above scheme (7) for our exoplanet modeling is $\text{CH}_3\text{NH}_2 + \text{H} \rightarrow \text{CH}_2\text{NH}_2 + \text{H}_2$. We adopt the Dean & Bozzelli (2000) theoretically derived rate coefficient of $9.3 \times 10^{-16} T^{1.5} \exp(-2750/T) \text{ cm}^3 \text{ s}^{-1}$ for this rate-limiting reaction. On the warmer HD 209458b, HCN exchanges carbon with CO, as well as with CH_4 , and HCN is quenched when the following scheme becomes ineffective:



Some molecules like C_2H_2 quench at very high altitudes or are never truly quenched, as kinetic processes continue to affect their abundances throughout the atmospheric column, even when photolyzing radiation is absent. The dominant mechanism controlling the interchange of C_2H_2 and CH_4 in our models is the following scheme or its reverse:



The rate-limiting step in this scheme is either C_2H_6 thermal decomposition or $\text{H}_2 + \text{C}_2\text{H}_5 \rightarrow \text{C}_2\text{H}_6 + \text{H}$, depending on local pressure–temperature conditions.

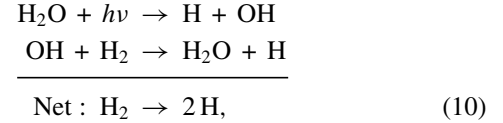
In all, transport-induced quenching can have a significant effect on the predicted abundances of species like CH_4 , NH_3 , HCN, and C_2H_2 on hot Jupiters. Given the overall uncertainties in the thermal structure, eddy diffusion coefficients, kinetic rate coefficients, and effects from horizontal transport, the quantitative predictions from our kinetics and transport models should not be taken too seriously. However, the general behavior in the models should be heeded—the column abundance of these species will likely be enhanced over equilibrium predictions (and in some cases significantly enhanced), and transport-induced quenching is more significant for cooler planets or atmospheric regions.

We now move on to discuss the effects of the photochemistry that is initiated when ultraviolet photons are absorbed by atmospheric constituents.

3.3. Photochemistry of Oxygen Species

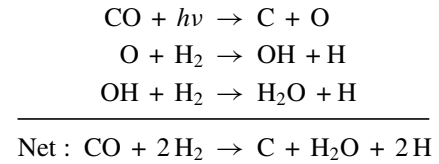
Figure 4 shows vertical profiles of the major oxygen-bearing species in our nominal thermo/photochemical kinetics and transport models. Photolysis of the major parent molecules CO and H_2O drives much of the oxygen chemistry. Water photolysis in particular is a key component of exoplanet photochemistry, as it sets up a catalytic cycle that destroys H_2 and

produces H:

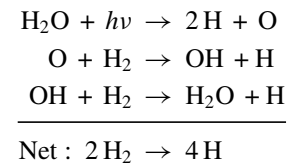


where $h\nu$ represents an ultraviolet photon. Water is recycled with this efficient scheme, but H_2 is destroyed, resulting in a huge net production rate for atomic H, which then replaces H_2 as the dominant atmospheric constituent at high altitudes (see Figure 4). This transition from H_2 to H likely signals a transition into the high-temperature thermosphere on hot Jupiters, as no potential molecular coolants survive when atomic H becomes the dominant constituent at high altitudes (see also García Muñoz 2007). Atomic species therefore are expected to dominate in the thermospheres of these close-in transiting planets (e.g., Yelle 2004; García Muñoz 2007; Koskinen et al. 2010), which might help explain the lack of obvious H_2 emission in far-ultraviolet dayglow observations of HD 209458b (France et al. 2010). From a column-integrated sense, scheme (10) is significantly more important as a source of atomic H than direct H_2 photodissociation. Atomic H flows downward from its production region and remains at abundances greatly in excess of equilibrium until it reaches altitudes marked by its mole-fraction minimum shown in Figure 4, near 0.01–0.1 bar on both planets, at which point atomic H again follows its equilibrium curve to lower altitudes.

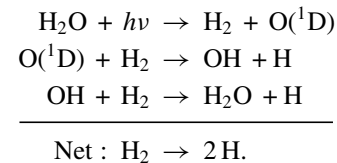
Photolysis of CO to produce C + O and photolysis of H_2O to produce $2\text{H} + \text{O}$ or $\text{O}(^1\text{D}) + \text{H}_2$ also contribute to H_2 destruction through schemes such as



and



and



Reactions of atomic H with H_2O and OH can partially recycle the H_2 , but key reactions like $2\text{H} + \text{M} \rightarrow \text{H}_2$ do not operate effectively at low pressures, and the net result is that the loss rate for H_2 exceeds the production rate at high altitudes. The H atoms produced in these mechanisms diffuse both upward and downward, where they strongly affect the abundance of other species.

Although H_2O photolysis operates effectively down to millibar regions in these models and the atomic H produced from

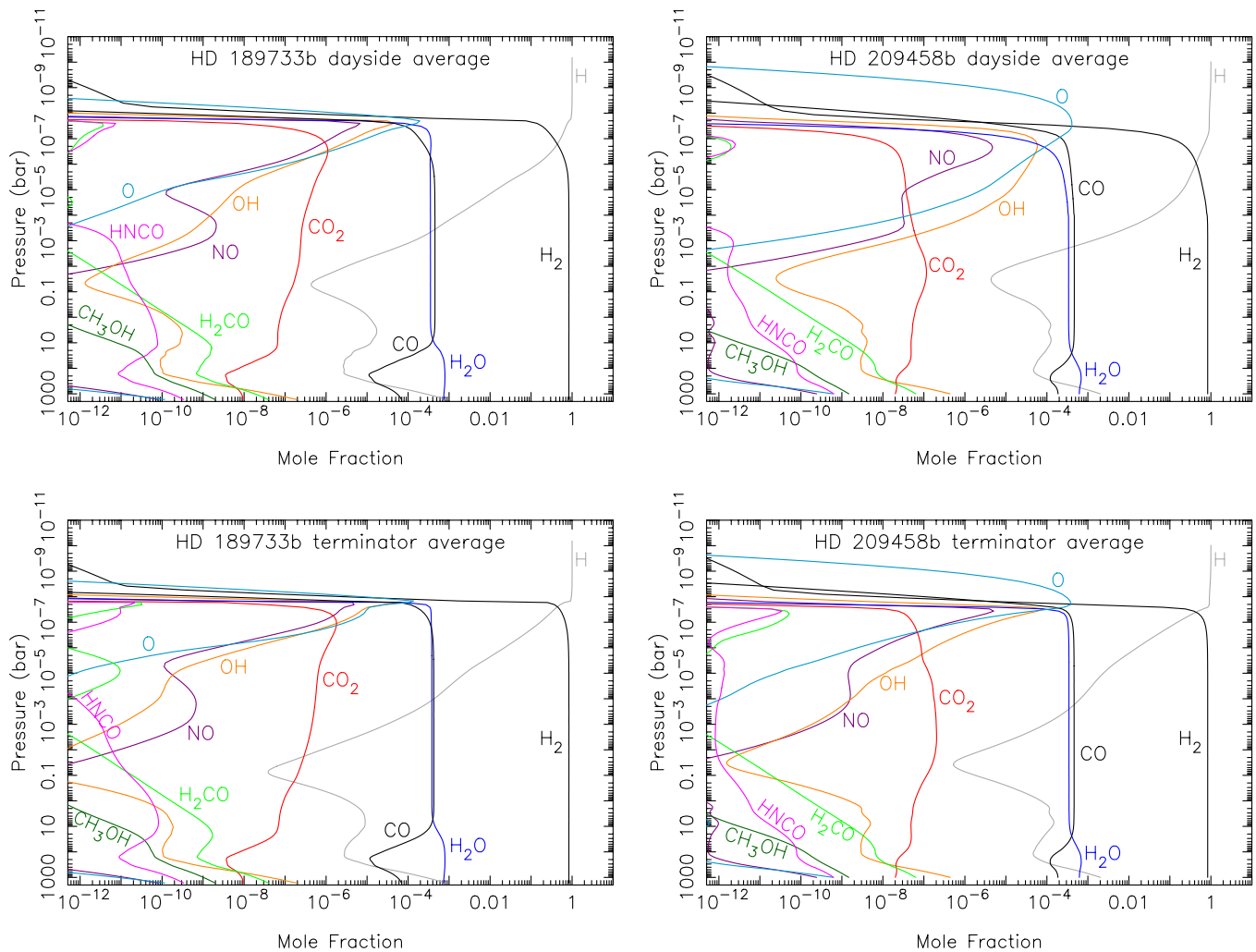


Figure 4. Mole-fraction profiles for several oxygen-bearing species in our models for HD 189733b (left) and HD 209458b (right) for dayside-average (top) and terminator-average (bottom) conditions, assuming the nominal K_{zz} profiles shown in Figure 1.

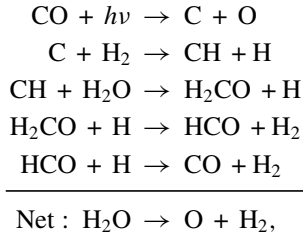
(A color version of this figure is available in the online journal.)

the photolysis continues to attack H_2O , water is not permanently removed from this atmospheric region because of the efficient recycling by the reaction $\text{OH} + \text{H}_2 \rightarrow \text{H}_2\text{O} + \text{H}$. Note that rapid replenishment by diffusion from other altitudes can also play an important role in maintaining H_2O for our models with cooler stratospheric temperature profiles (see also Line et al. 2010). As an example, water is in approximate chemical equilibrium at pressures greater than ~ 0.1 bar in the HD 189733b dayside-average model shown in Figure 4; however, the transport timescales are shorter than the net photochemical loss timescales for H_2O in the region from ~ 0.1 bar to a few μbar , so that atmospheric mixing “quenches” the H_2O mole fraction and keeps it roughly constant through this region. Since the H_2O mole fraction quenches at a value similar to the equilibrium value and since equilibrium would keep the H_2O mole fraction constant in this region anyway, the water profile for the thermo/photochemical kinetics and transport model is quite similar to the thermochemical equilibrium profile for our HD 189733b models. For our much warmer dayside HD 209458b model, equilibrium chemistry dominates the H_2O profile over a much more expanded altitude range—transport is only important at high altitudes, and only if the eddy diffusion coefficient is large. This effect can be seen from detailed comparisons of the H_2O

profile from the HD 209458b dayside-average model in Figure 3 in which it is assumed that $K_{zz} = 10^9 \text{ cm}^2 \text{ s}^{-1}$, in contrast to the H_2O profile in Figure 4 from an otherwise similar HD 209458b dayside-average model in which it is assumed that mixing is more vigorous at high altitudes (see the nominal K_{zz} profile from Figure 1). The $K_{zz} = 10^9 \text{ cm}^2 \text{ s}^{-1}$ model has the H_2O profile closely following equilibrium, whereas our higher K_{zz} nominal model has water being carried to higher altitudes before its eventual chemical destruction. However, this additional H_2O from transport processes does not add much to the column abundance of H_2O on the planet. The net result on both the cooler and warmer classes of planets is an H_2O profile that closely follows the equilibrium profile through the observable regions of the atmosphere.

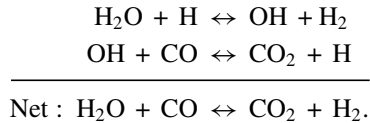
Carbon monoxide also survives in the atmospheres of HD 189733b and HD 209458b despite rapid loss from $\text{H} + \text{CO} + \text{M} \rightarrow \text{HCO} + \text{M}$, from $\text{OH} + \text{CO} \rightarrow \text{CO}_2 + \text{H}$, and from photolysis by EUV photons that continues down to mbar levels. The first two reactions dominate the column-integrated CO loss in the stratosphere; the HCO produced in the first reaction efficiently reacts with H to reform CO, and the CO_2 produced in the second reaction efficiently reacts with H to reform CO, so carbon monoxide is readily recycled on both HD 189733b and

HD 209458b. Even in the case of CO photolysis, some recycling pathways such as the following can operate



allowing CO to persist. However, these recycling schemes are not 100% effective, and some of the CO photodestruction leads to the production of other species. Atomic carbon and oxygen released from CO photolysis at high altitudes can remain as C and O, for example, and some of the O can lead to H₂O production through reactions like $\text{O} + \text{H}_2 \rightarrow \text{OH} + \text{H}$ followed by $\text{OH} + \text{H}_2 \rightarrow \text{H}_2\text{O} + \text{H}$, while some of the C can go toward producing hydrocarbons and HCN (see below; Liang et al. 2004; Line et al. 2010; Zahnle et al. 2011). As with H₂O, the CO profiles are expected to closely follow the equilibrium profiles, except at high altitudes, where the CO will be converted to C, O, and H₂O (i.e., for cooler-temperature models) or where high eddy diffusion coefficients may allow it to be transported to higher altitudes than equilibrium models predict (i.e., for our nominal dayside HD 209458b model).

The photochemistry of CO₂ is not particularly interesting, as CO₂ remains in equilibrium with CO and H₂O throughout most of the atmosphere via the reaction scheme:

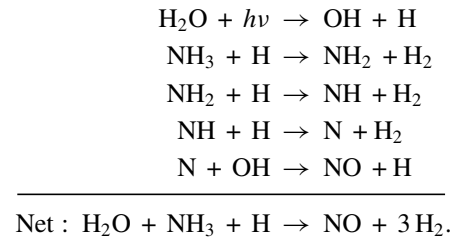


Some additional CO₂ in excess of equilibrium is produced at high altitudes from CO photochemistry on HD 189733b and/or from transport on HD 209458b, but the CO₂ profiles on both planets remain close to equilibrium predictions.

Aside from atomic H, few photochemical products build up from the chemistry of oxygen-bearing species in our hot-Jupiter models. Some O, OH, NO, and even O₂ and HNCO molecules are produced at high altitudes and diffuse downward; however, the photochemical lifetimes of these species are quite short, and they are not likely to achieve column abundances great enough to be detectable at visible or infrared wavelengths with current technologies unless the planet's metallicity is enhanced greatly over solar (see Figure 4 and Table 1). Atomic O is produced from the reaction of H with OH to form $\text{O} + \text{H}_2$, with lesser contributions from H₂O, OH, and CO photolysis. Atomic O is lost predominantly from $\text{O} + \text{H}_2 \rightarrow \text{OH} + \text{H}$. Because atomic O is not readily destroyed by H, it can be transported up to its homopause level in our HD 209458b models, unlike the situation for molecular species. Some fraction of the O column will then make it into the thermosphere on planets with vigorous vertical mixing, where high thermospheric temperatures and hydrodynamic winds or other processes may then distribute the atomic O over a large radial distance (Lecavelier des Etangs et al. 2004; Yelle 2004; Tian et al. 2005; García Muñoz 2007; Penz et al. 2008; Murray-Clay et al. 2009; Lammer et al. 2009), which will increase the likelihood of its detection at ultraviolet wavelengths (e.g., see Vidal-Madjar et al. 2004; Ben-Jaffel & Hosseini 2010; Koskinen et al. 2010). Even in

cases where K_{zz} is small in the upper atmosphere, the dynamical wind from the hydrodynamic escape—which is not included in our models—may then dominate over molecular diffusion in controlling the behavior of heavy atmospheric constituents, so that the concept of a homopause may not actually be appropriate for close-in transiting planets. The dominant OH production mechanism is $\text{H} + \text{H}_2\text{O} \rightarrow \text{OH} + \text{H}_2$, with the atomic H coming from the H₂ catalytic destruction scheme (10) described above. The reverse of this reaction is its dominant loss mechanism. In general, the cooler the stratosphere, the larger the increase in the OH abundance over equilibrium predictions.

The main production mechanism for NO is $\text{N} + \text{OH} \rightarrow \text{NO} + \text{H}$. The OH derives from water, and the N can come from either N₂ photolysis or from NH₃ via schemes such as the following:

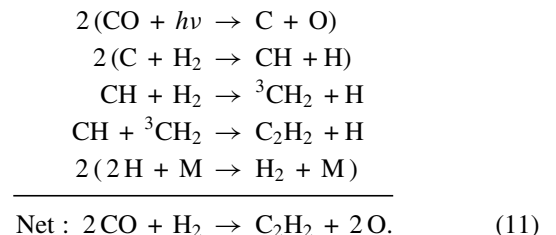


The double-peak appearance in the NO mole fraction is due to the dominance of the N₂ photolysis pathway in the upper stratosphere and the NH₃ pathway in the middle stratosphere. The NO is lost through reactions with N to form $\text{N}_2 + \text{O}$, with C to form $\text{N} + \text{CO}$ and/or $\text{CN} + \text{O}$, through photolysis to form $\text{N} + \text{O}$, and through reaction with atomic H. Molecular oxygen is produced through the reaction $\text{O} + \text{OH} \rightarrow \text{O}_2 + \text{H}$ and is lost through the reverse of this reaction.

As a general rule of thumb, photochemistry in these warm, highly irradiated stratospheres favors small molecules and/or molecules with strong bonds. Our results are consistent with other exoplanet photochemical models (Liang et al. 2003, 2004; Line et al. 2010; Zahnle et al. 2011) in that we see little photochemical production of molecules like H₂CO, CH₃OH, H₂CCO, or CH₃CHO.

3.4. Photochemistry of Carbon Species

The photochemistry of carbon species is more interesting than that of oxygen species, as the primary parent molecule CH₄ has weaker bonds. Several carbon-bearing photochemical products can build up in the atmospheres of extrasolar giant planets. Figure 5 shows vertical profiles of the major carbon species in our nominal thermo/photochemical kinetics and transport models. Carbon photochemistry is initiated by CO photolysis at high altitudes and by hydrogen abstraction from methane at lower altitudes. At pressures less than $\sim 1 \mu\text{bar}$, much of the C that is released from CO photolysis remains as atomic C, although some acetylene and other hydrocarbon production can occur through schemes such as



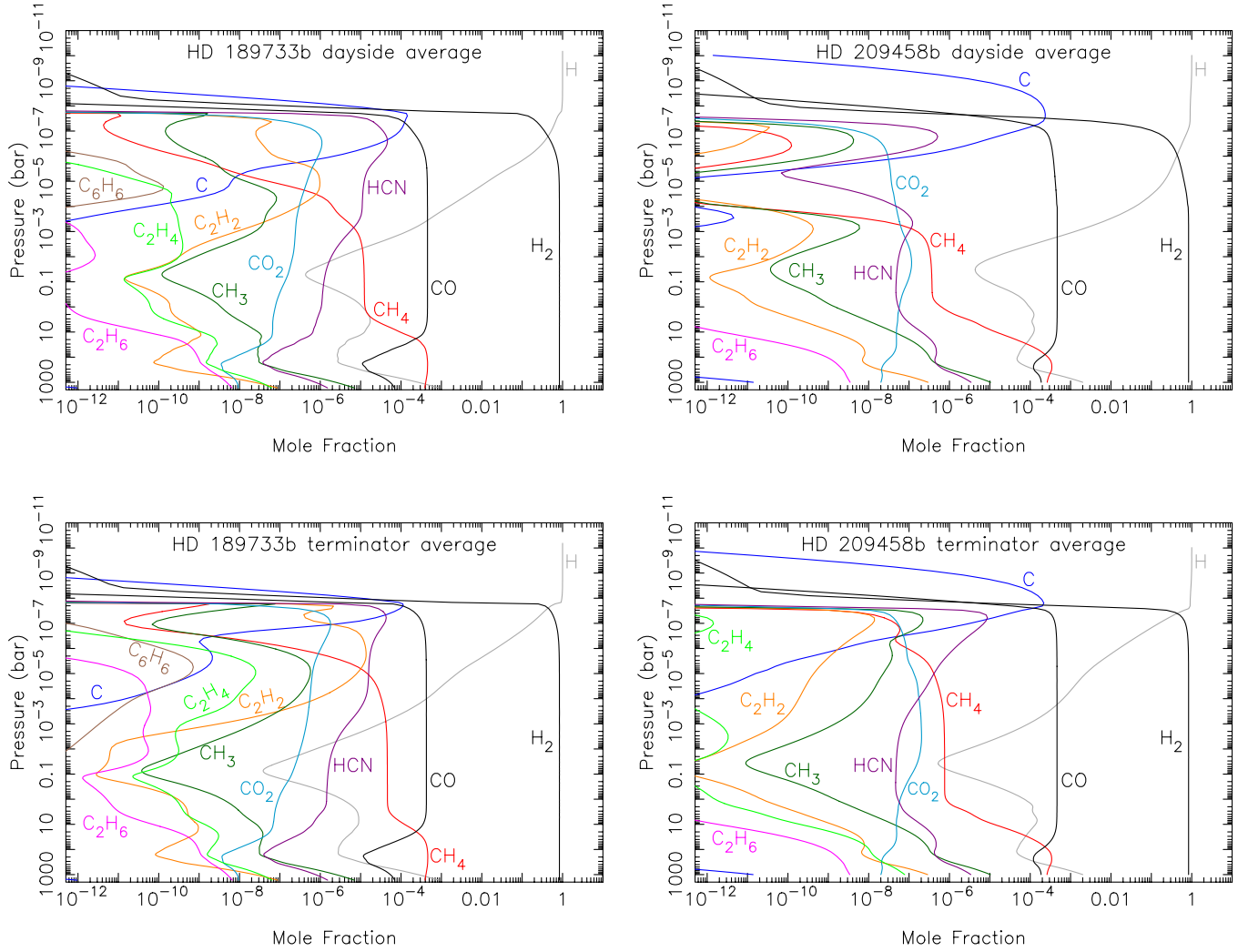
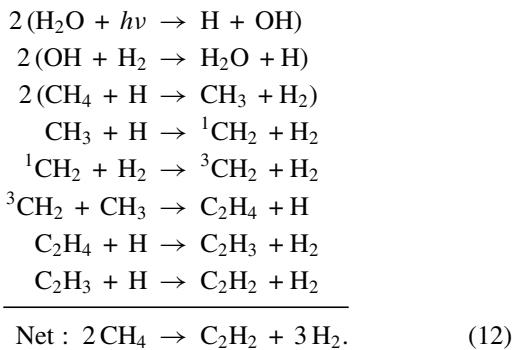


Figure 5. Mole-fraction profiles for several carbon-bearing species in our models for HD 189733b (left) and HD 209458b (right) for dayside-average (top) and terminator-average (bottom) conditions, assuming the nominal K_{zz} profiles shown in Figure 1.

(A color version of this figure is available in the online journal.)

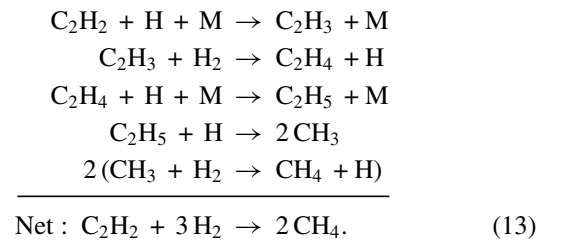
At greater pressures (and in particular where CH_4 or CH_3 become more abundant than atomic C), acetylene and other hydrocarbons are produced from methane destruction through pathways such as



Note the importance of H_2O photolysis in providing the atomic H used to destroy the CH_4 . These pathways are efficient enough that C_2H_2 becomes the dominant hydrocarbon at high altitudes under certain conditions in our models (see Figure 5).

Acetylene is more effectively hydrogenated with increasing pressure, such that the following scheme acts to remove the

C_2H_2 and recycle the methane at middle-stratospheric pressures:



This scheme, rather than photolysis, is responsible for removing C_2H_2 from the middle and lower stratosphere, as the C_2H_2 photolysis products tend to simply recycle the C_2H_2 .

Other C_2H_x hydrocarbons are less able to survive the large background H abundance. Ethane is produced in the stratosphere through $2\text{CH}_3 + \text{M} \rightarrow \text{C}_2\text{H}_6 + \text{M}$ and through $\text{C}_2\text{H}_5 + \text{H}_2 \rightarrow \text{C}_2\text{H}_6 + \text{H}$. Ethane is lost through hydrogen abstraction by atomic H ($\text{C}_2\text{H}_6 + \text{H} \rightarrow \text{C}_2\text{H}_5 + \text{H}_2$), followed by $\text{H} + \text{C}_2\text{H}_5 \rightarrow 2\text{CH}_3$, and eventual methane production. The column abundance of photochemically produced ethane is quite small in our models. Ethylene (C_2H_4) fares a bit better: it is produced predominantly from $\text{C}_2\text{H}_3 + \text{H}_2 \rightarrow \text{C}_2\text{H}_4 + \text{H}$ (see some of the C_2H_2 production schemes above) and is lost from the reverse

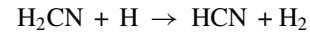
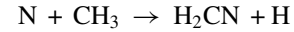
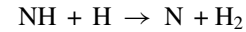
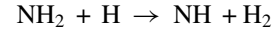
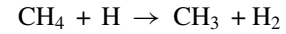
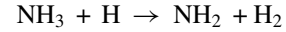
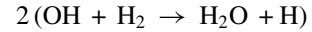
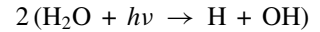
of this reaction (heading toward C_2H_2 production), as well as $H + C_2H_4 + M \rightarrow C_2H_5 + M$, to eventually form methane. Although the mole fraction of C_2H_4 can exceed that of C_2H_2 at the C_2H_2 mole-fraction minimum near $0.1\text{--}10^{-2}$ bar in some of our models, the peak C_2H_4 mole fraction never approaches that of the peak C_2H_2 mole fraction, and the column abundance of C_2H_4 is intermediate between that of C_2H_2 and C_2H_6 in our HD 189733b and HD 209458b models (see Table 1).

Although our kinetics is far from complete for C_3 -to- C_6 species, we do attempt to track the production and loss of some complex hydrocarbons. The dominant C_3 hydrocarbon in our models is actually the C_3H_2 radical. This result may be due to our insufficient knowledge of C_3H_x kinetics, and we encourage further laboratory and theoretical studies of the fate of C_3H_x species under the low-pressure, high-temperature, reducing conditions in the relevant regions of extrasolar-planet atmospheres. Both CH and C readily insert into C_2H_2 (e.g., Berman et al. 1982; Canosa et al. 1997; Haider & Husain 1993; Kaiser et al. 2001; Casavecchia et al. 2001; Mebel et al. 2007), and these insertion reactions likely dominate the production of C_3 hydrocarbons on extrasolar giant planets, but the fate of the C_3H_2 , C_3H , and C_3 radicals produced from these reactions is unclear. We implicitly assume that the C_3 and C_3H radicals that are produced from the reaction of C with C_2H_2 quickly end up as C_3H_2 —an assumption that may only be correct at altitudes where H_2 is the dominant atmospheric constituent. The main loss process for C_3H_2 in our models is $H + C_3H_2 + M \rightarrow C_3H_3 + M$. The resulting propargyl radicals can be photolyzed to recycle the C_3H_2 , can react with atomic H to reform C_2H_2 , can react with H_2 or H to form C_3H_4 , or can react with other C_3H_x radicals to form C_6 hydrocarbons and eventually benzene.

Although benzene is not a major constituent in our models, it can reach mole fractions of $0.1\text{--}1$ ppb in the few-microbar region in some of our HD 189733b models; however, benzene does not survive in the warmer HD 209458b models. While ppb levels are by no means sufficient for C_6H_6 condensation on HD 189733b, it does suggest that polycyclic aromatic hydrocarbon (PAH) formation could possibly occur at high altitudes on cooler transiting exoplanets, which could ultimately lead to the formation of a “soot” aerosol layer, as has been suggested by Zahnle et al. (2011). In contrast, PAH formation will be strongly suppressed on planets with strong stratospheric thermal inversions (see also Liang et al. 2004). Our neutral chemistry is not particularly conducive for soot formation, even under HD 189733b conditions, but it is possible that photoionization of N_2 or other species could lead to the production of high-molecular-weight ions and photochemically produced aerosols through a Titan-like ion-chemistry process (e.g., Waite et al. 2007, 2009; Imanaka & Smith 2007; Vuitton et al. 2007, 2008), although it is also possible that the high abundance of H_2O and/or CO and the low abundance of CH_4 at high altitudes on highly irradiated exoplanets could short-circuit this process. The potential for ion chemistry playing a role in the formation of complex species in extrasolar-giant-planet atmospheres deserves further study.

Unlike the case for CO and H_2O , methane can be efficiently destroyed and not recycled in the upper atmospheres of HD 189733b and HD 209458b. Some of the carbon ends up in C_2H_2 and other hydrocarbons, as well as CO and C, but cross reactions with nitrogen species become a key mechanism for removing CH_4 from the upper atmosphere. Hydrogen cyanide is the dominant product of this coupled carbon–nitrogen chemistry. From a column-integrated standpoint, the dominant pho-

tochemical scheme that permanently converts CH_4 into HCN in the stratospheres of our exoplanet models is

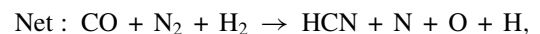
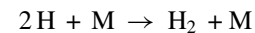
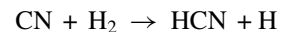
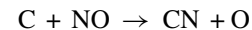
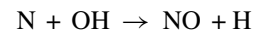
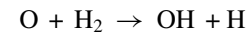
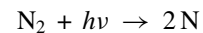
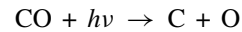


Hydrogen cyanide then becomes a major disequilibrium product in exoplanet atmospheres and can replace methane as the second most abundant carbon-bearing species at high altitudes.

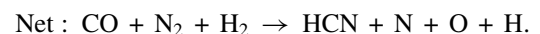
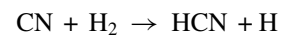
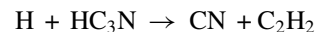
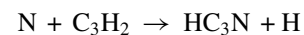
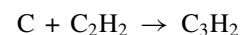
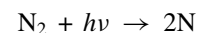
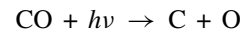
As is the case for oxygen compounds, the photochemistry of carbon compounds is more effective for cooler exoplanets, both because of the larger abundance of CH_4 from transport-induced quenching and because the lower temperatures allow disequilibrium products to survive more readily. The dominant carbon-bearing photochemical products are HCN, C_2H_2 , C, and CH_3 , with some CO_2 being produced at high altitudes.

3.5. Photochemistry of Nitrogen Species

Nitrogen photochemistry parallels that of carbon chemistry: N_2 , like CO, is a high-altitude source, and NH_3 , like CH_4 , is a critical transport-quenched species that drives photochemistry throughout the bulk of the stratosphere. Figure 6 shows vertical profiles of the major nitrogen-bearing species in our nominal thermo/photochemical kinetics and transport models. At high altitudes, nitrogen photochemistry is initiated by N_2 photolysis through schemes such as



where the resulting HCN and N are significant high-altitude products. On the cooler HD 189733b, additional speculative processes involving HC_3N rather than NO might contribute at high altitudes:



Molecular nitrogen is quite stable on HD 189733b and HD 209458b. Although N_2 can combine with atomic H to form

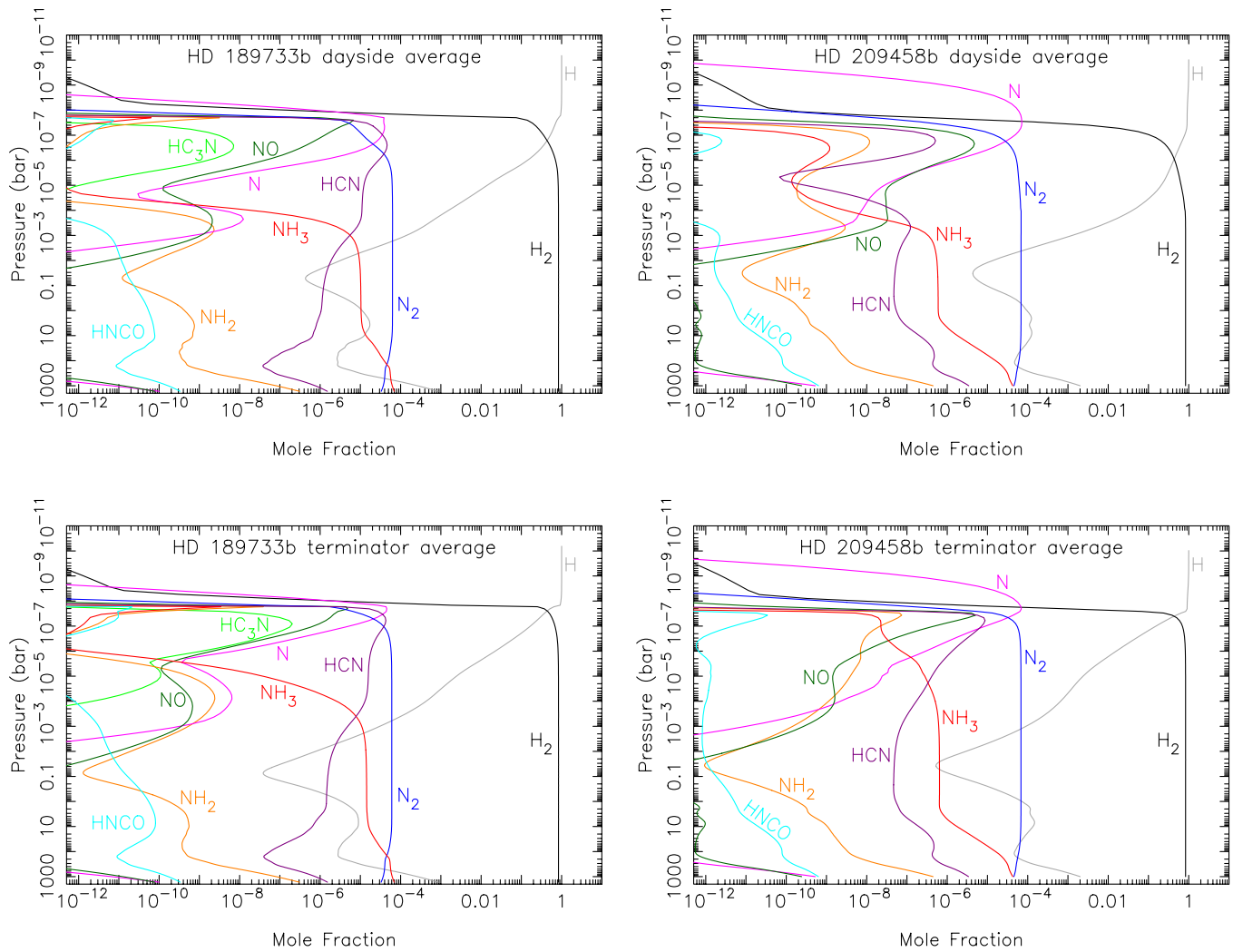
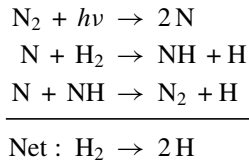


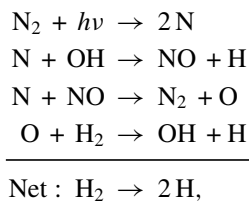
Figure 6. Mole-fraction profiles for several nitrogen-bearing species in our models for HD 189733b (left) and HD 209458b (right) for dayside-average (top) and terminator-average (bottom) conditions, assuming the nominal K_{zz} profiles shown in Figure 1.

(A color version of this figure is available in the online journal.)

NNH, thermal decomposition of this unstable species acts to recycle the N_2 throughout the stratosphere. At high altitudes, the strong $N\equiv N$ bond can be destroyed by photolysis or attacked by atomic C, H, and O to form atomic N, which then can become the dominant nitrogen species at high altitudes. However, N_2 is also recycled through schemes such as



and



where catalytic destruction of H_2 is the net result of both recycling schemes. Throughout much of the stratosphere, N_2

is shielded from photolysis by a larger surrounding column of H_2 .

Ammonia has much weaker bonds and is less stable than N_2 , so much of the interesting nitrogen chemistry in our models involves NH_3 . Throughout the bulk of the stratosphere, NH_3 destruction leads to HCN production through scheme (14) discussed in Section 3.4. This scheme is efficient enough—and HCN is recycled readily enough—that HCN can take over from NH_3 and CH_4 as important nitrogen and carbon carriers in the upper stratosphere. The main loss process for HCN in hot-Jupiter stratospheres is the reaction $H + HCN \rightarrow CN + H_2$, with a much lesser contribution from HCN photolysis to form $CN + H_2$. The CN produced by these processes reacts with H_2 to reform HCN, so HCN recycling is prevalent.

Complex nitriles are also formed from photochemistry on cooler extrasolar planets like HD 189733b. For example, some of the CN produced in the $H + HCN$ reaction can react with C_2H_2 to form HC_3N , or some of the CH_3 produced from hydrogen abstraction of methane can react with HCN to form CH_3CN . These nitriles tend to be unstable in a background bath of H, and their destruction pathways tend to reproduce the HCN, so they are nowhere near as abundant as HCN in our HD 189733b models. However, as with benzene

and potential PAHs, further nitrile chemistry may produce condensable products, particularly on colder exoplanets. On the other hand, complex nitriles will be very unstable on planets like HD 209458b that have a strong stratospheric thermal inversion. Other carbon–nitrogen bonded species, including imines and amines, are relatively unimportant in our models, although the H_2CN that is produced during the course of scheme (14) can undergo three-body recombination with H to form some CH_2NH that persists in our cooler atmospheric models. Note that nitrogen hydrides like hydrazine (N_2H_4) are unimportant in our models, unlike the situation on the much colder Jupiter.

Cross reactions between nitrogen and oxygen species can also occur in exoplanet stratospheres, leading to the production of species like NO and HNCO. The dominant schemes producing and destroying NO were discussed in Section 3.3. HNCO is produced predominantly through the reaction $\text{NH}_2 + \text{CO} \rightarrow \text{HNCO} + \text{H}$, where the NH_2 derives from hydrogen abstraction of ammonia by atomic H. The dominant loss for HNCO is reaction with atomic H in the reverse of the main production reaction.

The dominant nitrogen-bearing photochemical products in our exoplanet models are HCN, N, NO, and NH_2 . As with oxygen and carbon photochemistry, cooler planets tend to have more abundant and more varied disequilibrium nitrogen species than warmer planets. This tendency results from the larger abundance of photochemically active, transport-quenched species like NH_3 on cooler planets and from the greater stability of the photochemical products at low temperatures.

3.6. Sensitivity to Temperature

The atmospheric thermal structure can strongly affect the abundance of disequilibrium constituents. As shown in Figure 3, high temperatures in the stratospheres of transiting hot Jupiters can allow photochemically produced species to react chemically with other atmospheric constituents to drive the composition back toward equilibrium. Disequilibrium compositions are thus difficult to maintain on planets like HD 209458b that have strong thermal inversions. In contrast, thermochemical kinetics is inhibited when stratospheric temperatures are cooler, so that photochemically produced species are more likely to survive on HD 189733b and other exoplanets without stratospheric thermal inversions. Temperatures in the deep atmosphere also affect the abundance of disequilibrium constituents by controlling where transport-induced quenching begins to operate. Figure 7 illustrates the importance of this effect for key transport-quenched species like CH_4 , NH_3 , and HCN.

In Figure 7, all models have the same constant-with-altitude eddy $K_{zz} = 10^9 \text{ cm}^2 \text{ s}^{-1}$ profile, but the thermal structure is different for each model (see Figure 2 for the adopted temperature profiles). In general, colder temperatures at depth imply that transport will be able to compete with thermochemical kinetics at greater pressures; the quench point will therefore be deeper on colder planets, and the mole fraction of the quenched species will be larger. This effect can be seen with the HD 189733b models shown in Figure 7, where the coldest western-terminator-average model has a CH_4 quench point near the ~ 7 bar, ~ 1485 K level, whereas the warmest projected-area-weighted dayside-average models have quench points near 1.9 bar, ~ 1522 K. The resulting CH_4 quenched mole fraction is a factor of ~ 10 greater for the cooler western-terminator model than for the warmer dayside-average model. Ammonia quenches at even greater pressures and temperatures, at which point the temperature profiles are more uniform (see Figure 2),

so that the differences between models are less pronounced. The HCN profiles are more complicated because the quenched abundances of both NH_3 and CH_4 affect the HCN abundance, and HCN is photochemically produced at high altitudes, but Figure 7 suggests that HCN first quenches in the 10–30 bar region, where the GCM simulations of Showman et al. (2009) exhibit western-terminator-average temperatures that are actually warmer than the dayside-average temperatures at these pressures. As such, the western-terminator-average model has a smaller quenched HCN abundance than the dayside-average models. The 1D “4pi” profile from Fortney et al. (2006, 2010) is the coolest of all our models at 10–30 bars, resulting in the largest quenched HCN mole fraction in this model. Given the lack of constraints on temperatures and eddy diffusion coefficients at depth, the quantitative results for the abundance of quenched species have significant uncertainty in our models; moreover, horizontal advection timescales may be shorter than chemical timescales at pressures greater than a few mbar, acting to homogenize the composition longitudinally (see Section 3.8).

For HD 209458b, the presence of high stratospheric temperatures, particularly on the dayside, is the biggest factor in controlling the composition, as the disequilibrium molecular constituents do not survive in the middle and upper stratosphere. The cooler the atmosphere is at high altitudes, the more likely disequilibrium species are to survive to these altitudes. Note that the lack of UV photons in the nightside-average model shown in Figure 7 also helps keep disequilibrium molecules present at high altitudes. Even without a strong thermal inversion at the terminators of HD 209458b, stratospheric temperatures are considerably higher than on HD 189733b, enabling thermochemical kinetic processes to destroy disequilibrium constituents. Temperatures at depth are also much warmer on HD 209458b than on HD 189733b, due to the different luminosities of the host stars. Transport-induced quenching is therefore less effective on HD 209458b than on HD 189733b, and the predicted quenched abundances of CH_4 , NH_3 , and HCN are correspondingly reduced.

The abundances of HCN and CH_4 are particularly sensitive to temperature, whereas species like H_2O , CO, and CO_2 tend to follow more closely their equilibrium profiles such that these species are more sensitive to metallicity than to temperature on HD 189733b and HD 209458b. This conclusion will differ for colder planets like GJ 436b that are in the CH_4 rather than CO stability field.

3.7. Sensitivity to Eddy Diffusion Coefficients

The model results are also sensitive to the assumed eddy diffusion coefficients, again because of the potential importance of transport-induced quenching on extrasolar giant planets. Figure 8 demonstrates this sensitivity. For larger eddy diffusion coefficients, transport-induced quenching becomes effective at deeper pressures, leading to larger mole fractions of quenched species. Larger K_{zz} values also allow molecular constituents to be carried to higher altitudes. Both these processes contribute to enhanced abundances of photochemically derived products when atmospheric mixing is more vigorous. For example, when quenched species like CH_4 and NH_3 are more abundant and carried to higher altitudes, photochemical products like HCN and other nitriles, and C_2H_2 and other hydrocarbons can build up over a larger column. The H_2 -to-H conversion level also changes with K_{zz} , which can have a significant effect on all molecular abundances. Minor heavy constituents like complex hydrocarbons and nitriles are particularly affected by K_{zz} , as

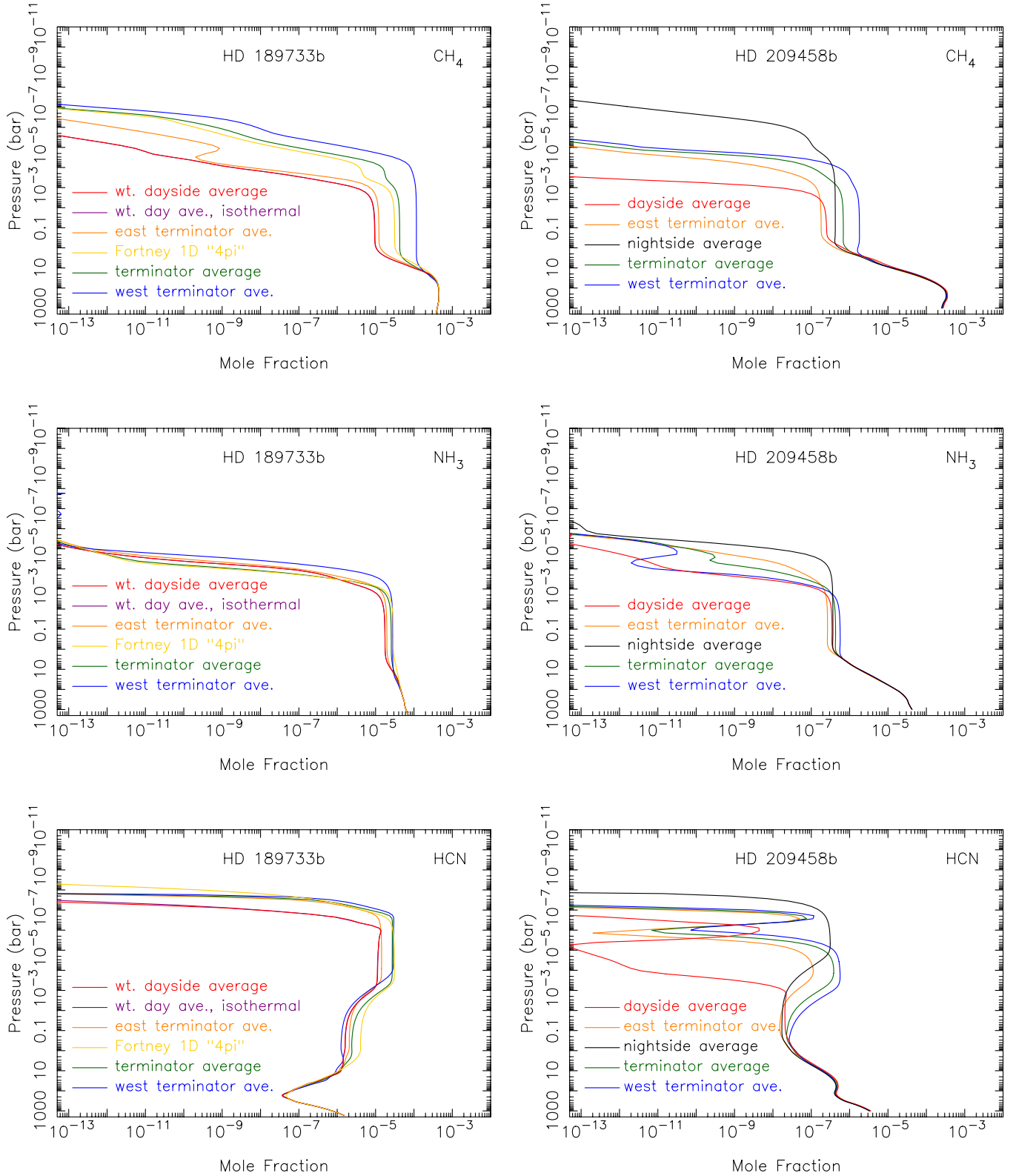


Figure 7. Mole-fraction profiles for CH_4 (top), NH_3 (middle), and HCN (bottom) in our models for HD 189733b (left) and HD 209458b (right) for different assumptions about the atmospheric thermal structure (as labeled, and see Figure 2). All models assume a constant $K_{zz} = 10^9 \text{ cm}^2 \text{ s}^{-1}$.

(A color version of this figure is available in the online journal.)

these species often depend nonlinearly on the abundance of parent molecules like CH_4 and NH_3 . Note from Figure 8 that if K_{zz} is sufficiently high, there is even a quench point for H_2O and CO that differs from the equilibrium solution.

General circulation models for highly irradiated hot Jupiters (see Showman et al. 2009, 2010, and references therein) suggest relatively strong vertical winds, which according to our assumptions could lead to potentially vigorous mixing at

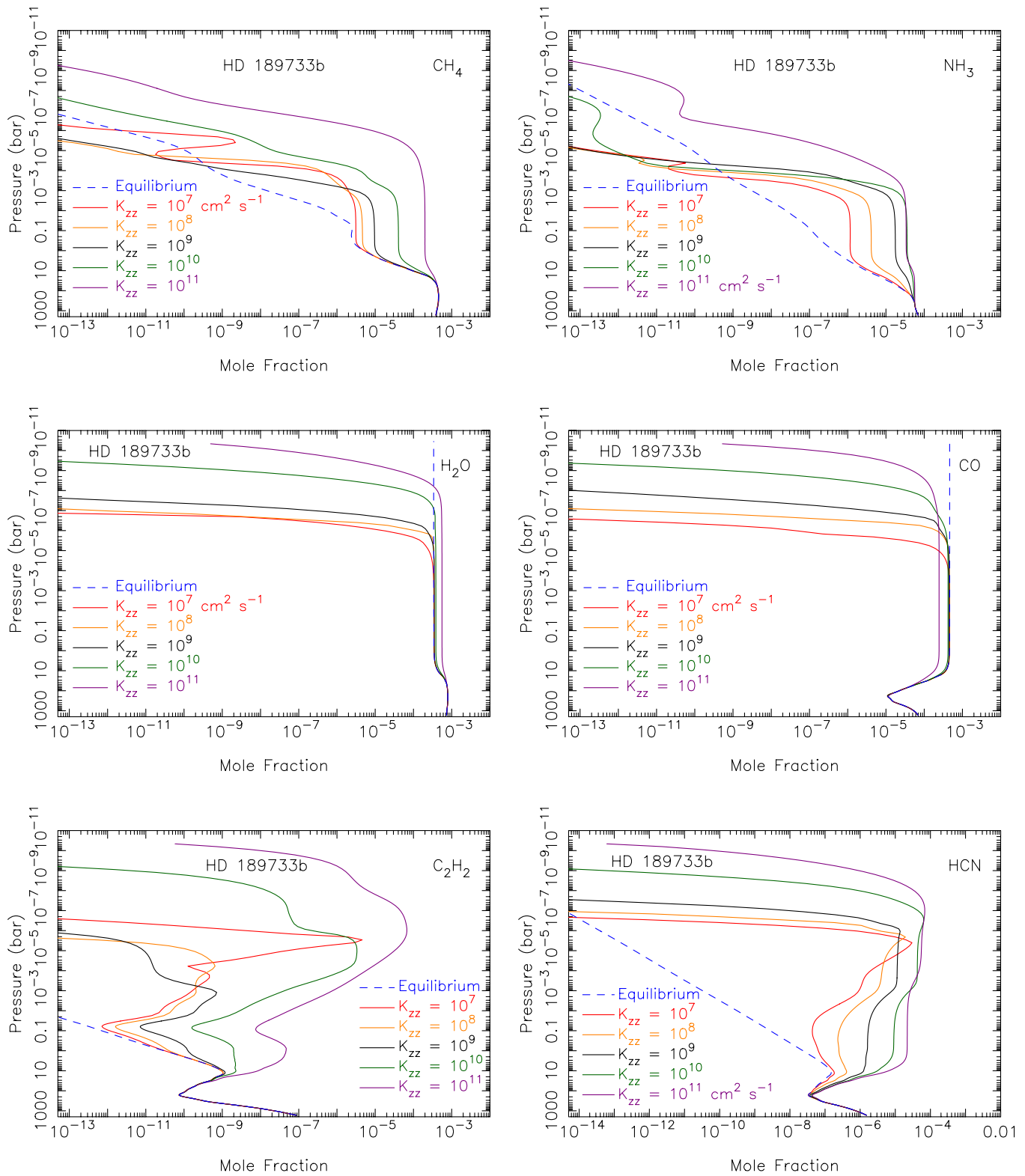


Figure 8. Mole-fraction profiles for CH_4 (top left), NH_3 (top right), H_2O (middle left), CO (middle right), C_2H_2 (bottom left), and HCN (bottom right) in our dayside-average HD 189733b model with an isothermal extension at high altitudes (see Figure 2), for different assumptions about the eddy K_{zz} profile (as labeled). Larger K_{zz} imply greater vertical mixing, deeper quench points, and larger quenched abundances.

(A color version of this figure is available in the online journal.)

pressures less than ~ 100 bar (i.e., Figure 1). We have assumed that convection in the adiabatic portion of the atmosphere at greater depth also contributes to vigorous vertical mixing (see Stone 1976). Transport-induced quenching is then very impor-

tant, and quenched disequilibrium species and their photochemical products are abundant. In contrast, Youdin & Mitchell (2010) suggest that weak turbulent mixing in extrasolar-giant-planet atmospheres could slow the cooling rate of the atmosphere and

might explain the large, “inflated” radii of some hot-Jupiter atmospheres. Youdin & Mitchell (2010) further suggest that K_{zz} values greater than $10^7 \text{ cm}^2 \text{ s}^{-1}$ would overinflate hot-Jupiter radii beyond what can be supported by observations—they favor much smaller K_{zz} values of $(1-5) \times 10^3 \text{ cm}^2 \text{ s}^{-1}$ at ~ 550 bar, or in general $K_{zz} < 10^5 \text{ cm}^2 \text{ s}^{-1}$ at $P > 100$ mbar for temperatures of $T_{\text{deep}} = 1500$ K in the deep isothermal radiative region above the optically thick region of the atmosphere, similar to the few-bar-to-few-hundred-bar region for our HD 189733b temperature profiles. With the Youdin & Mitchell (2010) formalism, K_{zz} scales as T_{deep}^5 , so that K_{zz} on HD 209458b could be slightly higher by a factor of 2–3. If eddy diffusion coefficients were as small as Youdin & Mitchell (2010) suggest in the ~ 2 –500 bar region, then transport-induced quenching would be significantly suppressed in our HD 189733b and HD 209458b models, and the quenched abundances of CH_4 , NH_3 , and HCN would be quite low—more consistent with what is predicted from thermochemical equilibrium—and these species (including methane) would likely not be observable. Although waves propagating up from the deep interior and down from the weather layer may keep K_{zz} from being as low as is suggested by Youdin & Mitchell (2010), the idea of a “mechanical greenhouse” is an interesting one. Spectral observations that can unambiguously confirm the presence of CH_4 , NH_3 , or HCN at levels in excess of equilibrium could help constrain the strength of turbulent mixing in extrasolar-giant-planet atmospheres.

Given that the NH_3 quench point is likely in the adiabatic region of the deep atmosphere, it is interesting to speculate that the NH_3 abundance might eventually help provide a measure of the entropy of the adiabat, which is currently known only crudely from the planet’s radius. For a given mass, planets with larger radii have higher-entropy adiabats and lower-pressure radiative-convective boundaries. Although the entropy of the adiabat will certainly affect the NH_3 quench point, the overall uncertainties in the eddy diffusion coefficients, in the planetary metallicity, and in the kinetics of NH_3 quenching might make such a suggestion impractical.

3.8. Photochemistry and Transport Time Constants and their Implications

Because our models remain at a single solar zenith angle for the long duration of the simulation, they are not true analogs for the situation on a real planet, even if the planet is tidally locked and has one hemisphere always facing the star. Real planets have meteorology, and dynamical models indicate that strong winds will be acting on close-in transiting exoplanets to transport species zonally, meridionally, and vertically (see Showman et al. 2010 for a review of exoplanet dynamical models); zonal jets are predicted to be particularly strong, such that material is transported longitudinally across a hemisphere with a horizontal transport timescale $\tau_{\text{dyn,h}} \approx 2 \times 10^5 \text{ s}$ on HD 209458b (Cooper & Showman 2006). A parcel of gas will therefore experience variable external forcing from the continuously changing irradiation angles, and those effects can influence the chemistry. A full 3D model of the radiative, dynamical, and chemical coupling needed to describe this situation would be computationally prohibitively expensive, but simplifications such have been described by Cooper & Showman (2006) can be made to track the key chemical effects. Although we do not attempt these kinds of simulations with our simple 1D models, we can at least examine the time constants in the system and make some comments about what the time-

constant analysis implies about the composition of more realistic planetary analogs.

Cooper & Showman (2006) convincingly argue that the large CO abundance that is predicted for dayside HD 209458b will not be chemically converted to CH_4 at the terminators or in the nightside stratosphere, despite the fact that CH_4 would be favored in chemical equilibrium. Vertical transport timescales are simply much shorter than the chemical conversion timescale between CO and CH_4 . In addition, note that just as there is transport-induced quenching in the vertical direction, horizontal transport-induced quenching can also operate (Cooper & Showman 2006). Will this horizontal quenching affect photochemically produced species? One might particularly want to know whether HCN will reconvert into CH_4 and NH_3 , whether C_2H_2 will reconvert into CH_4 , and whether H will reconvert into H_2 at high altitudes on the nightside of HD 189733b and HD 209458b, and whether vertical transport-induced quenching will lead to different CH_4 , NH_3 , and HCN mole fractions on the dayside as compared with the terminators (as predicted by our models) or whether horizontal transport-induced quenching will homogenize the quenched mole fractions in the stratosphere.

In general, the horizontal advection timescale over a planetary radius is comparable to or less than the vertical advection timescale over a scale height, suggesting that if temperatures are low enough in the upper troposphere and lower stratosphere to shut down $\text{CH}_4 \leftrightarrow \text{CO}$, $\text{NH}_3 \leftrightarrow \text{N}_2$, and $\text{CH}_4 \leftrightarrow \text{NH}_3 \leftrightarrow \text{HCN}$ interconversion, then horizontal quenching will also be in operation in these regions. As such, zonal winds would be expected to operate efficiently enough to homogenize the CO, CH_4 , H_2O , N_2 , and NH_3 abundances in longitude, and there should be no terminator-versus-dayside differences in the mole fractions of these species in regions where those interconversion reactions dominate. However, in the middle and upper stratosphere, the disequilibrium that results from the absorption of UV photons has a different set of quench reactions operating under much different conditions. Photochemically produced species tend to have shorter lifetimes, and vertical transport timescales are also expected to be shorter at high altitudes. Zonal winds may also increase with altitude in low-latitude regions (Showman et al. 2009), but horizontal transport timescales eventually become longer than the photochemical time constants. Therefore, longitudinal differences are more likely to be maintained at higher altitudes (i.e., pressures less than ~ 0.01 – 0.001 mbar, depending on the species and model).

In our nominal dayside HD 189733b atmosphere for instance (see Figure 5), the HCN that replaces CH_4 and NH_3 at pressures less than a few mbar is produced through scheme (14). This scheme does not operate effectively at pressures greater than a few mbar, and vertical transport dominates the behavior of the HCN profile at these pressures such that the HCN that was produced at higher altitudes diffuses with a constant flux to the lower atmosphere; however, the HCN photochemical lifetime is only ~ 2 hr at 10^{-2} mbar and less than 3 minutes at 10^{-3} mbar, compared to a zonal transport timescale that is likely greater than 20 hr at these pressures (Showman et al. 2009). The photochemical lifetime of C_2H_2 is even shorter, suggesting that longitudinal variations in HCN, CH_4 , NH_3 , and C_2H_2 could be maintained at high altitudes on HD 189733b, such that CH_4 and NH_3 could recover at high altitudes at night. The total column abundances of CH_4 and NH_3 would then be larger on the nightside than on the dayside, particularly at pressures less than ~ 1 mbar.

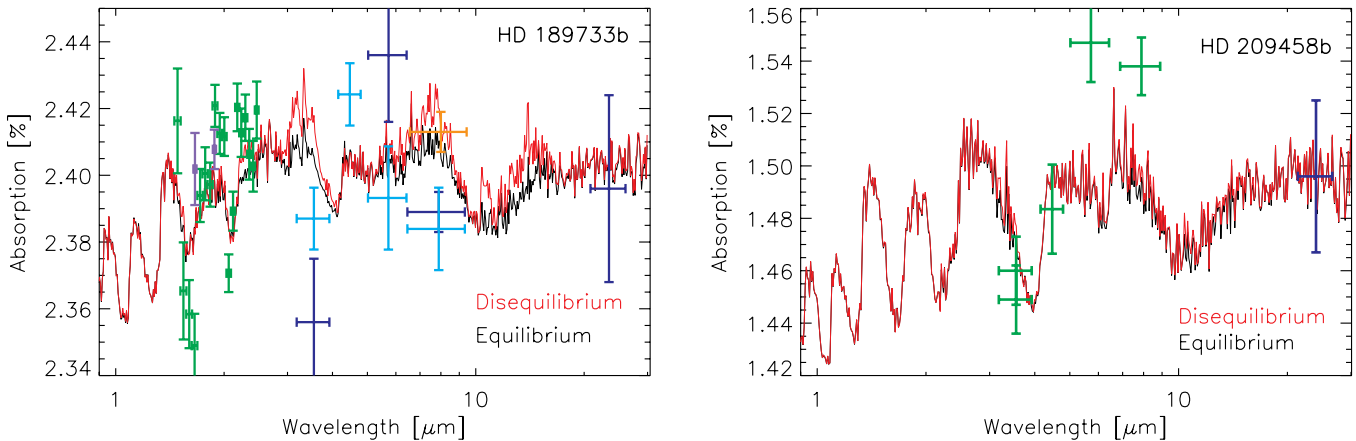


Figure 9. Synthetic transit spectra calculated for our HD 189733b (left) and HD 209458b (right) thermochemical and photochemical kinetics and transport models (red curves) that assume a terminator-average thermal structure and nominal K_{zz} profile, compared with synthetic transit spectra from the thermochemical-equilibrium models (black curves) for the same assumed thermal structure. All models assume a $1\times$ solar composition. Absorption depth is calculated as the square of apparent planet-to-star radius ratio. Observations for HD 189733b are shown as data points with associated error bars: green, Swain et al. (2008b) *HST*/NICMOS; purple, Sing et al. (2009) *HST*/NICMOS; light blue, Désert et al. (2009) *Spitzer*/IRAC; darker blue, Beaulieu et al. (2008) for *Spitzer*/IRAC 3.6 μm and 5.8 μm , Knutson et al. (2007) for *Spitzer*/IRAC 8 μm , and Knutson et al. (2009) for *Spitzer*/IRAC 24 μm ; and orange, Agol et al. (2010) *Spitzer*/IRAC 8 μm . For HD 209458b, the green data points represent the *Spitzer*/IRAC data of Beaulieu et al. (2010) and the blue data point at 24 μm represents the average of the *Spitzer*/MIPS values from Richardson et al. (2006) and H. Knutson (2009, private communication).

(A color version of this figure is available in the online journal.)

It is interesting to speculate what might happen on HD 189733b when the high-altitude CH_4 that comes back at night is transported by the zonal winds to the western (dawn) terminator (assuming atmospheric super-rotation, as is expected from the dynamical models). As the gas flows into the starlight again, the high-altitude CH_4 will strongly absorb in the ultra-violet and at certain visible and near-IR wavelengths where the methane bands have some optically thick lines. Does this expected “pulse” of high-altitude absorption on the dawn limb affect the high-altitude thermal structure or the CH_4 fluorescent emission behavior enough to cause emission in these optically thick lines? If the heating rates are greater than the chemical destruction rates, if there is sufficient methane at high altitudes, and if there is a lag in the cooling rates, then such a scenario might help explain the apparent 3.25 μm emission seen in the Swain et al. (2010) ground-based observations of HD 189733b. We note that if this process were really operating, the emission in the ν_3 methane band should be more obvious in the transit of the dawn terminator than the dusk terminator because more methane will be present at high altitudes on the dawn terminator (again, assuming atmospheric super-rotation). Even if cooling rates were rapid, the sudden pulse of photons at high altitudes would provide energy needed to drive the chemical reactions or fluorescence and might excite any molecules present.

This process would work on HD 209458b as well, but it would be less apparent due to the overall smaller quenched abundance of CH_4 and the correspondingly smaller column abundance of CH_4 at high altitudes. On planets like GJ 436b that are in the CH_4 stability regime at the deep $\text{CO} \leftrightarrow \text{CH}_4$ quench point, the effect could be particularly important. Because CH_4 is likely relatively abundant at high altitudes on both terminators on GJ 436b, we suggest that high-spectral-resolution modeling of radiative absorption and emission on GJ 436b might be called for to determine whether portions of the ν_3 band would be expected in emission rather than absorption on this planet (due to a high-altitude thermal inversion from UV, visible, and near-IR absorption from CH_4), potentially explaining the apparent lack of CH_4 absorption at 3.6 μm in eclipse observations of this planet (Stevenson et al. 2010). These

ideas are quite speculative at this point but deserve further quantitative study. The possibility of dawn-dusk differences in the transit spectra could potentially be explored with the *James Webb Space Telescope* (JWST; see Fortney et al. 2010).

4. IMPLICATIONS WITH RESPECT TO OBSERVATIONS

Figure 9 illustrates how the predicted HD 189733b and HD 209458b spectra from the primary transits are altered by the presence of the disequilibrium products derived in our models. Different radiative-transfer models in the literature are producing different predicted transmission spectra for exoplanets, for reasons that are unclear (cf. Shabram et al. 2011; Beaulieu et al. 2011). For Figure 9, the synthetic transmission spectra are calculated as is described in Fortney et al. (2010) and Shabram et al. (2011) for the terminator-average temperature profiles shown in Figure 2. The calculations assume either a thermochemical-equilibrium composition or use the results from our thermochemical and photochemical kinetics and transport models with the nominal K_{zz} profiles. The approximate pressure levels from which the spectral features originate are discussed further in Fortney et al. (2008a). For HD 189733b, Figure 9 shows clear excess absorption from the disequilibrium model at wavelengths near $\sim 2.1\text{--}2.5\ \mu\text{m}$ and $\sim 2.9\text{--}4\ \mu\text{m}$ due to CH_4 and to a lesser extent due to HCN near 3 μm , additional absorption in the $\sim 7\text{--}9\ \mu\text{m}$ region due largely to CH_4 (with HCN contributing near 7 μm), and additional absorption in the $\sim 9\text{--}15\ \mu\text{m}$ region due to NH_3 (centered near 10.5 μm) and HCN (centered near 14 μm), with a much lesser contribution from C_2H_2 (centered near 13.6 μm). Note that the column abundance of C_2H_2 in our nominal model is small enough that acetylene absorption features are not very prominent. For HD 209458b, spectral differences between the equilibrium and disequilibrium models are much more muted, as the overall compositional changes are slight between the equilibrium and disequilibrium models at the pressure levels at which the observations are sensitive. Our modeling suggests that photochemistry and transport-induced quenching will have only a minor effect on the spectral properties of the hottest “hot Jupiters” or those with strong

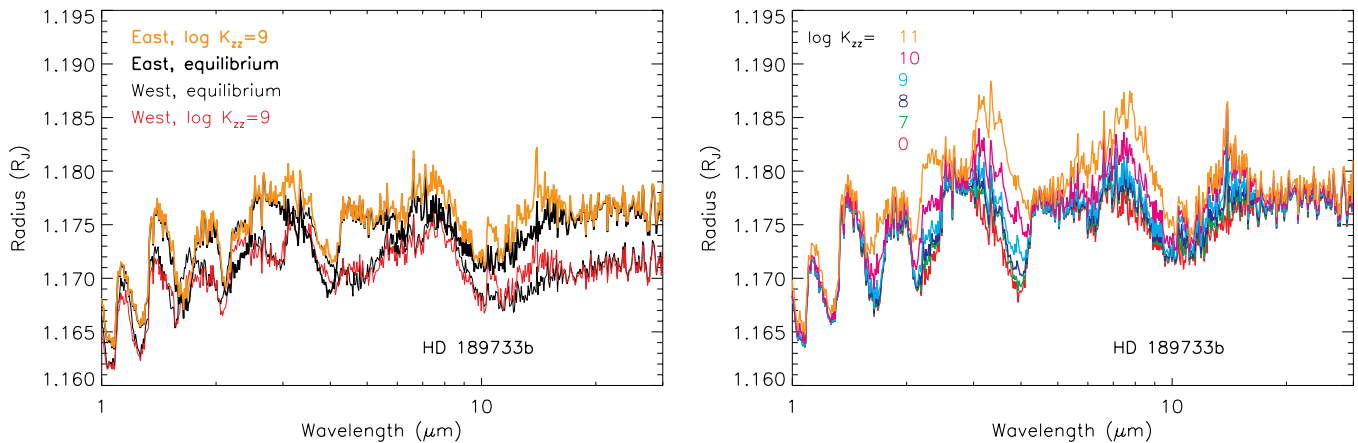


Figure 10. Synthetic transit spectra (apparent planetary radius in units of Jupiter radii) calculated for HD 189733b for different assumptions about the thermal structure (left) and the eddy diffusion coefficient profile (right). In the left panel, the gray curve represents a model with the west-terminator-average temperature profile and an equilibrium composition, the red curve represents a model with the west-terminator-average temperature profile and a composition indicated by our disequilibrium model with $K_{zz} = 10^9 \text{ cm}^2 \text{ s}^{-1}$, the black curve represents a model with the east-terminator-average temperature profile and an equilibrium composition, and the orange curve represents a model with the east-terminator-average temperature profile and a composition indicated by our disequilibrium model with $K_{zz} = 10^9 \text{ cm}^2 \text{ s}^{-1}$. In the right panel, the models assume a dayside-average thermal structure: the red curve is the equilibrium model, and the other curves represent disequilibrium models with assumed constant K_{zz} values of 10^7 (green), 10^8 (dark blue), 10^9 (cyan), 10^{10} (magenta), and 10^{11} (orange) $\text{cm}^2 \text{ s}^{-1}$.

(A color version of this figure is available in the online journal.)

stratospheric thermal inversions, as the high temperatures enable rapid kinetics that can drive the atmosphere back toward equilibrium.

For HD 189733b, however, the disequilibrium chemistry resulting from photochemistry and transport-induced quenching measurably alters the composition such that the disequilibrium model shows additional absorption and a greater wavelength-dependent contrast overall than the equilibrium model. Although the near-infrared absorption band positions predicted by the model are generally consistent with observations, both the equilibrium and disequilibrium models apparently underestimate the near-IR band depths and the overall amplitude of the wavelength-dependent variations—a fact previously discussed for equilibrium models by Fortney et al. (2010). Even when disequilibrium constituents are considered, the model fit to the near-IR *HST*/NICMOS data of Swain et al. (2008b) and Sing et al. (2009) is not significantly improved, as water absorption and H_2 collision-induced absorption dominate the spectral behavior at near-IR wavelengths, and these opacity sources remain roughly the same in the two models. The main exceptions to this statement are wavelength regions centered near $2.3 \mu\text{m}$ and $3.3 \mu\text{m}$, where methane absorption can have a significant effect. The additional methane in the disequilibrium models for HD 189733b improves the fit in the $2.3 \mu\text{m}$ region (see also Swain et al. 2008b; Madhusudhan & Seager 2009) but degrades the fit to the Infrared Array Camera (IRAC) $3.6 \mu\text{m}$ data (e.g., Beaulieu et al. 2008; Désert et al. 2009). At mid-IR wavelengths, the models also appear to underestimate the spectral contrast between different wavelengths, and neither model does a good job of reproducing the *Spitzer*/IRAC photometric data, although the data have large error bars, and different groups using different analysis procedures for the same data sets do not always agree on the observed flux in the IRAC bands. As was discussed by Fortney et al. (2010), higher-metallicity models with their increased CO and CO_2 abundances would improve the fit to the relative absorption strengths of the 3.6 , 4.5 , and $5.8 \mu\text{m}$ IRAC band data points from the Désert et al. (2009) analysis, but other model-data comparison problems would still remain. Note that we have not recalculated the thermal profile that will result from the additional disequilibrium opacity sources, and the ex-

pected altered thermal structure may also affect the observed spectrum.

As an example of the sensitivity of transmission spectra to the thermal profile, Figure 10 shows how the synthetic spectra for HD 189733b change for different assumptions about the thermal structure at the terminators—particularly the western versus eastern terminator-average profiles from Figure 2; Figure 10 also shows the sensitivity of the transmission spectra to different assumptions about the eddy diffusion coefficient profile, for assumed constant K_{zz} profiles ranging from 10^7 to $10^{11} \text{ cm}^2 \text{ s}^{-1}$. The thermal structure affects such things as the atmospheric scale height, which describes how extended the atmosphere becomes, so that a colder planet will have less of an apparent cross section during transit for all other factors being equal. As such, the colder western-terminator model exhibits a smaller apparent radius than the eastern-terminator model. Note that the spectral changes caused by the equilibrium versus disequilibrium models have less of an overall impact on the apparent absorption during transit than assumptions about the thermal structure. The eddy diffusion coefficient profile affects the extent to which heavy molecular constituents can be mixed to high altitudes on an H_2 -dominated planet; in general, the larger the eddy diffusion coefficient, the higher the altitude to which the molecular constituents can be carried, which allows photochemical species to be produced over a larger column of the atmosphere, leading to larger column abundances and increased absorption by the photochemical products. Eddy diffusion coefficients also affect the abundances of the species controlled by transport-induced quenching, as is discussed in Sections 3.2 and 3.7.

Synthetic emission spectra of HD 189733b and HD 209458b for dayside-average, secondary-eclipse conditions are shown in Figure 11. For these calculations, local thermodynamic equilibrium conditions are assumed, and the effects of the important spectrally active gases H_2O , CO, CH_4 , CO_2 , HCN, NH_3 , C_2H_2 , and C_2H_6 are considered. The opacities of these gases are garnered from different sources. The hot water line parameters from the latest 2010 November version of the HITRAN line list (Rothman et al. 2009) are adopted, using the original data of Barber et al. (2006) and Zobov et al.

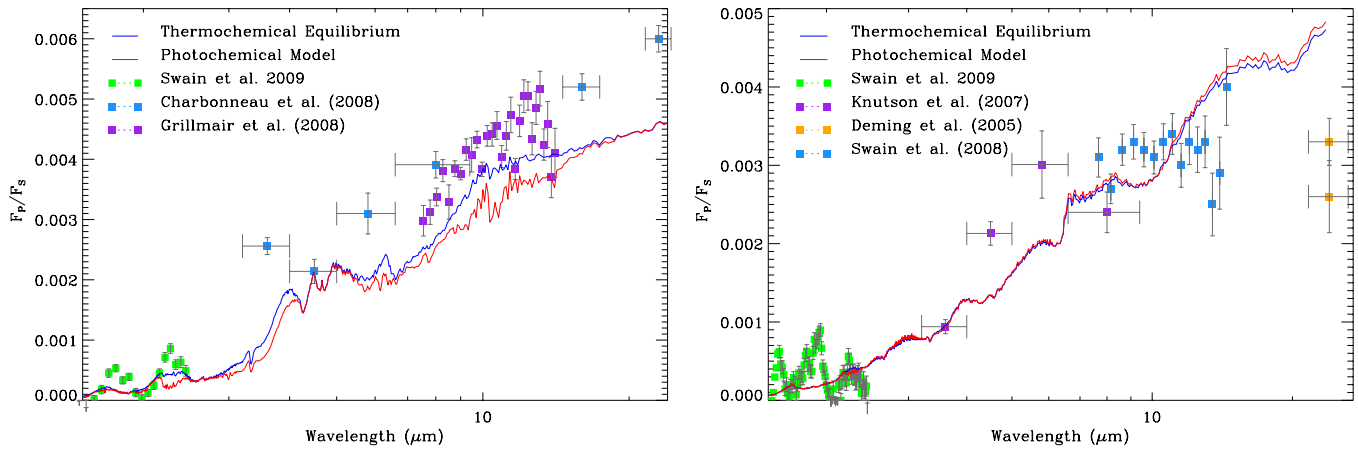


Figure 11. Synthetic emission spectra for HD 189733b (left) and HD 209458b (right) for our thermochemical and photochemical kinetics and transport models (red curves) that assume a dayside-average thermal structure and corresponding nominal K_{zz} profile for the planet in question (see Figures 1 and 2), compared with synthetic spectra from the thermochemical-equilibrium model (blue curves) for the same assumed thermal structure. All models assume a $1\times$ solar elemental composition. Spectra are calculated as the ratio of the flux of the planet to the flux of the star. Also shown are data points from various secondary-eclipse observations, as labeled. (A color version of this figure is available in the online journal.)

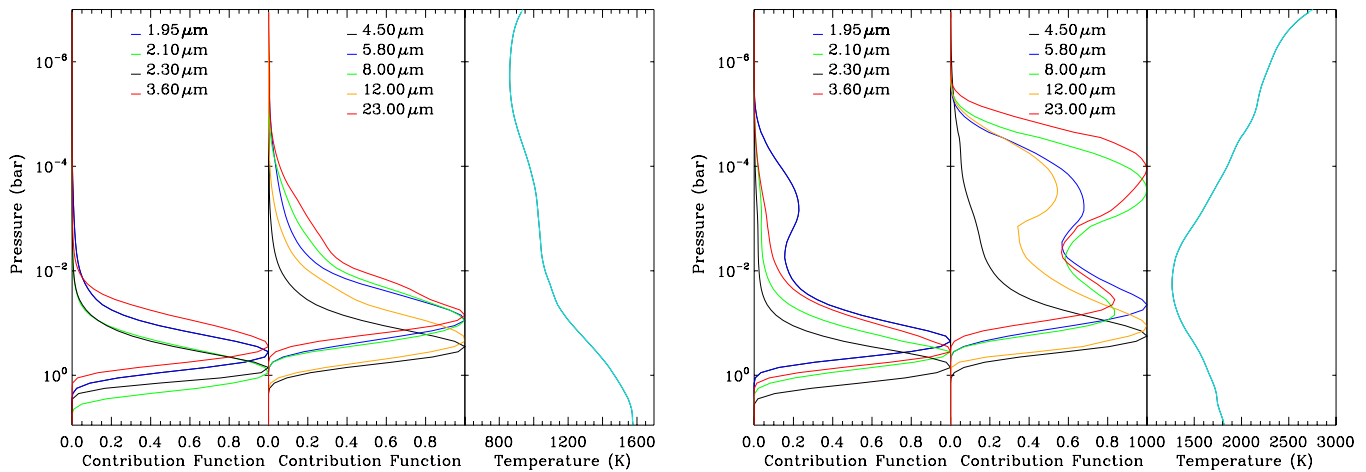


Figure 12. Contribution functions, which give the relative contribution of a given pressure level to the observed emission at any particular wavelength, are shown alongside the thermal structure from our dayside-average chemical models for HD 189733b (left) and HD 209458b (right).

(A color version of this figure is available in the online journal.)

(2008). Absorption by CO_2 is calculated from the HITRAN hot CO_2 line list (Tashkun et al. 2003), as is that of CO and NH_3 (Rothman et al. 2009), and the methane line parameters derived from the hot CH_4 line parameters of Freedman et al. (2008). Note that for both the transmission and emission modeling, the opacities of HCN and C_2H_2 —and really all species other than H_2O , CO_2 , and CO —are likely underestimated because the line parameters were derived from cool, low-temperature conditions. Absorption coefficients are calculated using a line-by-line technique every 0.004 cm^{-1} wavenumber to provide the k -coefficients that are included in the radiative-transfer calculations. For the calculations of the emission spectra, the atmosphere is divided into 80 vertical grid points that extend from 10^{-7} to 10 bar. The effects of particulates are excluded. The calculations explore the spectroscopic effects of the compositions that are indicated by the different chemical models, while the temperature structure is held fixed. The depths at which the various emission signatures originate can be seen from the contribution functions shown in Figure 12.

The synthetic emission spectra shown in Figure 11 illustrate that spectral signatures from the disequilibrium model are noticeably altered from the equilibrium predictions for the cooler

HD 189733b but not for the warmer HD 209458b. The predicted eclipse depths are only slightly modified at long wavelengths due to the disequilibrium chemistry on HD 209458b. That conclusion changes for HD 189733b, as the key disequilibrium constituents CH_4 , HCN , and NH_3 are more abundant and have a larger impact on the predicted spectrum. On HD 189733b, the disequilibrium-model spectra diverge from the equilibrium spectra in the 7–9 μm range due to the ν_4 CH_4 band at 7.7 μm , in the $\sim 3\text{--}4\text{ }\mu\text{m}$ and $\sim 2.1\text{--}2.5\text{ }\mu\text{m}$ ranges due to the 3.3 and 2.3 μm bands of CH_4 , in the 5.5–6.6 μm range due to the ν_4 band of NH_3 at 6.15 μm , in the 8–12 μm range due to the ν_2 band of NH_3 at 10.5 μm , and in the 13–15 μm range due to the ν_2 band of HCN at 14 μm . The individual contributions from the different disequilibrium species are better illustrated in Figure 13.

Our emission spectra for both HD 189733b and HD 209458b do not compare well with the observed fluxes during secondary eclipse (e.g., Deming et al. 2005b; Richardson et al. 2007; Knutson et al. 2008; Charbonneau et al. 2008; Grillmair et al. 2008; Swain et al. 2008a, 2009a, 2009b; Madhusudhan & Seager 2009). For HD 209458b, apparent emission features at 4.5 and 5.8 μm (see, e.g., Knutson et al. 2008) are not present

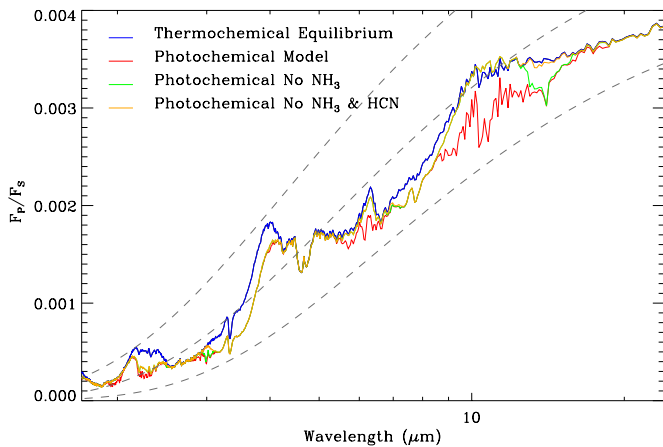
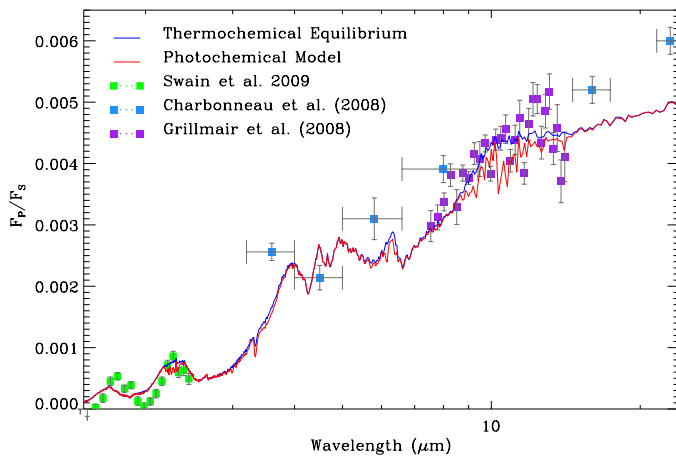


Figure 13. Synthetic emission spectra for HD 189733b, as described in Figure 11, except the green curve shows how the results change when the contribution of NH_3 is removed from the kinetics and transport model spectra, and the orange curve shows how the results change when the contributions of both NH_3 and HCN are removed from the kinetics and transport model spectra. Note that methane opacity is the primary source of the divergence of the orange curve from the blue equilibrium curve. The dashed lines are blackbody curves for particular temperatures: top curve is for 1400 K, middle curve is for 1200 K, and bottom curve is for 1000 K.

(A color version of this figure is available in the online journal.)

in the model spectra, which could be due to an inaccurate temperature profile adopted for our model (e.g., a thermal inversion beginning at higher altitudes in our model than on the real planet), or some other inappropriate assumptions for the spectral or chemical models. For HD 189733b, the model eclipse depths are much smaller than has been observed at all wavelengths, perhaps resulting from inaccurate model assumptions such as the atmospheric thermal structure of the planet, the planet’s metallicity and radius, or the spectrum of the host star (note that we have used the models of Castelli & Kurucz 2004 to simulate the spectrum of the host stars, with other stellar and planetary parameters as described in Torres et al. 2008). In particular, the model-data comparisons shown in Figure 11 suggest that our assumed dayside atmospheric temperatures may be too cold in the 0.01–1 bar region. We therefore also calculate synthetic spectra for the warmer 1D



“2 π ” model of Fortney et al. (2006, 2010; see Figure 2); the results are shown in Figure 14, along with the corresponding contribution functions. Note that the magnitude of the eclipse depths is better predicted and the disequilibrium effects are reduced with this warmer model.

Our emission spectra for both HD 189733b and HD 209458b do not compare well with the observed wavelength-dependent fluxes. Rather than dwelling on possible reasons, we have focused on the expected differences in the spectral signatures of equilibrium and disequilibrium compositions in this section. Detailed comparisons of our predicted mole fractions with inferences from published analyses of transit and eclipse observations are deferred to Sections 6 and 7.

5. COMPARISONS WITH OTHER PHOTOCHEMICAL MODELS

We now compare our results with those from other photochemical models. Liang et al. (2003) were the first to develop a photochemical model for hot-Jupiter exoplanets. Their main conclusion from their HD 209458b modeling was that atomic H is produced in large quantities from photolysis of H_2O and from the subsequent reaction of OH with H_2 (see our scheme (10) in Section 3.3). We agree with this general result, although some quantitative differences exist between our models. For instance, atomic H never replaces H_2 as the dominant constituent at high altitudes in the Liang et al. (2003) models, for reasons that are unclear. Our HD 209458b models are more comparable to the García Muñoz (2007) and Koskinen et al. (2010) models with regard to this H-abundance issue.

Other quantitative differences are apparent between the Liang et al. (2003) models and ours. Because Liang et al. (2003) do not consider thermochemical kinetics and do not fully reverse their reactions, they take a reasonable approach in beginning their model at a base pressure of ~ 1 bar, where equilibrium effects will be less prevalent. Liang et al. (2003) do not consider transport-induced quenching of CH_4 , and their assumed 1 bar methane abundance is quite a bit lower than ours; however, even ignoring this difference, the shape of their methane profiles throughout the atmosphere is quite different from our HD 209458b models. In the Liang et al. (2003) models, the CH_4 abundance increases from 1 bar to 0.1 mbar because of

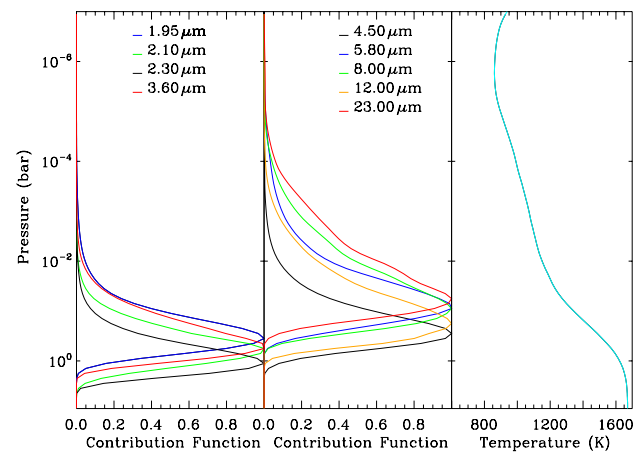


Figure 14. Synthetic emission spectra for HD 189733b (left) for the 1D “2 π ” thermal structure of Fortney et al. (2006, 2010; i.e., the temperature structure is from a 1D radiative-convective equilibrium model where it is assumed that the incident stellar energy is distributed over the dayside hemisphere only), along with the contribution functions for this model (right). The model shown by the red curve uses results from our thermochemical and photochemical kinetics and transport model with the nominal K_{zz} profile, whereas the model shown by the blue curve assumes a thermochemical-equilibrium composition. Both models assume a $1\times$ solar elemental abundance. Also shown are data points from various secondary-eclipse observations, as labeled.

(A color version of this figure is available in the online journal.)

production of CH₄ from CO photolysis, whereas our CH₄ mole-fraction vertical slopes above the quench point are more constant or even negative before methane becomes sharply depleted when schemes (14) and (12) become effective, indicating a net loss rather than net production of methane in the 1–10^{−4} bar region of our models. However, both our models and those of Liang et al. (2003) suggest that CH₄ does not survive at high altitudes on HD 209458b. In our models, CH₄ is destroyed by reaction with atomic H (see schemes (12) and (14), for example) and the carbon ends up in species like HCN and C₂H₂. In contrast, Liang et al. (2003) state that CH₄ photolysis rather than reaction with atomic H causes the high-altitude depletion, but it is not clear from their discussion where the carbon ends up.

Some of these issues are clarified in the follow-up model of Liang et al. (2004), where it seems that hydrocarbons like C₂H₂ may replace CH₄ as the second most abundant carbon-bearing species (behind CO) at high altitudes in their HD 209458b models. The Liang et al. (2004) “Model A” is closest to our HD 209458b west-terminator-average model in terms of the CH₄ abundance at 0.1 mbar, so these two models can be compared in detail. Our model has some similar general behavior, such as the fact that C₂H₂ is the dominant C₂H_x hydrocarbon from a column-integrated standpoint and that C₂H₂ can survive to relatively high altitudes, as compared with C₂H₆. We also agree that hydrogenation is the major loss mechanism for C₂H_x hydrocarbons that prevents complex hydrocarbons from becoming major constituents on HD 209458b. However, there are also some large differences between our models in terms of the overall abundances and vertical profiles of C₂H_x hydrocarbons. For example, our C₂H₂ profiles tend to peak at high altitudes and fall off sharply with both increasing and decreasing altitude, whereas their C₂H₂ profiles are roughly constant above ~0.1 mbar. In our models, three-body reactions with atomic H that act to destroy C₂H₂ become increasingly effective with increasing pressure, and C₂H₂ ends up being more efficiently converted to CH₄ in the 1–10^{−3} mbar region (see scheme (13) in Section 3.4) than is apparently the case in the Liang et al. (2004) models. Also, C₂H₂ cannot survive the large H abundance above 10 nbar in our model, whereas C₂H₂ readily survives at those pressures in the Liang et al. (2004) model, suggesting that H is much less abundant or that C₂H₂ conversion into atomic C is much less effective in this region of the Liang et al. (2004) models. In general, C₂H_x hydrocarbons are much less abundant in the 1–10^{−6} bar region of our HD 209458b models, suggesting that our kinetics more efficiently converts these species to CH₄ than in the Liang et al. (2004) models (see scheme (13) in Section 3.4).

The Liang et al. (2003, 2004) models were updated significantly by Line et al. (2010), who consider methane quenching for the first time and expand the range of high-temperature reactions in their kinetics. Line et al. (2010) use the timescale arguments developed by Prinn & Barshay (1977; see Section 3.2) to estimate the quenched CH₄ mole fraction on HD 189733b. Their resulting quenched mole fraction for CH₄— 4×10^{-5} —is reasonably consistent with the results of our kinetics/transport model (see Figure 5), but their reasoning in deriving this value is marred by the fact that they incorrectly reverse their assumed rate-limiting CO → CH₄ conversion step (see Bézard et al. 2002; Visscher et al. 2010b; Visscher & Moses 2011 for information on correct reversal procedures for this assumed rate-limiting reaction) and by the fact that the reversal was not necessary in the first place since it is CH₄ → CO quenching that matters for HD 189733b. Given these issues and the fact that Line et al.

(2010) have a different rate-limiting step for CH₄ quenching than we have derived in our model, as well as the fact that they do not use the Smith (1998) procedure when calculating the transport timescale, it is remarkable that their quenched mole fraction for CH₄ is so close to that in our models.

In any case, the procedure used by Line et al. (2010) once the CH₄ quench point has been established is perfectly valid—it may even be preferable to full thermochemical and photochemical kinetics and transport models in some instances. As an example, the quench kinetics for CH₄ has some uncertainty associated with it due to uncertainties in the kinetic rate coefficients, the eddy diffusion coefficients, and the atmospheric thermal structure. If the CH₄ abundance for a transiting exoplanet were unambiguously determined from transit or eclipse observations, it might be better to take this information into account and begin photochemical calculations at some point above the quench level (i.e., put the base of the model just above the CH₄ quench level, as in the Line et al. 2010 models). This procedure would work best for C–H–O chemistry investigations, as nitrogen-bearing and sulfur-bearing constituents have yet to be detected in hot-Jupiter atmospheres.

The quenched CH₄ mole fraction in the Line et al. (2010) daytime model is most similar to our terminator-average HD 189733b model (see Figures 4 and 5), and the two can be directly compared. In contrast to equilibrium predictions, both of our models show a greatly enhanced H abundance in the middle and upper stratosphere due to scheme (10), both show CH₄ depletions at high altitudes with corresponding significant C₂H₂ enhancements at these altitudes, both show small enhancements in the CO₂ mole fraction at high altitudes due to CO and H₂O photochemistry, and both show that photochemical processes have little net effect on the H₂O and CO profiles. However, there are also some significant differences between our models that are worth mentioning. As with the Liang et al. (2003, 2004) photochemical models, the H production rate in the Line et al. (2010) models is large, but H never exceeds the H₂ abundance at pressures $\lesssim 1$ nbar, as it does in our HD 189733b models. Again, the reason for this difference between our models is unclear, but it seems to have something to do with the efficiency of scheme (10) and its reverse or with other H₂ destruction and recycling mechanisms. The fact that we have considerably more O and OH at high altitudes in our model as compared with Line et al. (2010) is consistent with our greater depletion of H₂ and is consistent with this suggested cause. Our models also show less net production of CO₂ from photochemical processes than in the Line et al. (2010) model, as thermochemical processes in our model drive the CO₂ abundance back toward equilibrium.

Another difference between our model and that of Line et al. (2010) is the more abrupt and more severe depletion in the CH₄ mole fraction above $\sim 1 \mu\text{bar}$ in our HD 189733b model as compared with their model. This difference is likely due to coupled carbon–nitrogen chemistry (see scheme (14), for example), as HCN takes over from CH₄ at high altitudes in our model, whereas nitrogen chemistry is not considered in the Line et al. (2010) models. A more minor difference between our model and theirs is the dominant scheme to form C₂H_x hydrocarbons in the stratosphere. In Line et al. (2010) and in the Liang et al. (2003, 2004) models on which these models were based, the dominant reaction that produces C₂ species from CH_x species is apparently $^3\text{CH}_2 + ^3\text{CH}_2 \rightarrow \text{C}_2\text{H}_2 + 2\text{H}$, whereas we find the reaction $^3\text{CH}_2 + \text{CH}_3 \rightarrow \text{C}_2\text{H}_4 + \text{H}$ to be more important from a column-integrated standpoint. Qualitatively, however, the main behavior in the Line et al. (2010) models is similar to

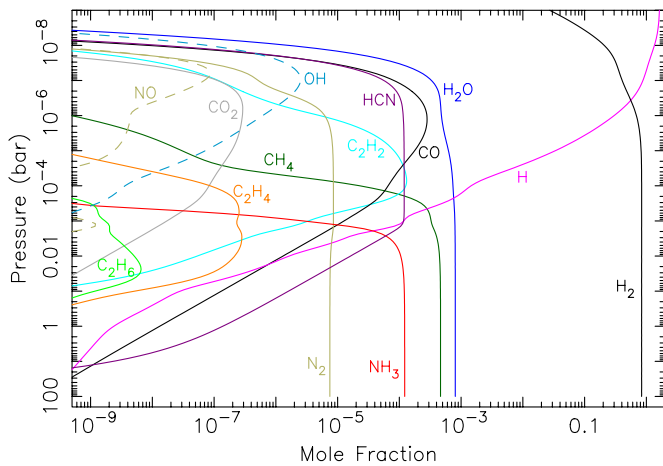


Figure 15. Mole-fraction profiles for major species in a $1\times$ solar composition model that assumes temperatures are constant at 1000 K, K_{zz} 's are constant at $10^9 \text{ cm}^2 \text{ s}^{-1}$, and the planet is located at 0.1 AU from a Sun-like star, for a stellar zenith angle fixed at 30° . These model results can be compared with isothermal models described in Zahnle et al. (2011), as well as with our HD 189733b and HD 209458b models results shown in Figures 4–6.

(A color version of this figure is available in the online journal.)

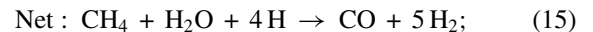
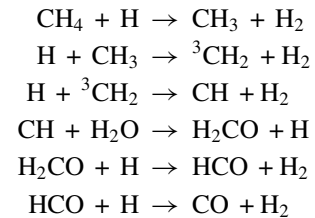
ours, other than some differences that result from our inclusion of nitrogen photochemistry.

We can also compare our models to the thermochemical and photochemical kinetics and transport models of Zahnle et al. (2011). Note that Zahnle et al. (2009) discuss sulfur photochemistry only, which we do not consider, so we do not compare our results with Zahnle et al. (2009). Direct comparisons between our models and those of Zahnle et al. (2011) are complicated by the fact that they show results only for models with isothermal atmospheres. Comparisons are also hampered by the fact that Zahnle et al. (2011) are working on a revision of their model as we are preparing this present paper, so that we can only compare with their “version 2” in the arXiv archive, rather than with a published version of the models. Although we cannot do anything about the second problem, we can resolve the first problem—which is a significant one—by developing an isothermal model of our own to better compare with the Zahnle et al. (2011) results. The isothermal model that we develop is for a $1\times$ solar-composition atmosphere, with $T = 1000 \text{ K}$, and K_{zz} at a constant $10^9 \text{ cm}^2 \text{ s}^{-1}$, for a planet located 0.1 AU from a Sun-like star, at a fixed solar zenith angle of 30° (see Figure 15). This model can be directly compared with the results shown in the top right figure of Figure 4 of the arXiv version 2 of Zahnle et al. (2011). Since Zahnle et al.’s 100 bar lower boundary condition of a 1×10^{-12} mole fraction for species other than H , H_2O , CO , CH_4 , NH_3 , N_2 , and H_2S in the Zahnle et al. (2011) model leads to odd behavior for some of the minor constituents near the lower boundary, we simply assumed a constant concentration gradient for minor species (including H and CO , which are minor species under these conditions at the 100 bar lower boundary), which means that these species will flow through the lower boundary at a maximum possible rate. We also assumed equilibrium mole fractions for H_2 and He at the lower boundary.

A detailed comparison of Figure 15 with Figure 4(b) of Zahnle et al. (2011) reveals some similarities and differences between our models. The H_2O mole fraction remains just below 10^{-3} in both models and is fairly unperturbed by photochemistry. Atomic H is very abundant at high altitudes and greatly affects

the chemistry of molecular species in both models. Although our results for atomic H are qualitatively similar here, the quantitative results differ, likely because of differences in chemical reaction rate coefficients for hydrocarbon reactions. Methane has a sharp mole-fraction cutoff in both models at pressures of 10^{-3} or 10^{-4} bar, although the location of the cutoff and shape of the CH_4 profile are different in both models. This difference appears to be related to C_2H_4 chemistry, as the ethylene profiles are the most obvious difference between the models. The Zahnle et al. (2011) results have C_2H_4 replacing CH_4 at a relatively deep ~ 0.1 bar, causing a large “bite out” in the CH_4 profile from 0.1 to 0.001 bar before C_2H_2 takes over as the dominant hydrocarbon at high altitudes. The C_2H_4 in our model peaks at a somewhat higher altitude, and its abundance never approaches that of CH_4 , so methane is carried up to pressures of 10^{-4} mbar before its eventual replacement by C_2H_2 , HCN , and CO —note that both models agree that CO , HCN , and C_2H_2 will be the dominant carbon carriers at high altitudes. The differences in the hydrocarbon profiles and some portion of the H profiles seem to stem from a different low-pressure limiting rate coefficient for $\text{H} + \text{C}_2\text{H}_4 + \text{M} \rightarrow \text{C}_2\text{H}_5 + \text{M}$ between our models. Due to an inadvertent data-entry error, that rate coefficient in the Zahnle et al. (2011) model is three orders of magnitude smaller than the expression we have adopted, effectively cutting off an important C_2H_4 destruction pathway. When this expression is changed to better reflect literature values (e.g., Baulch et al. 1994), the Zahnle et al. (2011) results are more in line with ours (K. Zahnle 2010, private communication).

Another apparent difference between the Zahnle et al. (2011) models and ours is the CO and CO_2 mole fractions at lower altitudes. Although the CO mole fraction remains at 10^{-3} to 10^{-4} at high altitudes in both models, the drop off with decreasing altitude has a much different gradient in our model compared with theirs. Carbon monoxide is produced photochemically at high altitudes in both models, and CO then flows down to the lower atmosphere where in our model the large flux boundary condition allows it to be transported out of the system. Zahnle et al. (2011) do not discuss their dominant methane oxidation pathways in detail, so it is not clear how methane is converted to CO in their model, although they do mention that $\text{C} + \text{OH}$ is important and they mention that they include three-body OH addition reactions that can form $\text{C}-\text{O}$ bonds. In our model, methane is oxidized to CO through processes such as



however, this mechanism becomes ineffective once the H abundance drops significantly, and mechanisms like schemes (2) and (3) in Section 3.2 take over but do not operate effectively at 1000 K. Therefore, in our model, diffusion controls the CO profile at low altitudes. If the Zahnle et al. (2011) model is fully converged, then it appears that either the above CO production scheme (15) or alternative ones that produce the $\text{C}-\text{O}$ bond remain effective at low altitudes in the Zahnle et al. (2011) model—perhaps due to their much larger low-altitude H abundance—allowing CO to be kinetically produced

in the lower atmosphere. Whatever the cause, their increased CO abundance in the lower atmosphere allows an increased abundance of CO₂ compared to our model, as CO and CO₂ are kinetically linked.

The qualitative results for the nitrogen-bearing species appear to be similar between our model and that of Zahnle et al. (2011). Ammonia has a sharp cutoff at $\sim 10^{-3}$ bar in both models, with HCN replacing NH₃ as the dominant nitrogen carrier at higher altitudes. Molecular N₂ is relatively unreactive in both models and has a constant mole fraction throughout most of the atmosphere. The Zahnle et al. (2011) model apparently has an effective mechanism that converts HCN to N₂ at high altitudes, whereas HCN is more efficiently recycled at high altitudes in our model. Similarly, NO is produced at high altitudes more efficiently in the Zahnle et al. (2011) model, or we have more efficient loss processes in our model.

In general, our main conclusions from this isothermal modeling exercise are similar to those of Zahnle et al. (2011) in terms of the major carbon-, oxygen-, and nitrogen-bearing species and their relative importance in different regions of the atmosphere, with the exception of the C₂H₄ abundance, as discussed above. However, we disagree with the assertion of Zahnle et al. (2011) that such isothermal atmospheres are good analogs for extrasolar planets, and we feel the likelihood of soot formation on cooler exoplanets has been overemphasized as a result of Zahnle et al.'s reliance on isothermal models. Isothermal model results do have some resemblance to those from models with more realistic temperature profiles (compare Figures 4–6 with Figure 15). However, one critical difference is the presence of transport-induced quenching in the models with more realistic temperature profiles. Like the real HD 189733b atmosphere, the isothermal 1000 K profile starts in the CH₄ stability regime in the deep atmosphere but crosses over to the CO stability field in the upper atmosphere. However, unlike the real HD 189733b atmosphere, temperatures are low enough throughout the 1000 K isothermal atmosphere that interconversion between CO and CH₄ (and between N₂ and NH₃, etc.) is inhibited everywhere. Therefore, whatever molecule is dominant at the base of the isothermal model will continue to be the dominant molecule throughout most of the atmosphere in the isothermal photochemical models. Transport-induced quenching will not occur, and thus the abundance of species like CO will be underpredicted (as its only source will be photochemistry, not thermochemistry), and the CH₄ abundance will be overpredicted as compared to kinetic-transport models that have higher temperatures at depth.

This problem is particularly acute if the real planet has a temperature profile such that the composition would remain in thermochemical equilibrium as the atmosphere transitions into the CO stability field, as seems to be the case for both HD 189733b and HD 209458b. In that case, the CH₄ → CO interconversion quench point will occur while CO is dominant, and CO will be the main carrier of carbon in the stratospheres of these planets, in stark contrast to the isothermal model results. Even if the stratospheres become quite cold on these planets with more realistic temperature profiles, methane is not going to be as abundant as the isothermal models would indicate. Because CH₄ is the source of the complex hydrocarbons in the Zahnle et al. (2011) models (and in our own models), a greater CO/CH₄ ratio in the upper atmosphere implies fewer hydrocarbons and less chance of soot formation. The inability to form complex hydrocarbons is also exacerbated by the efficient hydrogenation of unsaturated hydrocarbons as the pressure increases, so that species like C₂H₂ and C₂H₄ are efficiently

converted back to methane at pressures greater than 1 μ bar in our model (and probably would be in the Zahnle et al. (2011) model for more realistic considerations of the low-pressure limiting rate coefficient for $\text{H} + \text{C}_2\text{H}_4 + \text{M} \rightarrow \text{C}_2\text{H}_6 + \text{M}$). Complex hydrocarbons are thus several orders of magnitude less important in our HD 189733b models than the isothermal (Zahnle et al. 2011) models would suggest, and soot formation is much less of a factor. That is not to say that soot formation cannot still occur on these cooler exoplanets, as is discussed in Section 3.4, particularly if ion chemistry is conducive to the formation of heavy neutrals, but the soot precursors would be confined to high altitudes, and the overall column abundance of heavy hydrocarbons will be many orders of magnitude smaller than is suggested by the Zahnle et al. isothermal models.

6. COMPARISONS WITH OBSERVED MOLE FRACTIONS ON HD 189733b

Our model results can also be compared with the mole fractions inferred from the transit and eclipse observations of HD 189733b (see Table 2). The suggestion that C-, O-, or N-bearing molecules are affecting the observational signature of HD 189733b during the primary transit and secondary eclipse came originally from mid-infrared photometry from the IRAC and from mid-infrared spectra from the Infrared Spectrograph (IRS) on the *Spitzer Space Telescope* (Tinetti et al. 2007; Grillmair et al. 2008; Beaulieu et al. 2008; Knutson et al. 2007, 2008; Charbonneau et al. 2008; Désert et al. 2009; see also the theoretical modeling and model-data comparisons of Fortney & Marley 2007; Barman 2008; Burrows et al. 2008; Madhusudhan & Seager 2009). The mid-IR data have provided relatively loose constraints on molecular abundances for HD 189733b (see Table 2), whereas the near-infrared wavelength region is potentially more useful for constraining abundances because of the presence of potentially diagnostic absorption features in this region. In fact, near-IR transit and eclipse data from the NICMOS instrument on the *HST* do seem to provide tighter constraints on molecular abundances (Swain et al. 2008b, 2009a; Sing et al. 2009; Madhusudhan & Seager 2009). However, the state of affairs in the analysis of transit and eclipse observations is clearly not ideal, as contradictory data sets and/or analyses exist, both within the mid-IR and near-IR regions and between these two regions (e.g., Madhusudhan & Seager 2009; Désert et al. 2009; Beaulieu et al. 2008; Sing et al. 2009; Swain et al. 2008b; Gibson et al. 2011; Fortney et al. 2010). If systematic instrument effects are not completely inhibiting the ability to acquire meaningful spectral and photometric information (e.g., Gibson et al. 2011), we can at least attempt to compare our model results with the available observations (see Table 2) and discuss some general issues.

Our 1 \times -solar-composition kinetics-transport models for HD 189733b appear consistent with the loose constraints supplied by the *Spitzer* IRS secondary-eclipse observations of H₂O and CH₄ (Grillmair et al. 2008; Madhusudhan & Seager 2009), with the tighter constraints from *HST* NICMOS secondary-eclipse observations of CO and CO₂ as reported by Swain et al. (2009a), and with the CH₄ and H₂O abundances from the *HST* NICMOS transit observations analyzed by Madhusudhan & Seager (2009) and Swain et al. (2008b). The models cannot, however, account for the much smaller CH₄ mixing ratios inferred for the secondary eclipse as opposed to the primary transit of HD 189733b (cf. Swain et al. 2008b, 2009a; Madhusudhan & Seager 2009), unless large temperature differences between the dayside and terminators can be maintained in the 1–100 bar

Table 2
Volume Mixing Ratios from HD 189733b Observations and Models

Source	H ₂ O	CO	CH ₄	CO ₂
Secondary eclipse: <i>Spitzer</i> IRS				
Grillmair et al. (2008)	1 × solar
Madhusudhan & Seager (2009)	10 ⁻⁶ to 0.1	...	<10 ⁻²	...
Secondary eclipse: <i>Spitzer</i> IRAC				
Charbonneau et al. (2008)	1 × solar	1 × solar
Madhusudhan & Seager (2009)	(0.1–1) × 10 ⁻⁴	...	≤2 × 10 ⁻⁶	(7–700) × 10 ⁻⁷
Secondary eclipse: <i>HST</i> NICMOS				
Swain et al. (2009a)	(0.1–1) × 10 ⁻⁴	(1–3) × 10 ⁻⁴	≤1 × 10 ⁻⁷	(1–10) × 10 ⁻⁷
Madhusudhan & Seager (2009)	~1 × 10 ⁻⁴	(0.2–20) × 10 ⁻³	≤6 × 10 ⁻⁶	~7 × 10 ⁻⁴
Our dayside-average thermal-structure models at 0.1 bar (i.e., for secondary-eclipse conditions)				
Nominal K_{zz}	3.5 × 10 ⁻⁴	4.5 × 10 ⁻⁴	1.2 × 10 ⁻⁵	1.3 × 10 ⁻⁷
$K_{zz} = 10^7 \text{ cm}^2 \text{ s}^{-1}$	3.4 × 10 ⁻⁴	4.6 × 10 ⁻⁴	2.9 × 10 ⁻⁶	1.3 × 10 ⁻⁷
$K_{zz} = 10^{10} \text{ cm}^2 \text{ s}^{-1}$	3.9 × 10 ⁻⁴	4.1 × 10 ⁻⁴	3.9 × 10 ⁻⁵	1.3 × 10 ⁻⁷
Nominal K_{zz} , 10 × solar	3.4 × 10 ⁻³	4.6 × 10 ⁻³	6.1 × 10 ⁻⁶	1.3 × 10 ⁻⁵
Our warmer “2 π ” Fortney et al. (2006, 2010) model at 0.1 bar (i.e., for secondary-eclipse conditions)				
Nominal K_{zz}	3.4 × 10 ⁻⁴	4.7 × 10 ⁻⁴	6.7 × 10 ⁻⁷	9.7 × 10 ⁻⁸
Primary transit: <i>Spitzer</i> IRAC				
Tinetti et al. (2007)	~5 × 10 ⁻⁴	1 × solar
Désert et al. (2009)	Upper limit	CO/H ₂ O ~ 5–60
Primary transit: <i>HST</i> NICMOS				
Swain et al. (2008b)	~5 × 10 ⁻⁴	...	~5 × 10 ⁻⁵	...
Madhusudhan & Seager (2009)	5 × 10 ⁻⁴ to 0.1	...	10 ⁻⁵ to 0.3	...
Sing et al. (2009)	Upper limit
Our nominal K_{zz} terminator-average model (i.e., for primary-transit conditions)				
At 10 ⁻⁴ bar	3.8 × 10 ⁻⁴	4.2 × 10 ⁻⁴	3.2 × 10 ⁻⁵	5.5 × 10 ⁻⁷
At 10 ⁻³ bar	3.8 × 10 ⁻⁴	4.2 × 10 ⁻⁴	4.3 × 10 ⁻⁵	4.5 × 10 ⁻⁷
At 10 ⁻² bar	3.8 × 10 ⁻⁴	4.2 × 10 ⁻⁴	4.5 × 10 ⁻⁵	3.2 × 10 ⁻⁷
At 10 ⁻¹ bar	3.8 × 10 ⁻⁴	4.2 × 10 ⁻⁴	4.6 × 10 ⁻⁵	2.0 × 10 ⁻⁷

Notes. For the observations in which “1 × solar” or “...” (no data) is listed, detailed constraints on the abundances were not presented. Our models assume 1 × solar abundance, unless otherwise indicated. The “nominal” K_{zz} profiles are shown in Figure 1.

region and unless zonal transport does not homogenize the CH₄ abundance in the 0.1–1 bar region. As was first demonstrated by Cooper & Showman (2006), vertical transport-induced quenching is quite effective in the upper atmospheres of hot Jupiters, and CH₄ is not readily converted to CO at dayside temperatures in our models. Some high-altitude CH₄ is lost to HCN and C₂H₂ in our models, but there is still sufficient CH₄ at transit-sensitive pressures that we would expect dayside observations to show CH₄ mole fractions only a factor of a few smaller than at the terminators for the dayside-average and terminator-average temperature profiles derived from the Showman et al. (2009) GCMs. If temperatures in the deep (1–10 bar) dayside atmosphere are much warmer than we have assumed (e.g., compare the 1D 2 π Fortney et al. 2006, 2010 profile with the area-weighted dayside-average thermal profile shown in Figure 2) or if K_{zz} ’s at the deep quench points are much smaller on the dayside than at the terminators, then this result could change.

The fact that the predicted infrared eclipse depths from our dayside-average model seem to be uniformly too small compared to observations, combined with the low dayside CH₄ abundance inferred by Swain et al. (2009a) and Madhusudhan & Seager (2009), suggests a scenario in which the dayside-versus-terminator temperature differences in the 1–100 bar region of HD 189733b are larger than is predicted from the Showman et al. (2009) GCMs. Quenched CH₄ abundances are much smaller in the model that uses the warmer “2 π ” 1D Fortney et al. (2006, 2010) thermal profile, for example (see Table 2).

The main problem with this scenario is that the radiative time constants at the CH₄ quench level near 1–10 bar are expected to be greater than the zonal transport timescales, so that one would expect the temperatures to be homogenized longitudinally in this region. The strong zonal winds would also be expected to help homogenize the CH₄ abundance across longitudes, so that there would not be a big terminator versus dayside difference, in conflict with the observations.

As it stands, neutral C–H–O–N chemistry does not seem to be able to account for a depletion of CH₄ at 1–10⁻³ bar pressures on the dayside of HD 189733b—where we expect transport-induced quenching to dominate—when we adopt the Showman et al. (2009) GCM-based temperature profiles. It is possible that sulfur photochemistry could contribute to a loss of CH₄ at these pressures on HD 189733b (Zahnle et al. 2009, 2011), despite the low S/C ratio expected for solar-like compositions, if catalytic destruction cycles are in operation. This process could only work effectively at low altitudes if the CH₄ mole fraction were comparable to the H₂S mole fraction (i.e., in situations where the quenched CH₄ abundance is small) because the solar ratio of S/C ≪ 1 will make it unlikely that products like CS and CS₂ can make a dent in the methane abundance if CH₄ is the dominant carbon carrier, and other potential products like C₂H_x hydrocarbons are unstable and will not replace methane at these pressures. In the (Zahnle et al. 2011) isothermal models, for instance, CS and CS₂ do not replace CH₄ at low altitudes because of the much greater CH₄ abundance as compared with

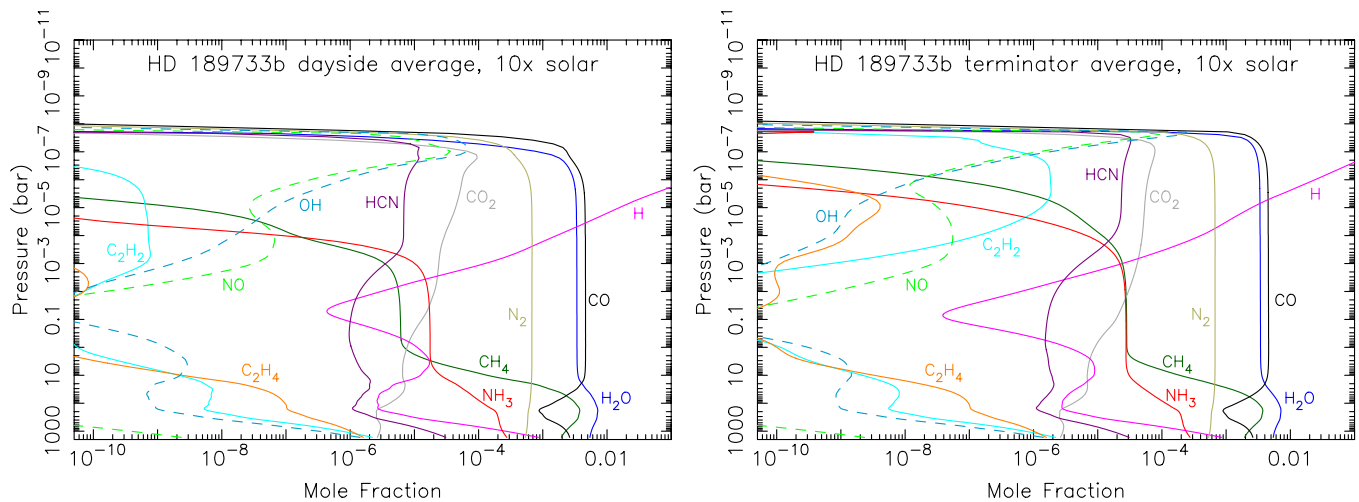


Figure 16. Mole-fraction profiles for several important species in dayside-average (left) and terminator-average (right) HD 189733b models that assume a $10\times$ solar composition but otherwise have the same K_{zz} profile, thermal structure, and background atmospheric grid as our nominal $1\times$ solar HD 189733b models shown in Figures 4–6. From comparisons between these figures, note the linear increase in the H_2O and CO mole fractions, the quadratic increase in the CO_2 mole fraction, the slight increase in the quenched NH_3 mole fraction, and the slight decrease in the quenched CH_4 mole fraction as the metallicity is increased from $1\times$ to $10\times$ solar. (A color version of this figure is available in the online journal.)

H_2S . However, since CH_4 is likely *not* the dominant carbon carrier on HD 189733b and HD 209458b, sulfur chemistry might potentially play a larger role in methane destruction than the Zahnle et al. (2011) models indicate. Similarly, PH_3 has weak bonds and could be an important source of atomic H at low altitudes that could affect CH_4 chemistry, but to truly destroy CH_4 in the lower stratosphere, some product like HCP must be able to compete with methane, which we think is unlikely given the thermodynamic stability of HCP—sulfur photochemistry seems to have greater promise as a mechanism for destroying CH_4 in the dayside lower stratosphere of HD 189733b.

Although our predicted CO_2 abundances for HD 189733b are consistent with those from the *HST* NICMOS secondary-eclipse observations reported by Swain et al. (2009a), a much greater CO_2 abundance is suggested from the Madhusudhan & Seager (2009) reanalysis of both these data and the *Spitzer* IRAC secondary eclipse data. Carbon dioxide closely follows thermochemical equilibrium in our models. Some additional CO_2 is produced at high altitudes from photochemistry in our models, but this amount is not sufficient to affect the column abundance at pressures greater than $\sim 10^{-2}$ bar. Therefore, if these larger observationally derived CO_2 values are correct, then HD 189733b likely has an enhanced metallicity (see also Fortney et al. 2010; Line et al. 2010; Zahnle et al. 2011). Enhanced metallicities might also help explain the strong absorption in the $4.5\ \mu\text{m}$ band from *Spitzer* IRAC transit observations (Désert et al. 2009). A large $\text{CO}/\text{H}_2\text{O}$ ratio was invoked by Désert et al. (2009) to explain this $4.5\ \mu\text{m}$ feature, which would not be consistent with solar elemental ratios; however, as is described by Fortney et al. (2010), this feature could also be explained by the high CO_2 abundances that are predicted from enhanced-metallicity models (Line et al. 2010; Zahnle et al. 2011). A high metallicity for HD 189733b might then explain both the Madhusudhan & Seager (2009) derived high CO_2 abundances from the *HST* NICMOS data of Swain et al. (2008b, 2009a), as well as the $4.5\ \mu\text{m}$ absorption seen by Désert et al. (2009).

Figure 16 illustrates how our HD 189733b model results change if we assume $10\times$ solar metallicity, but otherwise keep the same K_{zz} profile and atmospheric grid (e.g., the T – P profiles and scale height stay the same despite the increased mean

molecular weight and atmospheric opacity) as in our nominal $1\times$ solar model. The CO and H_2O mole fractions increase by a factor of 10, but the CO_2 mole fraction increases by a factor of ~ 100 , and the CH_4 mole fraction actually decreases when the metallicity is increased from $1\times$ to $10\times$ solar. The sensitivity of the CO_2 abundance to metallicity has been documented previously (Lodders & Fegley 2002; Line et al. 2010; Zahnle et al. 2011) and is the natural result of CO_2 's dependence on both CO and H_2O . The *decrease* in the CH_4 abundance with increased metallicity seems to result from the fact that the $\text{CH}_4 \rightarrow \text{CO}$ conversion schemes (2) and (3) in Section 3.2 are more effective when there is more H_2O and CO present, such that CH_4 follows its equilibrium curve to higher altitudes before the quench point occurs, resulting in a decrease in the quenched CH_4 abundance at higher metallicities. This higher-metallicity model seems at face value to be more consistent with the secondary-eclipse CO_2 and CH_4 abundances inferred by Madhusudhan & Seager (2009) and with the strong $4.5\ \mu\text{m}$ absorption observed in the transit observations of Désert et al. (2009), but the resulting water abundance may be higher than can be supported by the *HST* NICMOS secondary eclipse data, unless some additional absorption or scattering is muting the near-IR H_2O absorption bands.

In fact, the relatively low inferred H_2O mixing ratio for HD 189733b from the *HST* NICMOS secondary eclipse data (Swain et al. 2009a; Madhusudhan & Seager 2009) is somewhat disconcerting. Water is prevalent in both equilibrium and disequilibrium models for a wide range of metallicities. Only for greatly subsolar metallicities or greatly supersolar C/O ratios can the H_2O mole fraction be much less than 10^{-4} in the atmosphere of HD 189733b (e.g., Lodders & Fegley 2002; Line et al. 2010). As is discussed by numerous authors, water absorption is therefore expected to dominate the infrared spectrum of this and most other transiting extrasolar giant planets. Given the photochemical stability of H_2O and the likelihood of H_2O being carried to as high altitudes as any other stable molecular constituent, it is unlikely that clouds or hazes could obscure H_2O absorption features at near-infrared wavelengths without all other molecular features being obscured as well. However, where H_2O does not strongly absorb, other molecules—including

Table 3
Volume Mixing Ratios from HD 209458b Observations and Models

Source	H ₂ O	CO	CH ₄	CO ₂
Secondary eclipse: <i>Spitzer</i> IRAC (3.5, 4.6, 5.8, 8 μ m), IRS (16 μ m), and MIPS (24 μ m)				
Madhusudhan & Seager (2009)	$<10^{-4}$	$>4 \times 10^{-5}$	10^{-8} to 0.04	$(0.02\text{--}70) \times 10^{-7}$
Secondary eclipse: <i>Spitzer</i> IRAC, IRS, and <i>HST</i> NICMOS				
Swain et al. (2009b)	8×10^{-7} to 1×10^{-4}	...	$(0.2\text{--}2) \times 10^{-4}$	$(0.1\text{--}1) \times 10^{-5}$
Our nominal K_{zz} dayside-average model at 0.1 bar (i.e., for secondary-eclipse conditions)				
Nominal K_{zz}	3.4×10^{-4}	4.7×10^{-4}	3.7×10^{-7}	5.7×10^{-8}
Primary transit: <i>Spitzer</i> IRAC				
Beaulieu et al. (2010)	$1 \times$ solar
Our nominal western-terminator-average model (i.e., for primary-transit conditions)				
At 10^{-4} bar	3.5×10^{-4}	4.6×10^{-4}	6.3×10^{-7}	1.8×10^{-7}
At 10^{-3} bar	3.5×10^{-4}	4.6×10^{-4}	7.3×10^{-7}	2.0×10^{-7}
At 10^{-2} bar	3.5×10^{-4}	4.6×10^{-4}	7.6×10^{-7}	1.9×10^{-7}
At 10^{-1} bar	3.5×10^{-4}	4.6×10^{-4}	7.6×10^{-7}	1.2×10^{-7}

Notes. For the observations in which “ $1 \times$ solar” or “...” (no data) is listed, detailed constraints on the abundances were not presented. Our models assume $1 \times$ solar abundance, unless otherwise indicated. The “nominal” K_{zz} profiles are shown in Figure 1.

disequilibrium molecules—might contribute opacity that could mask the expected signatures of H₂O. As such, the observed apparent radius ratios between $1.66 \mu\text{m}$ and $1.87 \mu\text{m}$ in the *HST* NICMOS transit observations of Sing et al. (2009) could indicate the presence of an additional absorber rather than a lack of H₂O. Alternatively, the contrast in the absorption bands could be washed out due to multiple Rayleigh or aerosol scattering, but such effects should mute the contrast for all near-IR absorption features such that the relatively strong absorptions reported by Swain et al. (2008b, 2009a) could not be explained. In any case, spectral models need to be updated to include the effects of disequilibrium constituents.

These disequilibrium products will affect not only the observed spectra of HD 189733b, but the energy balance of the planet as well. A full discussion of the effect of disequilibrium constituents on the thermal structure of the planet is deferred to a future work.

7. COMPARISONS WITH OBSERVED MOLE FRACTIONS ON HD 209458b

Although some infrared photometric and spectral data that can potentially help constrain the abundance of C-, O-, and N-bearing molecules on HD 209458b have been acquired and analyzed (Brown et al. 2002; Richardson et al. 2003, 2006, 2007; Deming et al. 2005a, 2005b, 2007; Knutson et al. 2008, 2009; Beaulieu et al. 2010; Madhusudhan & Seager 2009), actual reported constraints on the molecular abundances are rare, due to signal-to-noise issues and to the fundamental degeneracy between temperatures and abundances that becomes a bigger problem for planets with stratospheric thermal inversions. Available constraints are listed in Table 3, along with some results from our models. Our nominal HD 209458b dayside-average model, which is supposed to be representative of secondary-eclipse conditions, has a greater water mixing ratio, a smaller CH₄ mixing ratio, and a smaller CO₂ mixing ratio than the values derived by Swain et al. (2009b). Since the mid-IR *Spitzer* data themselves may not provide strict constraints on the CH₄ mixing ratio (Madhusudhan & Seager 2009), this model-data discrepancy for CH₄ may not represent a true problem, unless the near-IR *HST* NICMOS data rather than the *Spitzer* IRAC and

IRS data are the main source of the CH₄ constraints from the Swain et al. (2009b) analysis. In any case, it is hard to imagine how HD 209458b could be very methane-rich, especially on the dayside, as the high stratospheric temperatures should drive the composition toward equilibrium, where CH₄ would then be a minor constituent. Larger eddy diffusion coefficients might help quench CH₄ at greater abundances than we are seeing in our nominal model, but thermochemical reactions on the dayside would still act to limit the total column abundance that could be built up. Perhaps some other constituent is masquerading as methane in the Swain et al. (2009b) data. Hydrogen cyanide is one possibility, although it, too, is predicted to be less abundant on the warm dayside. Carbon dioxide is another species that seems to be only loosely constrained by the mid-IR photometric data for HD 209459b (Madhusudhan & Seager 2009), so our models might not be out of line with the Swain et al. (2009b) data unless their CO₂ constraints come largely from the *HST* NICMOS data rather than the *Spitzer* photometric data. However, both Swain et al. (2009b) and Madhusudhan & Seager (2009) constrain the H₂O mixing ratio to be less than 10^{-4} , which would seem to favor low metallicities for HD 209458b, and the constraints on other species in relation to H₂O seems to favor large (non-solar) C/O ratios (Madhusudhan & Seager 2009). We have yet to investigate these types of models.

For the atmospheric composition at the terminators, even fewer constraints exist for the molecular composition. Beaulieu et al. (2010) do not provide any firm conclusions regarding molecular abundances and simply state that models that assume H₂O mixing ratios of 10^{-4} to 10^{-3} provide reasonable fits to the data, and that a CO mixing ratio of 10^{-4} , a CO₂ mixing ratio of 10^{-7} , and a CH₄ mixing ratio of 10^{-6} are allowable. Model-data comparisons by Fortney et al. (2010) with the Beaulieu et al. (2010) *Spitzer* IRAC data and the $24 \mu\text{m}$ *Spitzer* MIPS point from Richardson et al. (2006) and H. Knutson (2009, private communication) do not add any further constraints, although Fortney et al. (2010) note that the contrast in the Beaulieu et al. (2010) mid-IR data is hard to reproduce with their equilibrium models. In particular, absorption at 5.8 and $8 \mu\text{m}$ is underrepresented, or in general the contrast between the $3.6 \mu\text{m}$ and the 5.8 and $8 \mu\text{m}$ apparent radii is underrepresented by their models. As shown in Section 4 and Figure 9, the predicted

spectra from the disequilibrium models are similar to spectra from the equilibrium models, so disequilibrium chemistry of C, H, O, and N species cannot resolve these discrepancies.

8. CONCLUSIONS

Our kinetics-transport models for HD 189733b and HD 209458b demonstrate that disequilibrium processes such as photochemistry, chemical kinetics, and transport-induced quenching can dramatically affect the composition of extrasolar-giant-planet atmospheres. Although thermochemical equilibrium can be maintained in the deep, hot tropospheres of these planets, rapid transport and the photochemistry that is initiated from the absorption of ultraviolet photons from the host star can drive the composition away from equilibrium. The effects of these disequilibrium processes are more prominent for cooler exoplanets than for warmer exoplanets for two main reasons. First, the quench points for major species like CH_4 , CO , NH_3 , and N_2 are dependent on temperature: the colder the deep atmosphere, the less effective that thermochemical kinetics will be at maintaining equilibrium, and the deeper the pressure level at which the quenched species will depart from their equilibrium composition. Since the major transport-quenched species CH_4 and NH_3 on HD 189733b and HD 209458b have equilibrium abundances that increase with decreasing altitude, a deeper quench level corresponds to a greater mole fraction of the quenched constituent. Second, thermochemical kinetics will be less effective on planets with cooler stratospheres, such that disequilibrium compositions can be maintained. When stratospheric temperatures are high, such as is expected for HD 209458b and other planets with stratospheric thermal inversions—or that are very strongly irradiated in general—kinetic reactions are more effective at driving the composition back toward equilibrium, even in the presence of ultraviolet photons and transport-induced quenching. Disequilibrium processes are therefore expected to be more effective on the cooler HD 189733b than on the warmer HD 209458b.

Although transport-induced quenching can modify the abundances of all species, the effects are typically more noticeable for the species that are not expected to be abundant in equilibrium at observable altitudes. When CH_4 – CO interconversion ceases to become kinetically efficient, for example, both CH_4 and CO will quench, but the quenching will be most obvious for CO on planets that have cooler upper atmospheres (e.g., brown dwarfs or giant planets far from their host stars) and most obvious for CH_4 on planets with warmer upper atmospheres (e.g., highly irradiated hot Jupiters). The location of the quench point—such as whether it is in the CH_4 - or CO -dominated regime—can also play a role determining which molecule appears to be the most influenced by quenching.

In our kinetics-transport models that include neutral carbon, nitrogen, and oxygen chemistry, we find that species like CO , H_2O , CO_2 , and N_2 are relatively unaffected by disequilibrium chemistry because of their strong bonds and/or efficient recycling. The vertical profiles of these species are expected to follow equilibrium, except at very low pressures ($P \lesssim 1 \mu\text{bar}$), where photochemical processes can play a dominant role under some conditions. In contrast, the mole fractions of CH_4 and NH_3 are expected to be significantly enhanced (i.e., by several orders of magnitude) over equilibrium predictions in the bulk of the “photosphere” of these planets because of transport-induced quenching. In the upper stratosphere, however, photochemical processes abruptly and effectively remove NH_3 and CH_4 on

HD 189733b and HD 209458b in favor of photochemical products like HCN , C_2H_2 , N , and C (cf. Liang et al. 2004; Zahnle et al. 2009, 2011; Line et al. 2010).

As was first discussed by Liang et al. (2003), Yelle (2004), and García Muñoz (2007), one major consequence of photochemistry on close-in transiting planets like HD 209458b and HD 189733b is the production of huge quantities of atomic H due to catalytic cycles initiated by H_2O photolysis. In our model, as with some models of thermospheric photochemistry (e.g., Yelle 2004; García Muñoz 2007), H replaces H_2 as the most-abundant constituent near the base of the thermosphere, and H will be the dominant neutral component throughout the bulk of the thermosphere of these planets. Our model differs from those of Liang et al. (2003, 2004) and Line et al. (2010) in the effectiveness of H_2 destruction at high altitudes. Other significant photochemical products in our models include HCN , unsaturated hydrocarbons like C_2H_2 , atomic O , C , and N , and certain radicals like OH , CH_3 , and NH_2 .

This disequilibrium chemistry will have some observational consequences, as the disequilibrium products can affect the photometric and spectral signatures during the primary transit and secondary eclipse of transiting planets like HD 189733b and HD 209458b. Increased opacity from HCN , CH_4 , NH_3 , and under certain conditions C_2H_2 could be particularly important, especially for cooler planets like HD 189733b or for transit spectra that are influenced by the atmospheric transmission at the colder terminators. We recommend that investigators who analyze transit and eclipse data should include the possible effects of nitrogen-bearing species like HCN and NH_3 in their analyses. The additional disequilibrium species will also likely affect the thermal structure of the planets—a factor that was not considered in our present analysis—and future radiative models should include the effects of potential disequilibrium amounts of species like HCN , CH_4 , NH_3 , and C_2H_2 . We note that spectroscopic information on the hot bands of these molecules is needed to better predict the effects of these species on the observed spectra, and measurements of ultraviolet photoabsorption cross sections at high temperatures would improve the model predictions.

We find that although we produce some benzene, complex nitriles, and other high-molecular-weight species in our HD 189733b and HD 209458b models, the production of these and other potential soot precursors is not very favorable with our currently adopted neutral carbon, oxygen, and nitrogen photochemistry, in part because CO rather than CH_4 is the dominant carbon-bearing constituent at high altitudes in our models. In this respect, we disagree with the conclusions based on the cool, isothermal model atmospheres of Zahnle et al. (2009, 2011). On both HD 189733b and HD 209458b, we expect the $\text{CO} \leftrightarrow \text{CH}_4$ interconversion quench point to reside within the CO stability field, such that CO rather than CH_4 is the dominant carbon-bearing constituent in the cooler upper atmospheres of these planets—unless the eddy diffusion coefficient is extremely high ($K_{zz} > 10^{11} \text{ cm}^2 \text{ s}^{-1}$ on HD 189733b). Since cool ($\lesssim 1500 \text{ K}$) isothermal models are already quenched at the bottom boundary, where CH_4 is dominant, they predict unrealistically high CH_4 abundances on planets like HD 189733b (Zahnle et al. 2011). The likelihood of soot formation on HD 189733b has therefore been overemphasized in the Zahnle et al. (2011) models. On warmer planets like HD 209458b, complex hydrocarbons will have particular difficulty surviving, as the high H abundance and efficient thermochemical kinetics will greatly increase net destruction rates for these species. However, some soot formation

may be possible on cooler planets like HD 189733b, particularly if one considers the possibility of ion chemistry that is initiated from extreme ultraviolet radiation or charged particles from the parent star. On many planets with reduced atmospheres within our own solar system, high-altitude hazes are produced from such processes (e.g., West et al. 1981; Pryor & Hord 1991; Gérard et al. 1995; Wong et al. 2000, 2003; Friedson et al. 2002; Waite et al. 2007; Imanaka & Smith 2007; Vuitton et al. 2007, 2008). We encourage the consideration of Titan-like ion chemistry in future photochemical models of extrasolar giant planets.

Our models of neutral carbon, nitrogen, and oxygen chemistry shed little light on the source of the absorber responsible for the stratospheric thermal inversions inferred for HD 209458b and other exoplanets (e.g., Burrows et al. 2007, 2008; Knutson et al. 2008, 2009; Fortney et al. 2008a; Machalek et al. 2009, 2010; Madhusudhan & Seager 2009, 2010; O'Donovan et al. 2010). TiO was originally deemed to be a leading candidate because it would be expected to condense on cooler, less-irradiated hot Jupiters while remaining in gas phase on warmer, more highly irradiated hot Jupiters (Hubeny et al. 2003; Burrows et al. 2008; Fortney et al. 2008a); however, Knutson et al. (2010) argue that the lack of a convincing correlation between the incident flux and the presence of an inferred thermal inversion—as well as an observed apparent correlation between less chromospherically active stars and exoplanet thermal inversions—suggest that photochemistry might play a role, perhaps through destruction of the responsible absorber. In our models, we do not see any molecular absorbers on HD 209458b that are not also present on HD 189733b. In fact, the cool stratosphere of HD 189733b supports *more* disequilibrium molecular constituents than on HD 209458b. Atomic species are more prevalent on HD 209458b, and it is possible that some unidentified atom could be the culprit absorber, but that suggestion leads to a circular argument, as it is the high temperatures that cause atomic species to be more prevalent in the first place. Chromospherically active stars have more flares and produce more cosmic rays, and one might suggest that ion chemistry induced by charged particles from the host star could produce a high-altitude haze that could obscure the culprit absorber—despite the fact that photochemical hazes tend to be absorptive themselves and could thus heat the atmosphere (see Pont et al. 2008 for evidence of a Rayleigh-scattering atmosphere at visible wavelengths on HD 189733b such that the Na absorption features are obscured, suggesting a high-altitude haze, and see Zahnle et al. 2011 who champion soot formation at high altitudes). Alternatively, some sulfur photochemical product might contribute to absorption (Zahnle et al. 2009), or there could be a difference in dynamical mixing on different exoplanets. In any case, neutral C–N–O chemistry seems unlikely to explain the difference in stratospheric thermal profiles on HD 189733b and HD 209458b because of the expected similar photochemical products on the two planets, but ion chemistry might contribute to the destruction of gas-phase absorber or to the formation of complex C- and N-bearing photochemical products that are ultimately condensable.

The quantitative results of our models are very sensitive to factors such as the thermal structure, the eddy diffusion coefficient profile, and the planetary metallicity. Most of these parameters are not well constrained by observations. The eddy diffusion coefficients, in particular, are difficult to obtain either theoretically or observationally. If eddy diffusion coefficients in the lower stratosphere and upper troposphere were as low

as are suggested by Youdin & Mitchell (2010), then transport-induced quenching of constituents would be much less important on HD 189733b and HD 209458b. We note that if the CH₄ abundance and metallicity could be accurately constrained by observations, then one could place constraints on the value of K_{zz} at the CH₄ → CO quench point in the deep atmosphere. Similarly, one might suggest that the observed presence of heavy atomic species like O, C, and metals might provide some constraints on the eddy diffusion coefficients in the upper atmosphere, given that low K_{zz} values of $\lesssim 10^8$ cm² s^{−1} result in a very low homopause altitude in our models, making it difficult for heavy atomic species to be mixed into the thermosphere. Note, however, that this conclusion is based on hydrostatic models that do not include the hydrodynamic vertical wind, and it is likely that the hydrodynamic wind could dominate in cases where K_{zz} is low, such that the concept of a homopause level has little meaning for close-in transiting exoplanets; heavy species could be dragged into the thermosphere regardless of K_{zz} in these situations, and our low K_{zz} models are likely not very realistic.

Simple time-constant arguments suggest that advection might effectively homogenize the longitudinal composition such that the terminator-versus-dayside differences in the abundance of quenched species like CH₄ and NH₃ that are predicted by our simple 1D models would be washed out at pressures greater than a few mbar. Therefore, observations that indicate a difference in the column abundance of these species during transit as compared with eclipse observations could provide clues to the rate of horizontal transport in the lower stratosphere. In the upper stratospheres at pressures less than $\lesssim 1$ mbar, photochemical time constants likely dominate, suggesting that the composition could be highly variable with longitude at high altitudes. One important outcome is the potential conversion of HCN and C₂H₂ back to CH₄ at high altitudes on the nightside hemisphere. When that high-altitude methane flows back around to the dayside, it may strongly absorb stellar radiation, with some interesting radiative consequences, including potential emission in the ν_3 band of methane that has some strong lines that could potentially absorb at high altitudes if CH₄ is abundant enough (see the observations of Swain et al. 2010). The quantitative details need to be worked out to determine if this process is viable.

The qualitative details of the photochemistry described here will be similar to other hot Jupiters and hot Neptunes. On very cool planets like GJ 436b, CH₄ will dominate over CO, with a resulting increase in the production of photochemical products like hydrocarbons and nitriles. However, CH₄ will not be efficiently removed from the lower atmosphere of GJ 436b with our standard neutral C, O, N chemistry, and we cannot explain the low inferred CH₄ abundance on this planet (Stevenson et al. 2010). Sulfur photochemistry could potentially help (Zahnle et al. 2009, 2011), but only if the total sulfur mole fraction approaches the CH₄ mole fraction (i.e., for S/C ratios \gg solar) or if as-yet-unidentified catalytic cycles can permanently convert the methane into other hydrocarbons or C–O-bearing species.

We eagerly await future results from the upcoming *JWST*, whose broad wavelength coverage and other spectral capabilities should help reduce current uncertainties in the determination of atmospheric composition on extrasolar giant planets.

We thank A. García Muñoz for sending us his HD 209458b thermospheric model results, and Michael Line, Kevin Zahnle,

and Roger Yelle for interesting chemistry discussions. We gratefully acknowledge support from the NASA Planetary Atmospheres Program grant numbers NNX10AF65G (J.M.), NNX10AF64G (C.V.), NNX09AK24I (S.K.), and now NNX11AD64G. Support for C.V. also provided by the Lunar and Planetary Institute, USRA (NASA Cooperative Agreement NCC5-679). LPI Contribution Number 1622.

REFERENCES

- Agol, E., Cowan, N. B., Knutson, H., Deming, D., Steffen, J. H., Henry, G. W., & Charbonneau, D. 2010, *ApJ*, **721**, 1861
- Allen, M., Yung, Y. L., & Waters, J. W. 1981, *J. Geophys. Res.*, **86**, 3617
- Atkinson, R., Baulch, D. L., Cox, R. A., Hampson, R. F., Jr., Kerr, J. A., Rossi, M. J., & Troe, J. 1997, *J. Phys. Chem. Ref. Data*, **26**, 1329
- Atkinson, R., et al. 2006, *Atmos. Chem. Phys.*, **6**, 3625
- Ayers, T. 2005, in Proc. 13th Cool Stars Workshop, ed. F. Favata, G. Hussain, & B. Batrick (ESA SP-560; Noordwijk: ESA), 419
- Ballester, G. E., Sing, D. K., & Herbert, F. 2007, *Nature*, **445**, 511
- Baraffe, I., Chabrier, G., & Barman, T. 2010, *Rep. Prog. Phys.*, **73**, 016901
- Barber, R. J., Tennyson, J., Harris, G. J., & Tolchenov, R. N. 2006, *MNRAS*, **368**, 1087
- Barman, T. 2008, *ApJ*, **676**, L61
- Barnes, J. R., et al. 2010, *MNRAS*, **401**, 445
- Baulch, D. L., et al. 1992, *J. Phys. Chem. Ref. Data*, **21**, 411
- Baulch, D. L., et al. 1994, *J. Phys. Chem. Ref. Data*, **23**, 847
- Baulch, D. L., et al. 2005, *J. Phys. Chem. Ref. Data*, **34**, 757
- Beaulieu, J. P., Carey, S., Ribas, I., & Tinetti, G. 2008, *ApJ*, **677**, 1343
- Beaulieu, J. P., et al. 2010, *MNRAS*, **409**, 963
- Beaulieu, J. P., et al. 2011, *ApJ*, **731**, 16
- Ben-Jaffel, L. 2007, *ApJ*, **671**, L61
- Ben-Jaffel, L. 2008, *ApJ*, **688**, 1352
- Ben-Jaffel, L., & Hosseini, S. S. 2010, *ApJ*, **709**, 1284
- Berman, M. R., Fleming, J. W., Harvey, A. B., & Lin, M. C. 1982, *Chem. Phys.*, **73**, 27
- Bézar, B., Lellouch, E., Strobel, D., Maillard, J.-P., & Drossart, P. 2002, *Icarus*, **159**, 95
- Bouchy, F., et al. 2005, *A&A*, **444**, L15
- Brown, T. M. 2001, *ApJ*, **553**, 1006
- Brown, T. M., Charbonneau, D., Gilliland, R. L., Noyes, R. W., & Burrows, A. 2001, *ApJ*, **552**, 699
- Brown, T. M., Libbrecht, K. G., & Charbonneau, D. 2002, *PASP*, **114**, 826
- Burcat, A., & Ruscic, B. 2005, Third Millennium Ideal and Condensed Phase Thermochemical Database for Combustion with Updates from Active Thermochemical Tables, TAE 960, ANL-05/20 (Argonne, IL: Argonne National Laboratory)
- Burrows, A., Budaj, J., & Hubeny, I. 2008, *ApJ*, **678**, 1436
- Burrows, A., Hubbard, W. B., Lunine, J. I., & Liebert, J. 2001, *Rev. Mod. Phys.*, **73**, 719
- Burrows, A., Hubeny, I., Budaj, J., Knutson, H. A., & Charbonneau, D. 2007, *ApJ*, **668**, L171
- Burrows, A., & Sharp, C. M. 1999, *ApJ*, **512**, 843
- Canosa, A., Sims, I. R., Travers, D., Smith, I. W. M., & Rowe, B. R. 1997, *A&A*, **323**, 644
- Carvalho, E. F. V., Barauna, A. N., Machado, F. B. C., & Roberto-Neto, O. 2008, *Chem. Phys. Lett.*, **463**, 33
- Casavecchia, P., Balucani, N., Cartechini, L., Capozza, G., Bergeat, A., & Volpi, G. G. 2001, *Faraday Discuss.*, **119**, 27
- Castelli, F., & Kurucz, R. L. 2004, arXiv:astro-ph/0405087v1
- Charbonneau, D., Brown, T. M., Burrows, A., & Laughlin, G. 2007, in *Protostars and Planets V*, ed. B. Reipurth, D. Jewitt, & K. Keil (Tucson, AZ: Univ. Arizona Press), 701
- Charbonneau, D., Brown, T. M., Latham, D. W., & Mayor, M. 2000, *ApJ*, **529**, L45
- Charbonneau, D., Brown, T. M., Noyes, R. W., & Gilliland, R. L. 2002, *ApJ*, **568**, 377
- Charbonneau, D., Knutson, H. A., Barman, T., Allen, L. E., Mayor, M., Megeath, S. T., Queloz, D., & Udry, S. 2008, *ApJ*, **686**, 1341
- Charbonneau, D., et al. 2005, *ApJ*, **626**, 523
- Chase, M. W. 1998, NIST-JANAF Thermochemical Tables, J. Phys. Chem. Ref. Data, 28 (Monograph No. 9, 4th ed.; Melville, NY: AIP)
- Cooper, C. S., & Showman, A. P. 2006, *ApJ*, **649**, 1048
- Cowan, N. B., Agol, E., & Charbonneau, D. 2007, *MNRAS*, **379**, 641
- Dean, A. M., & Bozzelli, J. W. 2000, in *Gas Phase Combustion Chemistry*, ed. W. C. Gardiner, Jr. (New York: Springer), 125
- Dean, A. M., & Westmoreland, P. R. 1987, *Int. J. Chem. Kinetics*, **19**, 207
- Deming, D., Brown, T. M., Charbonneau, D., Harrington, J., & Richardson, L. J. 2005a, *ApJ*, **622**, 1149
- Deming, D., Richardson, L. J., & Harrington, J. 2007, *MNRAS*, **378**, 148
- Deming, D., & Seager, S. 2009, *Nature*, **462**, 301
- Deming, D., Seager, S., Richardson, L. J., & Harrington, J. 2005b, *Nature*, **434**, 740
- Désert, J.-M., Lecavelier des Etangs, A., Hébrard, G., Sing, D. K., Ehrenreich, D., Ferlet, R., & Vidal-Madjar, A. 2009, *ApJ*, **699**, 478
- Dunning, T. H., Jr. 1989, *J. Chem. Phys.*, **90**, 1007
- Ehrenreich, D., Hébrard, G., Lecavelier des Etangs, A., Sing, D. K., Désert, J.-M., Bouchy, F., Ferlet, R., & Vidal-Madjar, A. 2007, *ApJ*, **668**, L179
- Ehrenreich, D., et al. 2008, *A&A*, **483**, 933
- Fegley, B., Jr., & Lodders, K. 1994, *Icarus*, **110**, 117
- Fegley, B., Jr., & Lodders, K. 1996, *ApJ*, **472**, L37
- Fegley, B., Jr., & Prinn, R. G. 1985, *ApJ*, **299**, 1067
- Flasar, F. M., & Gierasch, P. J. 1977, in Proc. Nineteenth Symp. Roy. Soc. Canada, ed. A. V. Jones (Ottawa, Canada: Royal Soc. Canada), 85
- Fortney, J. J. 2005, *MNRAS*, **364**, 649
- Fortney, J. J., Cooper, C. S., Showman, A. P., Marley, M. S., & Freedman, R. S. 2006, *ApJ*, **652**, 746
- Fortney, J. J., Lodders, K., Marley, M. S., & Freedman, R. S. 2008a, *ApJ*, **678**, 1419
- Fortney, J. J., & Marley, M. S. 2007, *ApJ*, **666**, L45
- Fortney, J. J., Marley, M. S., Saumon, D., & Lodders, K. 2008b, *ApJ*, **683**, 1104
- Fortney, J. J., Shabram, M., Showman, A. P., Lian, Y., Freedman, R. S., Marley, M. S., & Lewis, N. K. 2010, *ApJ*, **709**, 1396
- Fortney, J. J., Sudarsky, D., Hubeny, I., Cooper, C. S., Hubbard, W. B., Burrows, A., & Lunine, J. I. 2003, *ApJ*, **589**, 615
- France, K., Stocke, J. T., Yang, H., Linsky, J. L., Wolven, B. C., Froning, C. S., Green, J. C., & Osterman, S. N. 2010, *ApJ*, **712**, 1277
- Freedman, R. S., Marley, M. S., & Lodders, K. 2008, *ApJS*, **174**, 504
- Fressin, F., Knutson, H. A., Charbonneau, D., O'Donovan, F. T., Burrows, A., Deming, D., Mandushev, G., & Spiegel, D. 2010, *ApJ*, **711**, 374
- Friedson, A. J., Wong, A.-S., & Yung, Y. L. 2002, *Icarus*, **158**, 389
- García Muñoz, A. 2007, *Planet. Space Sci.*, **55**, 1426
- Geballe, T. R., Saumon, D., Golimowsky, D. A., Leggett, S. K., Marley, M. S., & Noll, K. S. 2009, *ApJ*, **695**, 844
- Gérard, J.-C., Dols, V., Grodent, D., Waite, J. H., Gladstone, G. R., & Prangé, R. 1995, *Geophys. Res. Lett.*, **22**, 2685
- Gibson, N. P., Pont, F., & Aigrain, S. 2011, *MNRAS*, **411**, 2199
- Gladstone, G. R., Allen, M., & Yung, Y. L. 1996, *Icarus*, **119**, 1
- Gordon, S., & McBride, B. J. 1994, NASA Reference Publ., 1311
- Griffith, C. A., & Yelle, R. V. 1999, *ApJ*, **519**, L85
- Grillmair, C. J., et al. 2008, *Nature*, **456**, 767
- Gurwich, L. V., Veyts, I. V., & Alcock, C. B. 1989–1994, *Thermodynamic Properties of Individual Substances*, Vol. 3 (4th ed.; New York: Hemisphere)
- Haider, N., & Husain, D. 1993, *J. Photochem. Photobiol. A*, **70**, 119
- Harrington, J., Luszcz, S., Seager, S., Deming, D., & Richardson, L. J. 2007, *Nature*, **447**, 691
- Henry, G. W., Marcy, G. W., Butler, R. P., & Vogt, S. S. 2000, *ApJ*, **529**, L41
- Hubbard, W. B., Fortney, J. J., Lunine, J. I., Burrows, A., Sudarsky, D., & Pinto, P. 2001, *ApJ*, **560**, 413
- Hubeny, I., & Burrows, A. 2007, *ApJ*, **669**, 1248
- Hubeny, I., Burrows, A., & Sudarsky, D. 2003, *ApJ*, **594**, 1011
- Hwang, D.-Y., & Mebel, A. M. 2003, *J. Phys. Chem. A*, **107**, 2865
- Imanaka, H., & Smith, M. A. 2007, *Geophys. Res. Lett.*, **34**, L02204
- Iro, N., Bézar, B., & Guillot, T. 2005, *A&A*, **436**, 719
- Jasper, A., Klippenstein, S. J., Harding, L. B., & Ruscic, B. 2007, *J. Phys. Chem. A*, **111**, 3932
- Jodkowski, J. T., Rayez, M.-T., Rayez, J.-C., Bérce, T., & Dóbbé, S. 1999, *J. Phys. Chem. A*, **103**, 3750
- Kaiser, R. I., Mebel, A. M., & Lee, Y. T. 2001, *J. Chem. Phys.*, **114**, 231
- King, R. R., McCaughrean, M. J., Homeier, D., Allard, F., Scholz, R.-D., & Lodieu, N. 2010, *A&A*, **510**, A99
- Klippenstein, S. J. 2010, in *Miller, S., et al. Faraday Discuss.*, **147**, 251
- Klippenstein, S. J., Harding, L. B., Ruscic, B., Sivaramakrishnan, N. K., Su, M.-C., & Michael, J. V. 2009, *J. Phys. Chem. A*, **113**, 10241
- Knutson, H. A., Charbonneau, D., Allen, L. E., Burrows, A., & Megeath, S. E. 2008, *ApJ*, **673**, 526
- Knutson, H. A., Howard, A. W., & Isaacson, H. 2010, *ApJ*, **720**, 1569
- Knutson, H. A., et al. 2007, *Nature*, **447**, 183
- Knutson, H. A., et al. 2009, *ApJ*, **690**, 822
- Koskinen, T. T., Aylward, A. D., & Miller, S. 2009, *ApJ*, **693**, 868
- Koskinen, T. T., Aylward, A. D., Smith, C. G. A., & Miller, S. 2007, *ApJ*, **661**, 515
- Koskinen, T. T., Yelle, R. V., Lavvas, P., & Lewis, N. K. 2010, *ApJ*, **723**, 116

- Lammer, H., et al. 2009, *A&A*, **506**, 399
- Langland-Shula, L. E., Vogt, S. S., Charbonneau, D., Butler, P., & Marcy, G. 2009, *ApJ*, **696**, 1355
- Lecavelier des Etangs, A., Pont, F., Vidal-Madjar, A., & Sing, D. 2008a, *A&A*, **481**, L83
- Lecavelier des Etangs, A., Vidal-Madjar, A., Désert, J.-M., & Sing, D. 2008b, *A&A*, **485**, 865
- Lecavelier des Etangs, A., Vidal-Madjar, A., McConnell, J. C., & Hébrard, G. 2004, *A&A*, **418**, L1
- Lecavelier des Etangs, A., et al. 2010, *A&A*, **514**, A72
- Leggett, S. K., Saumon, D., Marley, M. S., Geballe, T. R., Golimowski, D. A., Stephens, D., & Fan, X. 2007, *ApJ*, **655**, 1079
- Lendvay, G., Bérces, T., & Márta, F. 1997, *J. Phys. Chem. A*, **101**, 1588
- Lewis, J. S., & Fegley, B., Jr. 1984, *Space Sci. Rev.*, **39**, 163
- Lewis, J. S., & Prinn, R. G. 1980, *ApJ*, **238**, 357
- Liang, M.-C., Parkinson, C. D., Lee, A. Y. T., Yung, Y. L., & Seager, S. 2003, *ApJ*, **596**, L247
- Liang, M.-C., Seager, S., Parkinson, C. D., Lee, A. Y. T., & Yung, Y. L. 2004, *ApJ*, **605**, L61
- Line, M. R., Liang, M. C., & Yung, Y. L. 2010, *ApJ*, **717**, 496
- Linsky, J. L., Yang, H., France, K., Froning, C. S., Green, J. C., Stocke, J. T., & Osterman, S. N. 2010, *ApJ*, **717**, 1291
- Lodders, K. 2003, *ApJ*, **519**, 793
- Lodders, K. 2004, *Science*, **303**, 323
- Lodders, K. 2009, in *Formation and Evolution of Exoplanets*, ed. R. Barnes (Berlin: Wiley), 157
- Lodders, K., & Fegley, B., Jr. 2002, *Icarus*, **155**, 393
- Lodders, K., Palme, H., & Gail, H.-P. 2009, in *The Solar System*, ed. J. E. Trümper (Berlin: Springer-Verlag)
- Machalek, P., McCullough, P. R., Burke, C. J., Valenti, J. A., Burrows, A., & Hora, J. L. 2008, *ApJ*, **684**, 1427
- Machalek, P., McCullough, P. R., Burrows, A., Burke, C. J., Hora, J. L., & Johns-Krull, C. M. 2009, *ApJ*, **701**, 514
- Machalek, P., et al. 2010, *ApJ*, **711**, 111
- Madhusudhan, N., & Seager, S. 2009, *ApJ*, **707**, 24
- Madhusudhan, N., & Seager, S. 2010, *ApJ*, **725**, 261
- Madhusudhan, N., & Seager, S. 2011, *ApJ*, **729**, 41
- Marley, M. S., Fortney, J. J., Seager, S., & Barman, T. 2007, in *Protostars and Planets V*, ed. B. Reipurth, D. Jewitt, & K. Keil (Tucson, AZ: Univ. Arizona Press), 733
- Mebel, A. M., Kislov, V. V., & Hayashi, M. 2007, *J. Chem. Phys.*, **126**, 204310
- Michelangelo, D. V., Allen, M., Yung, Y. L., Shia, R.-L., Crisp, D., & Eluszkiewicz, J. 1992, *J. Geophys. Res.*, **97**, 865
- Miller, J. A., Klippenstein, S. J., Robertson, S. H., Pilling, M. J., & Green, N. J. B. 2009, *Phys. Chem. Chem. Phys.*, **11**, 1128
- Montes, D., López-Santiago, J., Gálvez, M. C., Fernández-Figueroa, M. J., De Castro, E., & Cornide, M. 2001, *MNRAS*, **328**, 45
- Moses, J. I. 1996, in *The Collision of Comet Shoemaker-Levy 9 and Jupiter*, ed. H. A. Weaver, K. S. Noll, & P. D. Feldman (Cambridge: Cambridge Univ. Press), 243
- Moses, J. I., Allen, M., & Gladstone, G. R. 1995a, *Geophys. Res. Lett.*, **22**, 1597
- Moses, J. I., Allen, M., & Gladstone, G. R. 1995b, *Geophys. Res. Lett.*, **22**, 1601
- Moses, J. I., Bézard, B., Lellouch, E., Gladstone, G. R., Feuchtgruber, H., & Allen, M. 2000a, *Icarus*, **143**, 244
- Moses, J. I., Fouchet, T., Bézard, B., Gladstone, G. R., Lellouch, E., & Feuchtgruber, H. 2005, *J. Geophys. Res.*, **110**, E08001
- Moses, J. I., Lellouch, E., Bézard, B., Gladstone, G. R., Feuchtgruber, H., & Allen, M. 2000b, *Icarus*, **145**, 166
- Moses, J. I., Visscher, C., Keane, T. C., & Sperier, A. 2010, *Faraday Discuss.*, **147**, 103
- Murray-Clay, R. A., Chiang, E. I., & Murray, N. 2009, *ApJ*, **693**, 23
- Noll, K. S., Geballe, T. R., & Marley, M. S. 1997, *ApJ*, **489**, L87
- O'Donovan, F. T., Charbonneau, D., Harrington, J., Madhusudhan, N., Seager, S., Deming, D., & Knutson, H. A. 2010, *ApJ*, **710**, 1551
- Penz, T., et al. 2008, *Planet. Space Sci.*, **56**, 1260
- Perryman, M. A. C., et al. 1997, *A&A*, **323**, L49
- Pont, F., Knutson, H., Gilliland, R. L., Moutou, C., & Charbonneau, D. 2008, *MNRAS*, **385**, 109
- Pople, J. A., Head-Gordon, M., & Raghavachari, K. 1987, *J. Chem. Phys.*, **87**, 5968
- Prinn, R. G., & Barshay, S. S. 1977, *Science*, **198**, 1031
- Prinn, R. G., & Olague, E. P. 1981, *J. Geophys. Res.*, **86**, 9895
- Pryor, W. R., & Hord, C. W. 1991, *Icarus*, **91**, 161
- Redfield, S., Endl, M., Cochran, W. D., & Koesterke, L. 2008, *ApJ*, **673**, L87
- Richardson, L. J., Deming, D., Horning, K., Seager, S., & Harrington, J. 2007, *Nature*, **445**, 892
- Richardson, L. J., Deming, D., & Seager, S. 2003, *ApJ*, **597**, 581
- Richardson, L. J., Harrington, J., Seager, S., & Deming, D. 2006, *ApJ*, **649**, 1043
- Rothman, L. S., et al. 2009, *J. Quant. Spectrosc. Radiat. Transfer*, **110**, 533
- Saumon, D., Geballe, T. R., Leggett, S. K., Marley, M. S., Freedman, R. S., Lodders, K., Fegley, B., Jr., & Sengupta, S. K. 2000, *ApJ*, **541**, 374
- Saumon, D., Marley, M. S., Cushing, M. C., Leggett, S. K., Roellig, T. L., Lodders, K., & Freedman, R. S. 2006, *ApJ*, **647**, 552
- Saumon, D., Marley, M. S., Lodders, K., & Freedman, R. S. 2003, in *IAU Symp. 211, Brown Dwarfs*, ed. E. Martín (San Francisco, CA: ASP), 345
- Seager, S., & Sasselov, D. D. 2000, *ApJ*, **537**, 916
- Seager, S., Whitney, B. A., & Sasselov, D. D. 2000, *ApJ*, **540**, 504
- Shabram, M., Fortney, J. J., Greene, T. P., & Freedman, R. S. 2011, *ApJ*, **727**, 65
- Sharp, C. M., & Burrows, A. 2007, *ApJS*, **168**, 140
- Shkolnik, E., Bohlender, D. A., Walker, G. A. H., & Collier Cameron, A. 2008, *ApJ*, **676**, 628
- Showman, A. P., Cho, J. Y.-K., & Menou, K. 2010, in *Exoplanets*, ed. S. Seager (Tucson, AZ: Univ. Arizona Press), 471
- Showman, A. P., Cooper, C. S., Fortney, J. J., & Marley, M. S. 2008, *ApJ*, **682**, 559
- Showman, A. P., Fortney, J. J., Lian, Y., Marley, M. S., Freedman, R. S., Knutson, H. A., & Charbonneau, D. 2009, *ApJ*, **699**, 564
- Sing, D. K., Désert, J.-M., Lecavelier des Etangs, A., Ballester, G. E., Vidal-Madjar, A., Parmentier, V., Hébrard, G., & Henry, G. W. 2009, *A&A*, **505**, 891
- Sing, D. K., Vidal-Madjar, A., Désert, J.-M., Lecavelier des Etangs, A., & Ballester, G. 2008a, *ApJ*, **686**, 658
- Sing, D. K., Vidal-Madjar, A., Lecavelier des Etangs, A., Désert, J.-M., Ballester, G., & Ehrenreich, D. 2008b, *ApJ*, **686**, 667
- Smith, M. D. 1998, *Icarus*, **132**, 176
- Smith, G. P., et al. 2000, GRI Mech 3.0, http://www.me.berkeley.edu/gri_mech/
- Snellen, I. A. G., Albrecht, S., de Mooij, E. J. W., & Le Poole, R. S. 2008, *A&A*, **487**, 357
- Southworth, J. 2010, *MNRAS*, **408**, 1689
- Spiegel, D. S., Silverio, K., & Burrows, A. 2009, *ApJ*, **699**, 1487
- Stevenson, K. B., et al. 2010, *Nature*, **464**, 1161
- Stone, P. H. 1976, in *Jupiter*, ed. T. Gehrels (Tucson, AZ: Univ. Arizona Press), 586
- Swain, M. R., Bouwman, J., Akeson, R. L., Lawler, S., & Beichman, C. A. 2008a, *ApJ*, **674**, 482
- Swain, M. R., Vasisth, G., & Tinetti, G. 2008b, *Nature*, **452**, 329
- Swain, M. R., Vasisth, G., Tinetti, G., Bouwman, J., Chen, P., Yung, Y., Deming, D., & Deroo, P. 2009a, *ApJ*, **690**, L114
- Swain, M. R., et al. 2009b, *ApJ*, **704**, 1616
- Swain, M. R., et al. 2010, *Nature*, **463**, 637
- Tashkun, S. A., Perevalov, V. I., Teffo, J.-L., Bykov, A. D., & Lavrentieva, N. N. 2003, XIV Symposium on High Resolution Molecular Spectroscopy, Krasnoyarsk, Russia, 2003 July 6–11
- Tian, F., Toon, O. B., Pavlov, A. A., & De Sterck, H. 2005, *ApJ*, **621**, 1049
- Tinetti, G., et al. 2007, *Nature*, **448**, 169
- Tinetti, G., et al. 2010, *Faraday Discuss.*, **147**, 369
- Torres, G., Winn, J. N., & Holman, M. J. 2008, *ApJ*, **677**, 1324
- Troyer, J., Moses, J. I., Fegley, B., Lodders, K., Marley, M. S., & Fortney, J. J. 2007, *BAAS*, **39**, 450
- Tsang, W. 1987, *J. Phys. Chem. Ref. Data*, **16**, 471
- Tsang, W. 1991, *J. Phys. Chem. Ref. Data*, **20**, 221
- Udry, S., Fischer, D., & Queloz, D. 2007, in *Protostars and Planets V*, ed. B. Reipurth, D. Jewitt, & K. Keil (Tucson, AZ: Univ. Arizona Press), 685
- Vidal-Madjar, A., Lecavelier des Etangs, A., Désert, J.-M., Ballester, G. E., Ferlet, R., Hébrard, G., & Mayor, M. 2003, *Nature*, **422**, 143
- Vidal-Madjar, A., Lecavelier des Etangs, A., Désert, J.-M., Ballester, G. E., Ferlet, R., Hébrard, G., & Mayor, M. 2008, *ApJ*, **676**, L57
- Vidal-Madjar, A., et al. 2004, *ApJ*, **604**, L69
- Visscher, C., & Fegley, B., Jr. 2005, *ApJ*, **623**, 1221
- Visscher, C., Lodders, K., & Fegley, B., Jr. 2006, *ApJ*, **648**, 1181
- Visscher, C., Lodders, K., & Fegley, B., Jr. 2010a, *ApJ*, **716**, 1060
- Visscher, C., & Moses, J. I. 2011, *ApJ*, submitted
- Visscher, C., Moses, J. I., & Saslow, S. A. 2010b, *Icarus*, **209**, 602
- Vuitton, V., Yelle, R. V., & Cui, J. 2008, *J. Geophys. Res.*, **113**, E05007
- Vuitton, V., Yelle, R. V., & McEwan, M. J. 2007, *Icarus*, **191**, 722
- Waite, J. H., Jr., Young, D. T., Cravens, T. E., Coates, A. J., Crary, F. J., Magee, B., & Westlake, J. 2007, *Science*, **316**, 870
- Waite, J. H., Jr., Young, D. T., Westlake, J. H., Lunine, J. I., McKay, C. P., & Lewis, W. S. 2009, in *Titan from Cassini-Huygens*, ed. R. H. Brown, J.-P. Lebreton, & J. H. Waite (Dordrecht: Springer), 201

- West, R. A., Hord, C. W., Simmons, K. E., Coffeen, D. L., Sato, M., & Lane, A. L. 1981, *J. Geophys. Res.*, **86**, 8783
- Wong, A.-S., Lee, A. Y. T., Yung, Y. L., & Ajello, J. M. 2000, *ApJ*, **534**, L215
- Wong, A.-S., Yung, Y. L., & Friedson, A. J. 2003, *Geophys. Res. Lett.*, **30**, 1447
- Yamamura, I., Tsuji, T., & Tanabé, T. 2010, *ApJ*, **722**, 682
- Yelle, R. V. 2004, *Icarus*, **170**, 167
- Youdin, A. N., & Mitchell, J. L. 2010, *ApJ*, **721**, 1113
- Yung, Y. L., Allen, M., & Pinto, J. P. 1984, *ApJS*, **55**, 465
- Yung, Y. L., Drew, W. A., Pinto, J. P., & Friedl, R. R. 1988, *Icarus*, **73**, 516
- Zahnle, K., Marley, M. S., & Fortney, J. J. 2011, *ApJ*, submitted (arXiv:0911.0728v2)
- Zahnle, K., Marley, M. S., Freedman, R. S., Lodders, K., & Fortney, J. J. 2009, *ApJ*, **701**, L20
- Zobov, N. F., et al. 2008, *MNRAS*, **387**, 1093